Universidade de São Paulo
Instituto de Astronomia, Geofísica e Ciências Atmosféricas
Departamento de Geofísica

Caio Augusto Deiroz Amaral

Paleomagnetic study of Bahia Archean rocks

Estudo paleomagnético de rochas Arqueanas da Bahia

São Paulo

2021

Caio Augusto Deiroz Amaral

Paleomagnetic study of Bahia Archean rocks

Estudo paleomagnético de rochas Arqueanas da Bahia

Dissertação apresentada ao Departamento de Geofísica do Instituto de Astronomia, Geofísica e Ciências Atmosféricas da Universidade de São Paulo como requisito parcial para a obtenção do título de Mestre em Ciências.

Área de Concentração: Geofísica
Orientador(a): Prof. Dr. Ricardo Ivan Ferreira da Trindade

Versão Corrigida. O original encontra-se disponível na Unidade.

São Paulo

2021

To my family and friends.

Acknowledgements

To my family for always encouraging me to persist in my goals and to be there to support when needed.

To my advisor Prof. Dr. Ricardo I. F. da Trindade for the help, assistance, patience and friendship during this years. For always providing greats opportunities for me.

To all of my colleagues at the post graduation program in IAG. Especially those that where always present at the coffee after lunch and in the yearly barbecues.

To all the members of the USP-MAG laboratory for the great discussions, laughs and friendships over this years.

To all of the professors, technicians and staff of the IAG-USP.

To the São Paulo Research Foundation (FAPESP), for the financial support, process n°: 2019/24450-1 (The opinions, hypotheses and conclusions or recommendations expressed in this material are the responsibility of the author and do not necessarily reflect the view of FAPESP);

Esta tese/dissertação foi escrita em LaTeX com a classe IAGTESE, para teses e dissertações do IAG.

"Nada é mais real
Que aprender maneira simples de viver
Tudo é tão normal
Se a gente não se cansa nunca de aprender
Sempre olhar como se fosse a primeira vez
Se espantar como criança a perguntar porquês"

Almir Sater e Paulo Simões

Resumo

Amaral, C. A. D. **Estudo paleomagnético de rochas Arqueanas da Bahia.** 2021. 113pp. Dissertação (Mestrado) - Instituto de Astronomia, Geofísica e Ciências Atmosféricas, Universidade de São Paulo, São Paulo, 2021.

Este estudo realizou uma caracterização da mineralogia magnética, fábrica magnética e direção paleomagnética em um conjunto de diques máficos não datados (14.15°S, 40.72°W) e em um afloramento de rochas riolíticas Arqueanas (13.668°S, 40.905°W) no interior do estado da Bahia, Brasil. Os seguintes procedimentos laboratoriais foram realizados: obtenção de curvas termomagnéticas (variação $\chi - T$), ciclos de histerese, magnetização remanente isotérmica (MRI) e curvas de reversão de primeira ordem (FORC), definição da anisotropia de susceptibilidade magnética (ASM) e anisotropia de susceptibilidade magnética anisterética (AASM) e aplicação de técnicas de desmagnetização térmica e por campos magnéticos alternados. O principal mineral portador da magnetização em ambos conjuntos de rochas é a magnetita de pseudo-domínio simples à multidomínio, no entanto as rochas também apresentaram uma grande quantidade de minerais paramagnéticos. O conjunto de amostras de diques máficos não apresentou resultados satisfatórios para as análises de anisotropia e paleomagnetismo. A trama magnética dos riolitos apresentou baixos valores de susceptibilidade magnética e de grau de anisotropia (parâmetro P). O corpo como um todo exibiu um padrão subvertical para Leste, indicando um comportamento coerente para o fluxo de lava. A caracterização paleomagnética indicou apenas uma componente de magnetização secundária ($D_m = 40.52°$, $I_m = 4.32°$, $\alpha_{95} = 22.67°$, $K = 8.04$) apresentando um polo paleomagnético localizado em 46.82°N, 30.68°E ($dp = 11.38$, $dm = 22.72$).

Palavras chave: Magnetismo de rocha, fábrica magnética, paleomagnetismo, riolitos Arqueanos.

Abstract

Amaral, C. A. D. **Paleomagnetic study of Bahia Archean rocks** 2021. 113pp. Thesis (Master's degree) - Institute of Astronomy, Geophysics and Atmospheric Sciences, University of São Paulo, São Paulo, 2021.

This study performed a characterization of the magnetic mineralogy, magnetic fabric and paleomagnetic direction in a set of undated mafic dikes (14.15°S, 40.72°W) and in an outcrop of Archean rhyolitic rocks (13.668°S, 40.905°W) in the interior of the state of Bahia, Brazil. The following laboratory procedures were performed: obtaining thermomagnetic curves ($\chi - T$ diagram), hysteresis loops, isothermal remanent magnetization (IRM) and first order reversal curves (FORC), definition of the anisotropy of magnetic susceptibility (AMS) and anisotropy of anhysteretic magnetic susceptibility (AAMS) and application of thermal and alternated magnetic fields demagnetization techniques. The main magnetic carrier in both sets of rocks is the pseudo-single domain to multi-domain magnetite, however the rocks also presented a large amount of paramagnetic minerals. The set of mafic dykes samples did not present satisfactory results for the AMS analysis and paleomagnetism direction characterization. The magnetic fabric of the rhyolites presented low values of magnetic susceptibility and anisotropy degree (P parameter). The outcrop region exhibited coherent eastward sub-vertical lava flow direction. The paleomagnetic characterization indicated only one secondary remanence direction ($D_m = 40.52°$, $I_m = 4.32°$, $\alpha_{95} = 22.67°$, $K = 8.04$) with a paleomagnetic pole located at 46.82°N, 30.68°E ($dp = 11.38$, $dm = 22.72$).

Keywords: Rock magnetism, magnetic fabric, paleomagnetism, Archean rhyolite.

List of Figures

List of Tables

Contents

Chapter 1

Introduction

At the beginning of Earth's history, the planet had distinct characteristics and behaviors. The plate tectonics mechanism and the geomagnetic field properties were probably different than today, also the generation and development of continental crust had its peculiarities (McElhinny and Senanayake, 1980; Kröner and Layer, 1992; Tarduno et al., 2007; Hawkesworth et al., 2010, 2016; Smirnov et al., 2016).

One of the best ways to make an attempt to comprehend how the continental crust behaved itself at the early Earth is by performing a multi-approach study at Archean cratons (Bleeker, 2003; Bleeker and Ernst, 2006; Brenner et al., 2020; Smirnov et al., 2013; Salminen et al., 2019). Bleeker (2003) defined a supercraton as "*a large ancestral landmass of Archean age with a stabilized core that on break-up spawned several independently drifting cratons*", the author also proposes that the most probable scenario for the Late Archean configuration was that existed a limited set of supercratons that originated the present day known Archean cratons and fragments. Therefore, to study the tectonic evolution of current Archean cratons it is necessary to analyze the development of the supercraton that originated them and reliable chronostratigraphic data in order to correlated the Archean cratons distributed around the world. One of the best tools to make correlation is the comparison of age and direction of Paleoproterozoic mafic dykes swarms that occurred at the supercratons before their break-up, therefore facilitating its paleogeographic reconstruction (Bleeker and Ernst, 2006).

The work of Bleeker and Ernst (2006) demonstrated how mafic dyke swarms or rapid magmatic generation events are key to performe a high quality paleogeographic reconstruction. According to the authors, a well dated geochronological analyses (with associated error $\leq$ 2 Ma), a high quality paleomagnetic study and an integrated mapping of a mafic

dyke swarm make it possible to located two neighboring cratons with a common point at the location of the dykes occurrence, ensuring the cratons positions.

Recently, several authors have been performing new studies about Archean paleographic reconstructions using the approach described above (de Kock et al., 2009; Evans et al., 2017; Mertanen and Korhonen, 2011; Salminen et al., 2019; D'Agrella-Filho et al., 2020). Despite the effort, there are very few good quality Precambrian paleomagnetic studies, even less so in South America (Evans and Pisarevsky, 2008; D'Agrella-Filho and Cordani, 2017).

The São Francisco Craton is composed of Archean to Proterozoic rocks (Almeida, 1977; Hasui et al., 2012) and has its largest portion situated at Bahia and Minas Gerais states (Figure 2.1). The Gavião Block represents part of the craton basement and some of the oldest rocks of South America were found on it (Oliveira et al., 2019). The present work will seek to characterize new paleomagnetic, anisotropy of magnetic susceptibility and magnetic mineralogy information of a ∼3.3 Ga rhyolite rocks (Zincone et al., 2016) and undated dykes that outcrops at Serra dos Meiras.

Chapter 2

Geology

2.1 São Francisco Craton

The São Francisco Craton (Almeida, 1977) is one of the major Brazilian geotectonic compartments (Hasui et al., 2012) which is mostly located in the Bahia and Minas Gerais states (Figure 2.1), southeastern and northeastern Brasil respectively, and it is surrounded by fold belts (Araçuai, Ribeira, Brasília, Rio Preto, Riacho do Pontal and Sergipano Belts) that originated during the Brasiliano orogeny (Barbosa et al., 2003; Heilbron et al., 2017; Teixeira et al., 2000).

The basement of the craton is composed of Paleoproterozoic and Archean rocks (Figure 2.1) that are exposed in the southernmost part of the craton, in the Quadrilátero Ferrífero region in Minas Gerais state, and in the northeastern part of the craton, in the Bahia state (Alkmim, 2004; Alkmim and Teixeira, 2017; Barbosa and Barbosa, 2017; Heilbron et al., 2017). The northeastern part of the craton consists of gneissic migmatitic rocks, granulites, granitoids and greenstone belts that outcrops in the Gavião , Jequié and Serrinha Blocks which are separeted by the Contendas-Jacobina Lineament as shown in Figure 2.2 (Teixeira et al., 2017). These blocks contain some of the oldest rocks in South America with ages ranging from ∼2.4 Ga up to ∼3.7 Ga (Barbosa and Sabaté, 2002, 2004; Martin et al., 1991; Nutman and Cordani, 1993; Nutman et al., 1994; Peucat et al., 2002).

The studies of Barbosa and Sabaté (2002, 2004) explain the main geotectonic process that generated the four Archean Blocks of the basement of the craton. According to the authors, the crustal fragments that originated the Blocks, collided during the Paleoproterozoic Transamazonian Cycle due to a NW-SE sinistral movement. The collision of Gavião and Serrinha Blocks resulted in the formation of the Itabuna-Salvador-Curaça

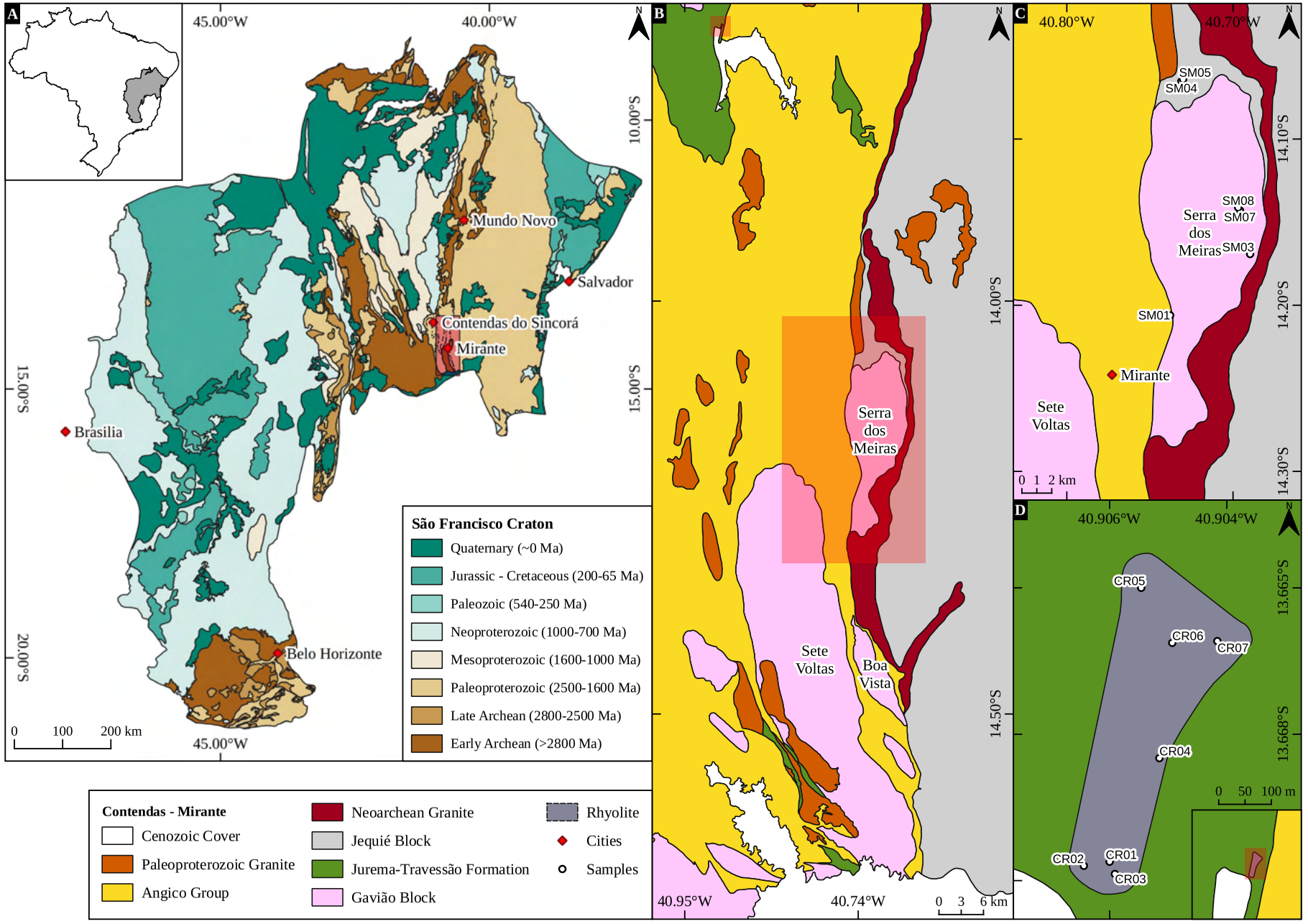

Figure 2.1: A - São Francisco Craton; B - Contendas - Mirante region; C - Sample location of the mafic dykes; D - Sample location of the rhyolite (modified from Cordani et al., 2016; Macêdo, 2016; Martins et al., 2017a,b).

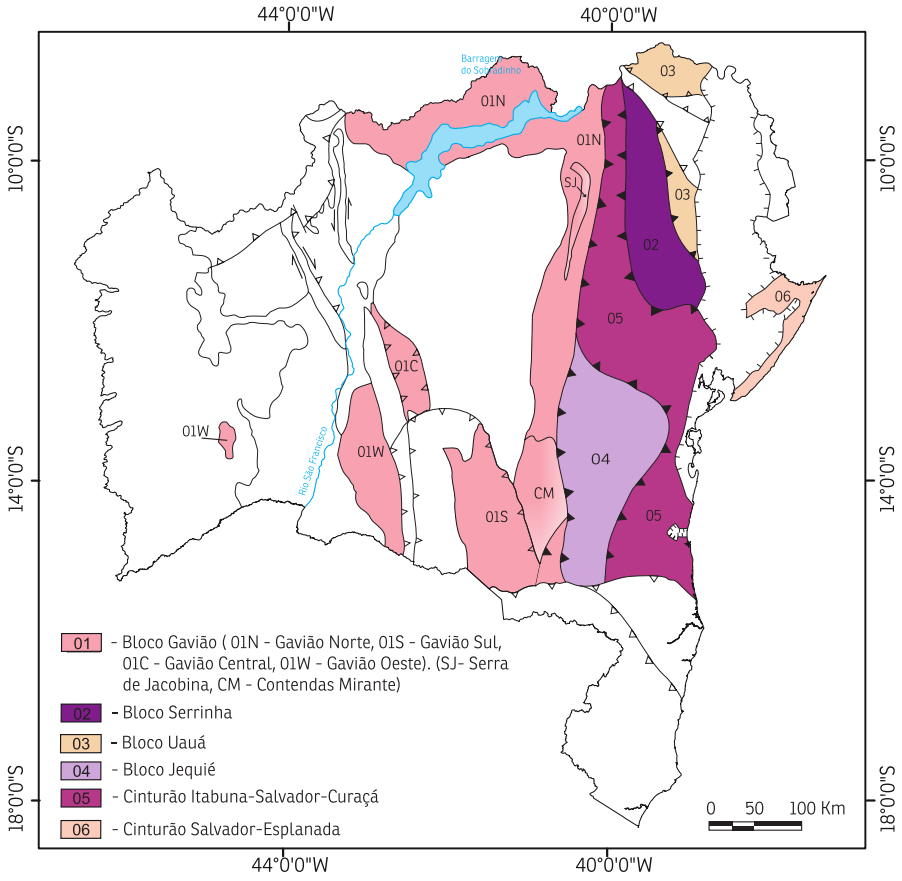

Figure 2.2: Simplified map showing the main geologic Blocks of the northeastern part of the São Francisco Craton in the Bahia state (modified from Barbosa et al., 2012).

Belt and the collision of the Gavião and Jequié Blocks resulted in the formation of the Contendas-Mirante Sedimentary Belt and Umburanas Greenstone Belt.

The Gavião Block is composed of Paleoarchean tonalites-trondhjemites-granodiorites (TTGs) (Condie, 2014; Moyen and Martin, 2012), Meso-Neoarchean granodioritic, gnaissic and granitic rocks that could eventually migmatized in anphibolite facies, Archean-Paleoproterozoic greenstone belts (Barreiro-Colomi, Boquira, Brumado, Guajeru, Ibitira-Ubiraçaba, Lagoa do Alegre, Mundo Novo, Riacho de Santana, Salitre-Sobradinho, Tiquara and Umburanas) and volcanic sedimentary belts (Caetité-Licínio de Almeida, Contendas-Mirante, Ibiajara and Urandi) (Barbosa and Sabaté, 2002, 2004; Barbosa et al., 2012; Marinho et al., 1993; Teixeira et al., 2000, 2017).

The Contendas-Mirante Volcanic Sedimentary Belt (CMVSB) is divided into the Angico Group (Areião, Santana, Rio Gavião and Mirante Formations), Barreiro D'Anta and Jurema-Travessão Formations, TTGs domes and Paleoproterozoic-Neoarchean Granitoids (Marinho et al., 2009) (Figure 2.1). The Jurema-Travessão Formation (JTF) border the

CMVSB following the contact with the Jequié and Gavião Block and is mainly composed of metavolcanic and metasedimentary rocks (Leite and Marinho, 2012; Marinho et al., 1993, 1994, 2009). The TTGs nuclei that outcrops in the southern part of the CMVSB are the Sete Voltas, Boa Vista and Serra dos Meiras massifs which represents the basement of the Gavião Block that was uplifted during the Paleoproterozoic tectonic events (Marinho et al., 1993; Martin et al., 1997). The Sete Voltas massif is essentially made of grey gneisses (3.0 - 3.4 Ga), porphyritic granodiorites (∼3.2 Ga) and granitic dykes (∼2.6 Ga) and the Boa Vista massif is essentially made of granitic rocks (∼3.4 Ga) (Cordani et al., 1985; Marinho et al., 1993; Martin et al., 1991, 1997; Nutman and Cordani, 1993). The Serra dos Meiras massif is essentially composed of granodiorites, tonalites and gray gneisses (∼3.4 Ga) and undated dykes that intrude the dome (Marchesin, 2015).

The Mundo Novo Greenstone Belt (MNGB) is located in the southern sector of the Serra Jacobina (Mascarenhas and Silva, 1994). The basement of the MNGB is described as gneisses and migmatized TTGs of the Mairi Complex, the lower units are represented by mafic-ultramafic rocks of the Saúde Complex and Jacobina Group, the upper units are composed by the Itapura Complex, Saúde Complex and Mundo Novo Complex and between these units some mafic and felsic volcanic rocks are exposed (Cunha et al., 2012; Macêdo, 2016; Martins et al., 2017a,b; Mascarenhas et al., 1998). Peucat et al. (2002) performed an U-Pb geochronological study on the MNGB in which porphyritic metadacite samples presented an age of ∼3.3 Ga.

Zincone et al. (2016) studied some rhyolites that are exposed in the MNGB and in the JTF. The authors established that the samples from both localities are cogenetic, had the same origin as the Boa Vista and Serra dos Meiras Granites, were formed in a intra-continent rift system and it still present the primary volcanic features (the samples from the JTF). Zincone et al. (2016) also made a geochronological and mineralogical studies in the rhyolites determining an age of ∼3.3 Ga (U-Pb) and that it is mainly composed of feldspar, quartz, plagioclase, chlorite, biotite and magnetite .

In this work, it will be performed a magnetic mineralogy characterization, a paleomagnetic analyses and an anisotropy of magnetic susceptibility study in nine sites of the mafic dykes that occurs in the Serra dos Meiras massif (SJ, SM01-08) and in seven sites of the non metamorphosed rhyolites of the JTF (CR01-07).

Chapter 3

Methods

3.1 Rock Magnetism

In all known materials the movement of electrons around the atomic nucleus gives rise to a resultant force (torque) called magnetic moment (m). The relation between the sum of all magnetic moments and the volume (V) of the material results in the magnetization (M) of the material (Lowrie and Fichtner, 2007), as in Equation 3.1 below:

$$M = \frac{\sum m_i}{V} \tag{3.1}$$

The magnetization is the ability of a material to stay magnetized in the presence of a magnetic field (Griffiths, 1999). The magnetization (M) is given in relation with magnetic susceptibility (χ) and the magnetic field (H). Another important magnetic property of materials is the relation between the induction field (B) with M and H (Tauxe et al., 2018). Both relations are respectively described in the Equation 3.2 and 3.3 below:

$$M = \chi H \tag{3.2}$$

$$B = \mu(H + M) \tag{3.3}$$

χ defines the ability with which the material is magnetized and μ is the magnetic permeability which defines how easily the magnetic flux can go through the material, both are dimensionless. According with the International System of Units (SI) (Newell and Tiesinga, 2019): $M[Am^{-1}], m[Am^2], B[NA^{-1}m^{-1}], H[Am^{-1}], \mu_0[NA^2], V[m^3]$.

There are three different types of magnetic materials (diamagnetic, paramagnetic and ferromagnetic), in each type the magnetization has a characteristic behavior (Figure 3.1). In diamagnetic materials, when a magnetic field (H) is applied, the magnetization (M)

decreases, this happens because diamagnetic materials have a weak and negative magnetic susceptibility. Paramagnetic materials have a weak and positive magnetic susceptibility, therefore when a H field is applied, the magnetization will give a positive response. In ferromagnetic materials the magnetization has a unique response to the applied H field. The main characteristics of ferromagnetic substances are that they achieve saturation, possess an intrinsic coercivity and, mostly important, has a spontaneous magnetization in the absence of the H field (Dunlop and Özdemir, 1997). They present a spontaneous magnetization due to the alignment of the atomic magnetic moments according to the crystaline structure of the solid, the principal manners that it happens is demonstrated in Figure 3.2.

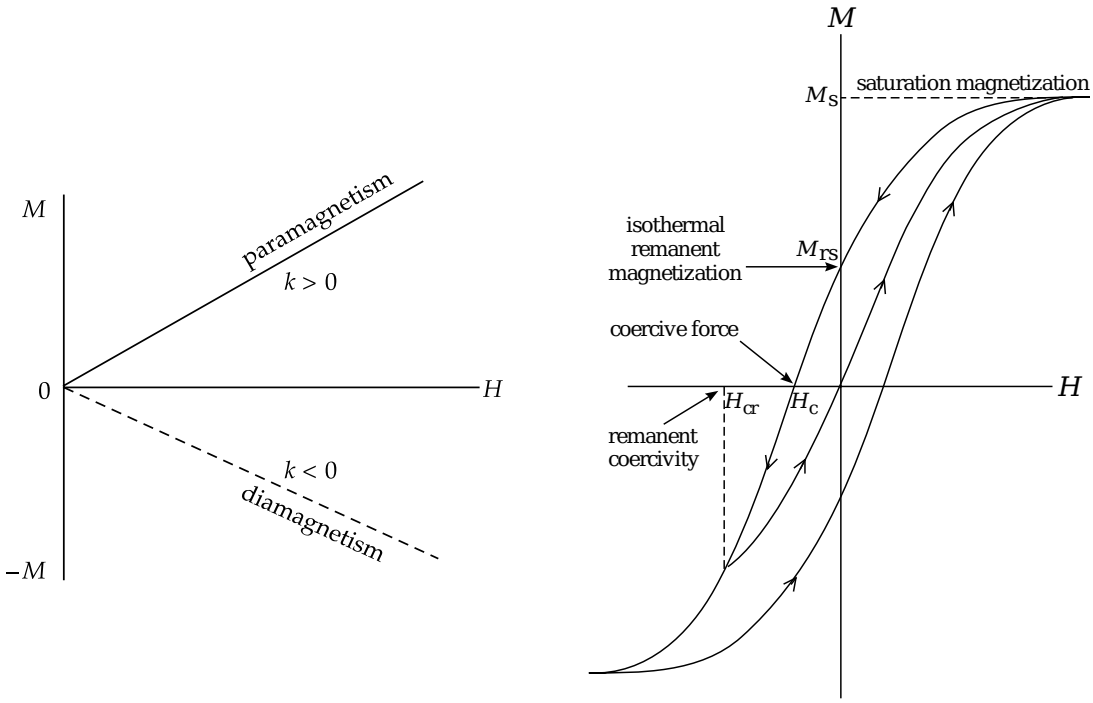

(a) Diamagnetic-Paramagnetic behavior *(b)* Ferromagnetic behavior

Figure 3.1: Magnetization behavior in differents types of materials (after Lowrie and Fichtner, 2007)

In ferromagnetic particles (*e.g.* magnetite, hematite), the magnetic spins will tend to align in a way that the internal energy of the particle is minimum, those types of arrangement are known as magnetic domains. Smalls particles will have a single domain (SD) behavior while a bigger particles will have a multi-domain (MD) behavior, the transition of SD to MD is known as pseudo-single domain (PSD) and very small particles, with $\tau < 100s$ (Equation 3.5), has a superparamagnetic behavior (Tauxe et al., 2018). Lascu et al. (2018)

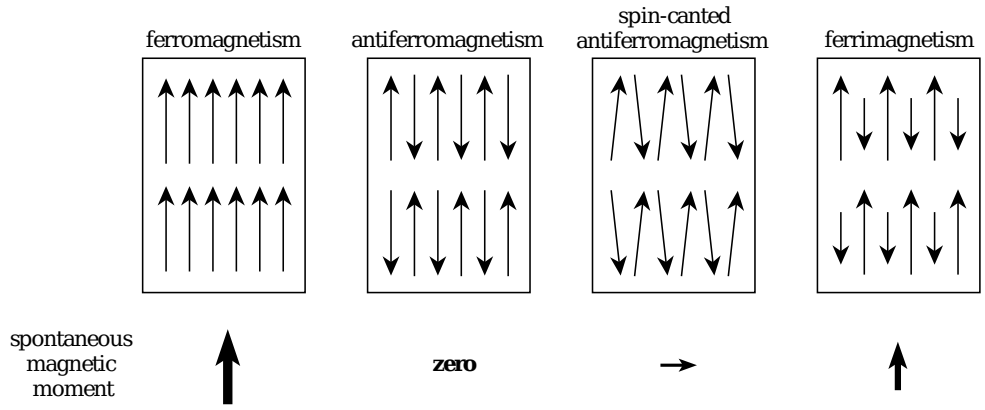

Figure 3.2: Schematic representation of magnetic moment alignment of ferromagnetic materials (after Lowrie and Fichtner, 2007)

provided a new perspective in understanding the magnetic domains, by performing a micromagnetic modeling in which he demonstrated the complexity surrounding the magnetic domains, specially the PSD domain.

In rock magnetism and paleomagnetism analysis it is important to determine which minerals composes the studied rock. The most important mineral types for those analysis are the ferromagnetic minerals which preserve the information of the Earth's magnetic field at the time of rock formation. The main magnetic minerals and its principals characteristics are indicated in Table 3.1 below.

Table 3.1 - Principal properties of the main magnetic minerals.

Ferromagnetic mineral	$M_S[kA/m]$	$T_C[^\circ C]$	Max $T_B[^\circ C]$	Max Coercivity $[T]$
Maghemite (γFe_2O_3)	380	590 - 675	≈350	0.3
Hematite (αFe_2O_3)	≈2.5	675	675	1.5 - 5
Magnetite (Fe_3O_4)	480	580	575	0.3
Titanomagnetite ($Fe_{2.4}Ti_{0.6}O_4$)	≈125	150 - 200	150	0.1
Titanomagnetite ($Fe_{2.7}Ti_{0.3}O_4$)	-	≈400	350	0.2

M_S = Spontaneous Magnetization, T_C = Curie Temperature, T_B = Blocking Temperature (Adapted from Dunlop and Özdemir, 1997; Lowrie and Fichtner, 2007).

3.2 Rock Magnetization Processes

3.2.1 Thermal Remanent Magnetization

In well preserved igneous rocks, the magnetic information of the rock can be preserved for millions of years. According to Néel Theory (Néel, 1955), in a assemblage of identical

SD grains, the magnetization over time ($M_{(t)}$) will obey the Equation 3.4, where $M_{(0)}$ is the magnetization of the rock when it was formed and τ is the relaxation time which defines for how long can the magnetization remain stable (Equation 3.5 from Tauxe et al. (2018)).

$$M_{(t)} = M_{(0)} \exp\left(\frac{-t}{\tau}\right) \tag{3.4}$$

$$\tau = \frac{1}{C} \exp\left(-\frac{Kv}{kT}\right)\left(1 - \frac{H}{H_c}\right)^2 \tag{3.5}$$

C is a lattice vibrational frequency factor [$\approx 10^8 - 10^{10}s{-}1$], K is the anisotropy parameter [Jm^{-3}], v is the grain volume [m^3], k is the Boltzmann constant [JK^{-1}], T is the temperature [K], H is the local magnetic field [T] and H_c is the grain coercivity [T].

The relaxation time is essentially defined by the relation between the anisotropic energy (Kv) and the thermal energy (kT), its behavior is demonstrated in the Néel Diagram (Figure 3.3). In ferromagnetic materials there is a specific temperature in which the mineral change its behavior, this temperature is known as Curie Temperature (T_C), while in antiferromagnetic materials it's known as Néel Temperature (T_N). When the material has a temperature $T > T_C$, the thermal energy dominates and the grain acquire a paramagnetic behavior, therefore it won't be able to preserve the magnetic information. The material will only be capable to preserve the remanent magnetization when $T < T_C$ thus presenting a ferromagnetic behavior, but there is a temperature gap ($T_B < T < T_C$) in which the grain still doesn't preserve the magnetization information because it has a superparamagnetic behavior ($\tau < 100s$). The temperature where the anisotropic energy overcomes the thermal energy is known as Blocking Temperature (T_B), only for $T < T_B$ the material will be able to preserve remanent magnetization.

3.2.2 Chemical Remanent Magnetization

The formation of new magnetic minerals or the alteration of pre-existing minerals can occur in a rock that passes through chemical alteration processes. Those altered/created minerals, when grow in volume in the presence of an external magnetic field, if achive a minimum volume, will acquire a Chemical Remanent Magnetization (CRM) (Butler, 1992).

In subaerial lava flows, the high-temperature oxyexsolution of titanomagnetites produces an intergrowth of magnetite with ilmenite, if the oxidation continues it will become a

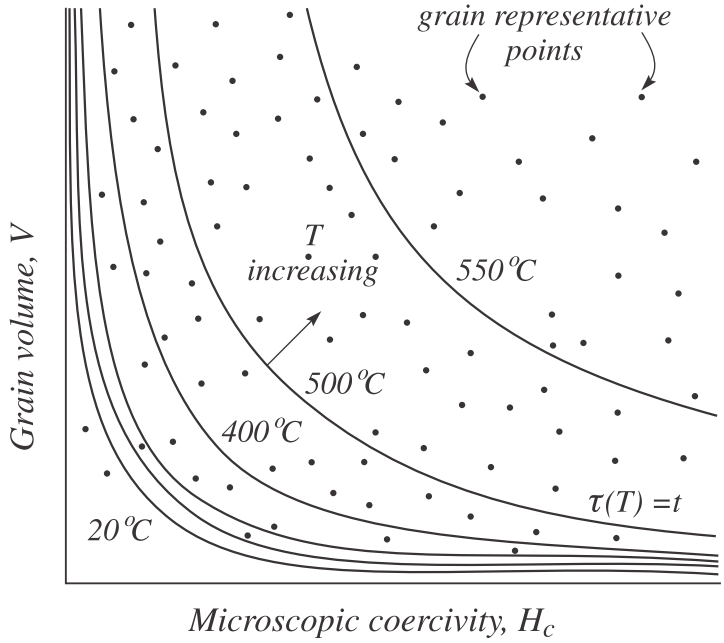

Figure 3.3: Néel Diagram - the continuous lines indicate grains whose combinations of volume and coercivity values produce the same unblocking temperatures (after Dunlop and Özdemir, 2015).

mixture of hematite, pseudobrookite and rutile. This type of process is known as Thermochemical Remanent Magnetization (TCRM) in which occur simultaneously the slow cooling and the volume growth of the magnetic grain. Usually, reheating processes on this type of samples produce a T_B higher than ordinary (Buddington and Lindsley, 1964; Dunlop and Özdemir, 1997).

3.2.3 Viscous Remanent Magnetization

The Earth surface rocks are always subject to Earth's geomagnetic field, whose characteristics vary over time (*e.g.* geomagnetic pole position drift, reversal of polarity). The long lasting exposure to a weak magnetic field induces a secondary magnetization in the rocks known as Viscous Remanent Magnetization (VRM). The VRM obey the Equation 3.5, but its behavior over time exhibit a logarithmic pattern due to the variety of grain sizes and shapes in the material (Butler, 1992; Dunlop and Özdemir, 1997).

Another type of VRM is the Thermoviscous Remanent Magnetization (TVRM) which is a viscous magnetization more effective due to higher temperatures, causing the rock to lose part of its primary magnetization (Figure 3.4). The key factors that determine if the rock has lost all of its magnetic information are the temperature which the rock was subjected and for how long it was exposed (Pullaiah et al., 1975).

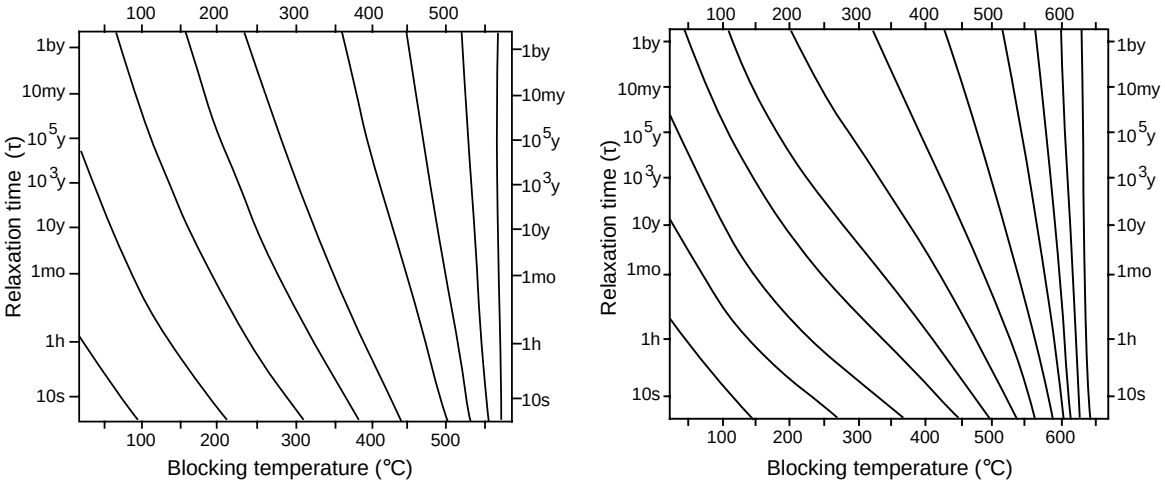

(a) Magnetite *(b)* Hematite

Figure 3.4: Pullaiah diagrams - the continuous lines indicate how blocking temperatures vary with different relaxation times for the same grains (adapted from Butler, 1992 *apud* Pullaiah et al., 1975).

Paleomagnetic studies on Archean rocks often shown that part of the rock magnetization was acquired due to TVRM processes, making the magnetization intensity be lower then expected. In order to fully understand the magnetization in such ancient rocks, one must fully comprehend how the TVRM was generated and how it influences in the rock magnetization (Herrero-Bervera et al., 2016; Smirnov and Tarduno, 2005).

3.2.4 Isothermal Remanent Magnetization

A rock briefly subjected to a strong magnetic field at constant temperature will obtain a secondary magnetization called Isothermal Remanent Magnetization (IRM) (Lowrie and Fichtner, 2007). In nature, this type of magnetization process happens when a rock is exposed to a magnetic field created by a lightning strike (Butler, 1992).

A rock that was hit by a lighting strike has its magnetic properties modified. It will present a increase in its magnetization intensity, susceptibility values and in the Koenigsberger's Q values (ratio of remanent over induced magnetization), will also have its magnetic mineralogy alterated by oxidation of magnetite to maghemite (Salminen et al., 2013).

3.3 Statistics in Paleomagnetism

In order to understand the magnetic information in rocks samples, it is necessary to perform some laboratory analysis (Section 3.5.1) to extract the magnetic directional information. To do so, the sample magnetic declination and inclination information vectors are decomposed in small portions and the statistical analysis of this decomposition provides some knowledge of the ancient geomagnetic field.

Fisher (1953) developed the statistics of directional data on a sphere which is used to analyze paleomagnetic directions. Equation 3.6 gives the probability of finding a direction in a band of width $d\theta$ between θ and $\theta + d\theta$:

$$P_{d\theta}(\theta) = \frac{\kappa}{2sinh(\kappa)} \exp[\kappa cos(\theta)] sin(\theta) d\theta \tag{3.6}$$

where θ is the angle from the true mean direction and κ is the precision parameter.

The precision parameter determines how scattered the data are on the sphere. Low values of κ indicates that the data is widely scattered while higher values of κ indicates that the data is well grouped. From a finite sample set of directions κ can be estimated by Equation 3.7:

$$\kappa \approx k = \frac{N-1}{N-R} \tag{3.7}$$

where N is the number of unit vectors that represent from each sample directional data and R is the resultant vector (McFadden, 1980; Tauxe et al., 2018).

The confidence limit is another important parameter, it determinate an angular radius from the calculated mean direction which indicates the probability of the true mean direction to fall inside such circle. Equation 3.8 provides de confidence limit for a known data set:

$$cos\alpha_{(1-p)} = 1 - \frac{N-R}{R}\left[\left(\frac{1}{p}\right)^{\frac{1}{N-1}} - 1\right] \tag{3.8}$$

$(1-p)$ represent the probability level, in other words, how accurate the data is regarded to the calculated mean, usually $(1-p) = 0.95$. A reasonable approximation for $\kappa \geq 10$ and $N \geq 10$ is given by Equation 3.9 (Butler, 1992):

$$\alpha_{95} \approx \frac{140^\circ}{\sqrt{kN}} \tag{3.9}$$

The Fisher Distribution Function is the most used analytical tool in determining mean paleomagnetic directions. Nevertheless, it is important to say the there are others statistical approaches that can be used to analyze vector data. Kent Distribution (Kent, 1982)

considers that the probability parameter has elliptic distribution instead of a circular one. Bingham Distribution (Bingham, 1974) takes one step further. It considers that the distribuiton has elliptical behavior and is antipodally symmetric, in others words, it treats bi-modal data. However, each method has its owns advantages and disadvantagesand an analysis is needed to determine which of the approaches is best suited for the desired analysis.

In order to ensure the data quality in paleomagnetic studies, (Van der Voo, 1990) established seven reliability criteria, among which the criteria regarding age reliability (I, IV), structural control (V) and laboratory demagnetization analysis (II, III) are the most important. Meert et al. (2020) reviewed the original work of Van der Voo (1990) and updated the seven reliability criteria under the light of the new development that occurred in the paleomagnetic science in the past 30 years. The seven criteria from the original work are listed in Table 3.2 below:

Table 3.2 - Van der Voo (1990) seven quality criteria.

I.	Well-determined rock age and a presumption that magnetization is the same age;
II.	Sufficient numbers of samples ($N \geq 24$), κ (or K) ≥ 10 and α_{95} (A_{95}) ≤ 16.0;
III.	Adequate demagnetization that demonstrably includes vector subtraction;
IV.	Fields tests that constrain the age of magnetization;
V.	Structural control and tectonic coherence with craton or block involved;
VI.	The presence of reversals;
VII.	No resemblance to paleopoles of younger age (by more than a period).

3.4 Sample Collection and Preparation

Samples at each sampling site were collected using a gasoline powered drill as shown in Figure 3.5. Each site provided 7-11 oriented cores with approximately 5-8 cm long and 2.5cm in diameter, the location of all sites are presented in Figure 2.1. The samples were oriented by a Pomeroy Orienting Fixture (ASC Scientific^{TM}) coupled with a Brunton Compass.

The core samples were cut in small cylinders (specimens) with ≈2.2cm length in the laboratory of the Institute of Astronomy, Geophysics and Atmospheric Sciences of the University of São Paulo (IAG-USP) Figure 3.6. All core samples provided 191 specimens for the mafic dykes and 64 specimens for the rhyolite.

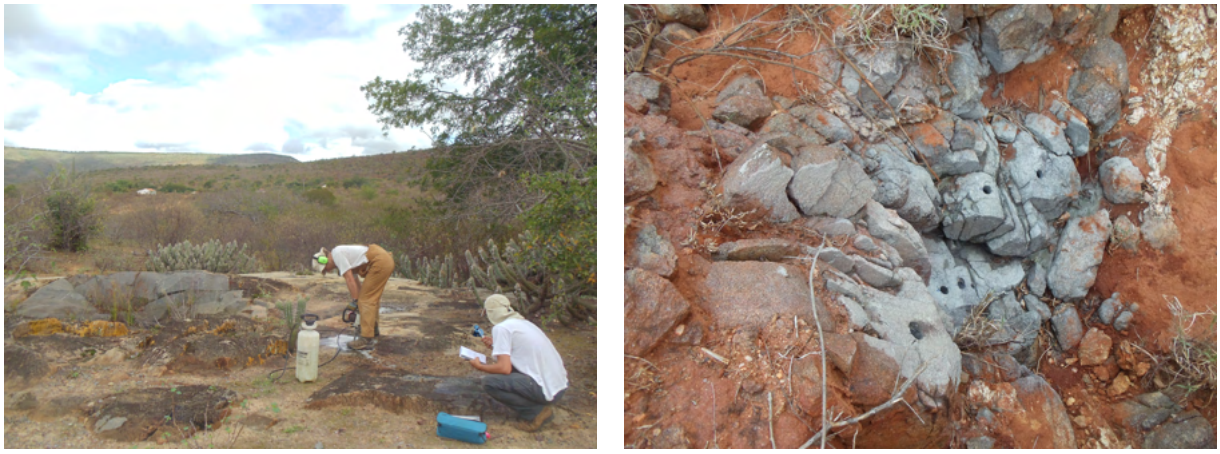

(a) Rhyolite *(b)* Mafic dyke

Figure 3.5: Sampling

Figure 3.6: Laboratory samples

3.5 *Laboratory Analysis*

All the analysis were performed at the Paleomagnetism and Rock Magnetism Laboratory at IAG-USP (USPMag). The demagnetization procedures were performed inside a shielded room with ambient magnetic field $< 500\ nT$.

3.5.1 Reconstructing a Long Forgotten Directional Vector

The magnetization directional data in unaltered igneous rocks can be recovered using demagnetization techniques (Collinson, 1983). Those techniques seeks to retrieve the geomagnetic field characteristics (declination, inclination, intensity) of the rock formation times. In order to do so, it is performed a step-wise demagnetization protocol applying alternating magnetic field or thermal procedures. Both methods obey Equation 3.5, but

use different approaches (Parry, 2013). Figure 3.7 exemplifies a response to be obtained from a demagnetization process applied to a sample with two well-separated magnetization components.

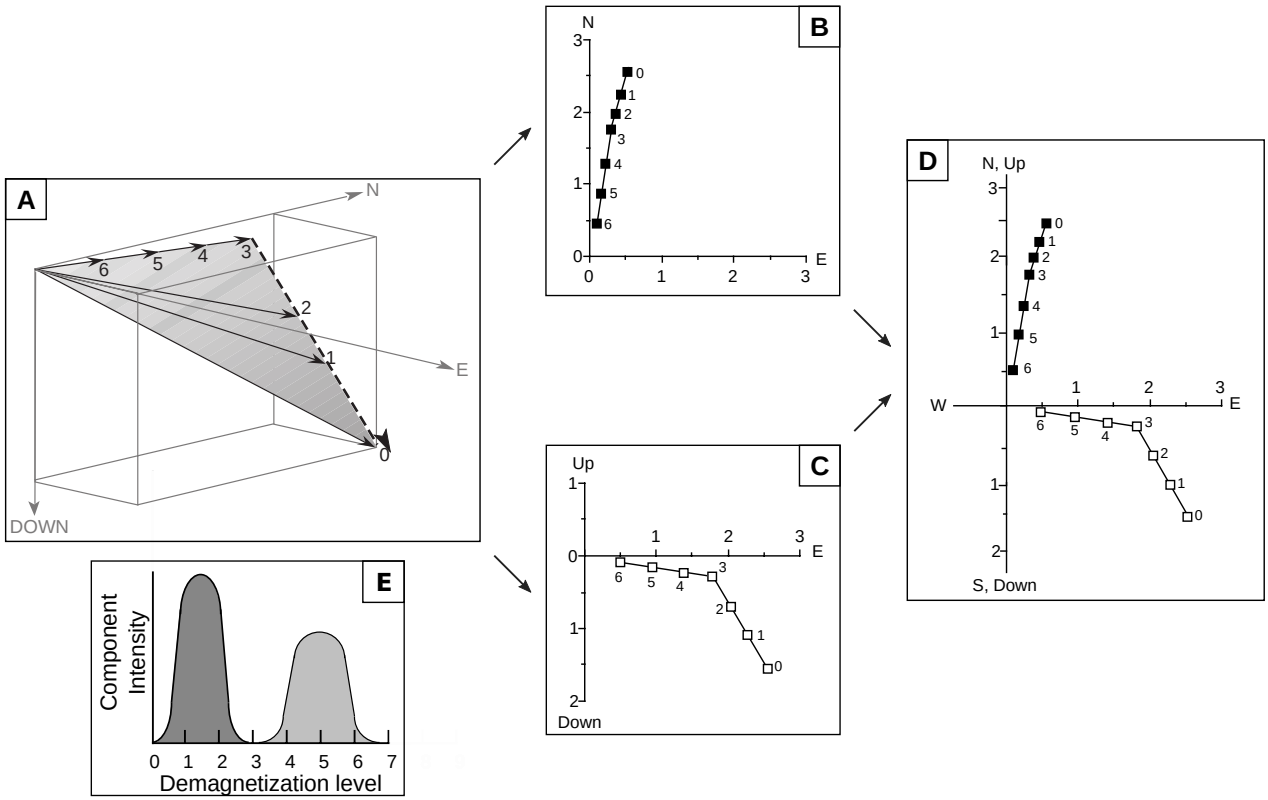

Figure 3.7: Representative demagnetization vector diagrams; A - Perspective view; B - Projection onto the horizontal plane; C - Projection onto the vertical plane; D - Projection of the two orthogonal planes in only one diagram; E - Demagnetization interval for each component (modified from Butler, 1992).

Precambrian rocks usually have more than one overlapping magnetization component, making it more difficult to interpret the data (Dunlop, 1979). Halls (1976, 1978) and Hoffman and Day (1978) developed a technique to analyze multi-component magnetization data (*i.e.* remagnetization circles), however the method didn't allowed to make a jointed analysis with direct observations obtained by Zijderveld diagram interpretation (Zijderveld, 2013). It was only with Kirschvink (1980) and McFadden and McElhinny (1988) that this problem was solved.

3.5.1.1 Thermal Demagnetization

A rock sample is formed by an assemblage of magnetic grains, each with its own T_B. In a null magnetic field room, when the sample is heated to a temperature $T<T_C$, all the grains with $T_B<T$ will have their magnetic moment randomly oriented. Cooling the sample

back to room temperature will make that this new random orientation is preserved. Repeating this procedure slowly increasing the temperature T until $T \geq T_C$ will make that all magnetic moments become randomly oriented (Figure 3.8). Equation 3.5 exemplifies this behavior, all the grains with $T_B<T<T_C$ will present a very low relaxation time (superparamagnetic behavior) therefore the magnetic moment will lose its primary orientation and will align with the local field when the sample is cooled. The new orientation is random because the procedure is performed in a magnetically shielded room. Gradually increasing the temperature will affect all magnetic minerals making that the sample magnetization become approximately null (Creer, 2013; Parry, 2013; Dunlop and Özdemir, 2015; Turner et al., 2015).

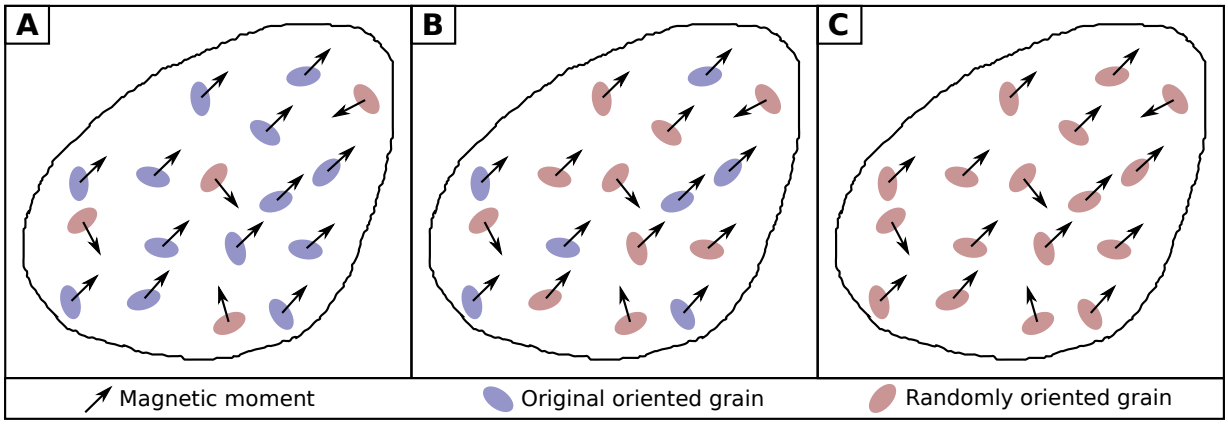

Figure 3.8: Schematic representation of a sample response during an thermal demagnetization; A - Low temperature step; B - Intermediate temperature step; C - High temperature step (adapted from Lowrie and Fichtner, 2007).

3.5.1.2 Alternating Magnetic Field Demagnetization

The coercive force or coercivity (H_C) is the magnetic field intensity required to realign the magnetic moment of a mineral grain. A rock sample is formed by a assemblage of grains, each with its own coercivity. In a null magnetic field environment, when subjecting the sample to an alternating magnetic field (AF) that decay with time in all its directions, the grains with coercivity lower than the intensity of the AF will have its magnetic moments realigned accordingly to the applied field. Repeating this procedure slowly increasing the AF intensity will make the sample magnetization become approximately null (Figure 3.9). Equation 3.5 exemplifies this behavior which can be simplified to $\tau = C_2 \left(1 - \frac{H}{H_c}\right)^2$, where $C_2 = \frac{1}{C} \exp\left(-\frac{Kv}{kT}\right)$, all the grains with $H_C \leq H$ will present a very low relaxation time

therefore the magnetic moment will loose its primary orientation and will align with the applied field. During a step, the magnetic moments of the sample will align upward when the field reaches its maximum peak and downward when the field reaches its minimum peak. The decay of the field over time causes only part of the moments to realign in a same step. In the end, the magnetization will be approximately zero (As, 2013; Parry, 2013; Dunlop and Özdemir, 2015; Turner et al., 2015).

3.5.2 Hysteresis Loops

A hysteresis loop measures the sample magnetization response when subjected to an inductive field. Figure 3.1b demonstrates the usual response of a ferromagnetic material and displays the obtained parameters. The saturation magnetization (M_s) represents the maximum value that the sample magnetization can achieve, the saturation remanent magnetization (M_{rs}) is the magnetization intensity that the sample preserves after reducing the applied field from saturation values back to $H = 0$, the coercive force or coercivity (H_c) is the applied field needed to make $M = 0$ and the remanent coercivity (H_{cr}) is the value that makes the magnetization became null again when increasing the applied field back to $H = 0$ from that starting point.

3.5.3 FORC Diagrams

The First-order Reversal Curve (FORC) diagram (Roberts et al., 2000) is a more recent technique that is used to analyze hysteresis curves in order to characterize the magnetic mineralogy. Basically consists in performing repeated partial hysteresis curves of a sample in order to map all of the curve interior, then it is calculated a mixed second derivative from the data points (Equation 3.10):

$$\rho(B_r, B) = -\frac{1}{2}\frac{\partial^2 M(B_r, B)}{\partial B_r \partial B} \tag{3.10}$$

In order to better visualize the results, a change in the coordinate systems is performed ($B_c = (B_r - B)/2$; $B_i = (B_r + B)/2$), where B_c is the sample coercivity and B_i indicates the magnetic interaction of the minerals (Figure 3.10). The typical responses obtained from FORC diagrams are displayed in Figure 3.11.

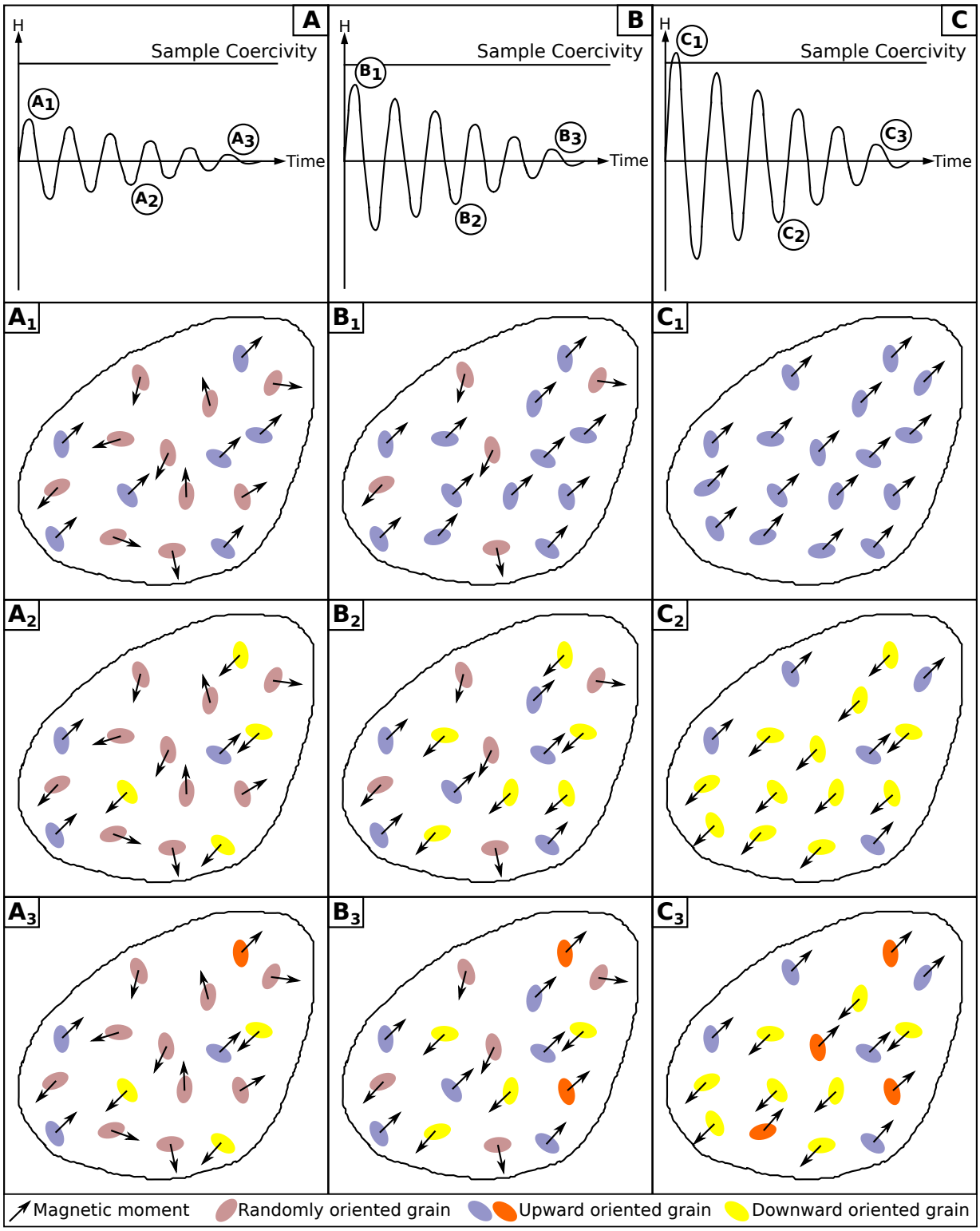

Figure 3.9: Schematic representation of a sample response during an alternating magnetic field demagnetization; A - Low intensity AF applied; B - Intermediate intensity AF applied; C - Low intensity AF applied; A, B and C subplots demonstrate the effects of the AF in the minerals magnetic moments (adapted from Butler, 1992; Lowrie and Fichtner, 2007).

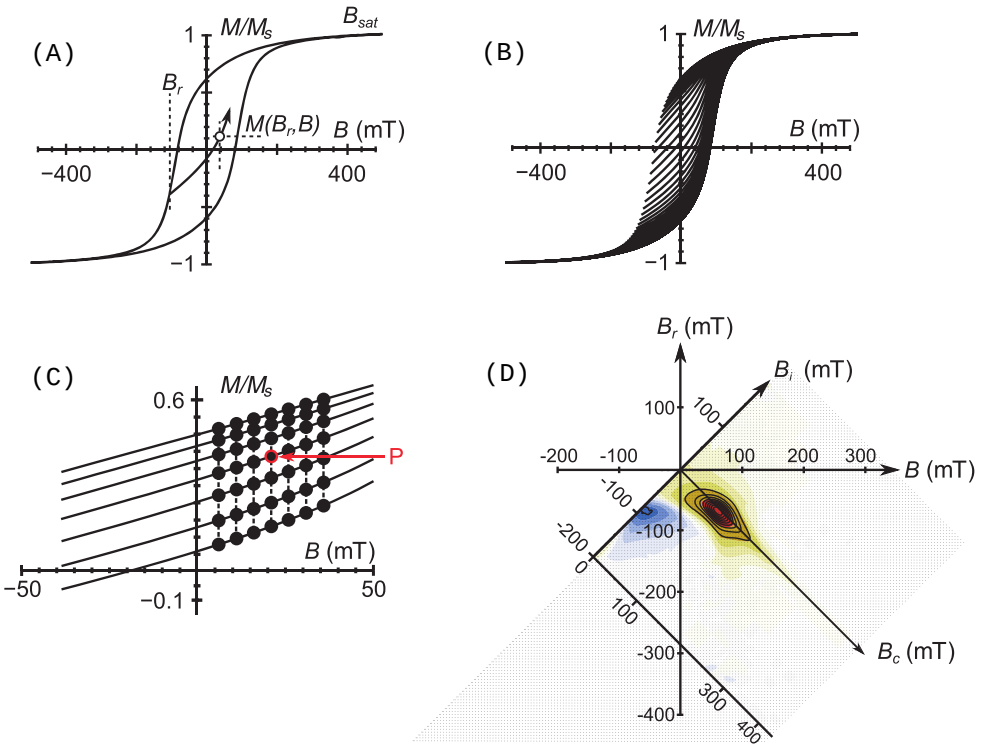

Figure 3.10: A - Definition of FORC measurements; B - Mapped hysteresis; C - FORC data points; D - FORC diagram example (after Roberts et al., 2014).

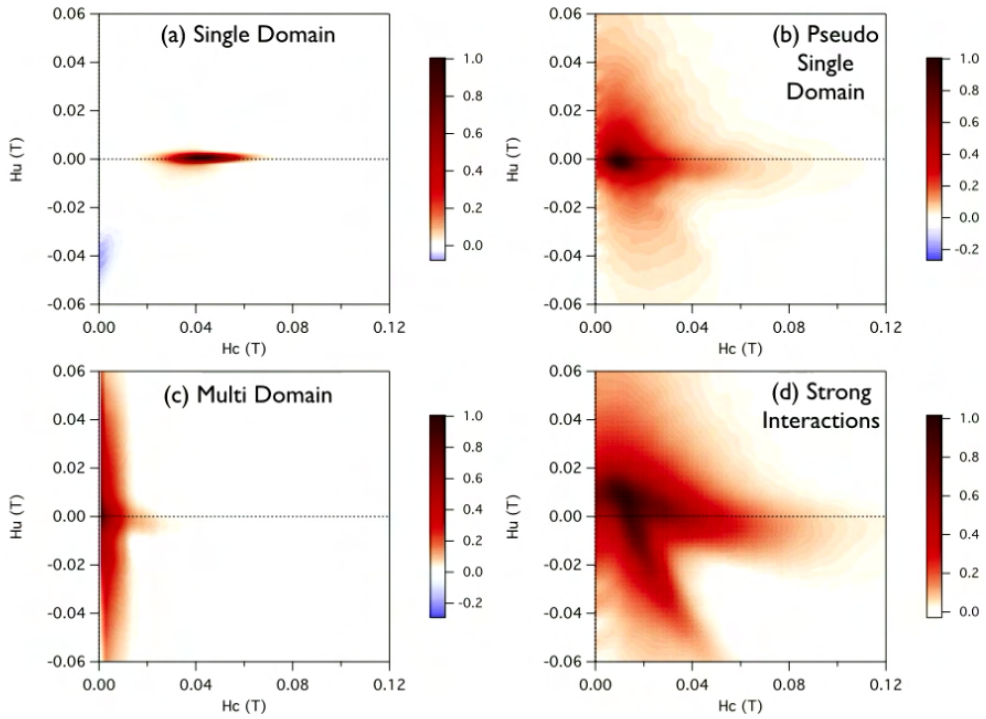

Figure 3.11: Typical FORC results (Roberts, 2015).

3.5.4 Isothermal Remanent Magnetization

Isothermal Remanent Magnetization (IRM) Curves are obtained by progressively subjecting a rock sample to a magnetizing field, in one or more axes as shown in Figure 3.12 (Dunlop, 1972; Lowrie, 1990). Usually a sample is composed of an assemblage of mineral grains with different coercivities, the interpretation of the curves are performed in softwares that can analyze the sample coercivity spectrum , therefore it can separate and characterize each component (Kruiver et al., 2001; Maxbauer et al., 2016).

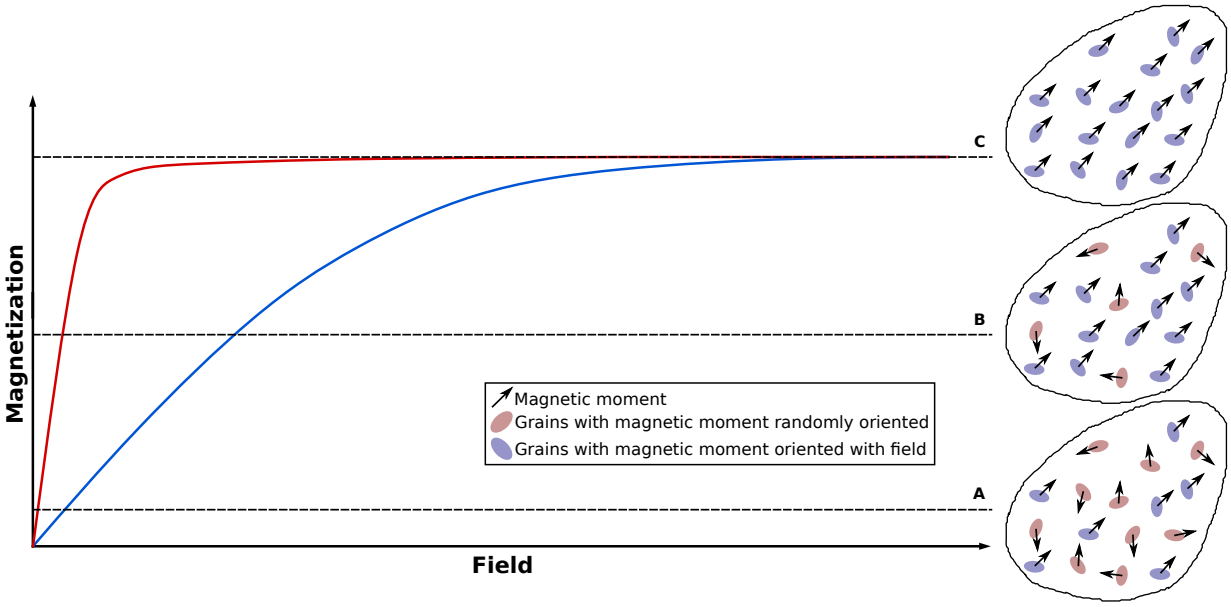

Figure 3.12: Schematic IRM Curve representation. Red and blue lines exemplifies the behavior of a low and high coercivity sample, respectively.

3.5.5 Thermomagnetic Curves

A thermomagnetic curve measures the sample magnetic susceptibility response when subjected to a heating ($-190\ C^{\circ}$ up to $700\ C^{\circ}$) and cooling ($700\ C^{\circ}$ down to ambient temperature) processes (Hrouda, 1994), making it possible to characterize the magnetic mineralogy by estimation of the Curie temperature (Grommé et al., 1969; Tauxe, 2006) and checking for the presence of the Vervey Transition for magnetite ($-150\ C^{\circ}$) and the Morin Transition for hematite ($-15\ C^{\circ}$) (Dunlop and Özdemir, 1997).

There are several ways to estimate the T_C of a sample (*e.g.* Grommé et al., 1969; Moskowitz, 1981; Tauxe, 2006). The Grommé et al. (1969) method analyzes the intersection of two tangents adjusted in the thermomagnetic curve around the T_C, however Petrovskỳ

and Kapička (2006) demonstrated that this method overestimates T_C. The differential method (Tauxe, 2006) estimates T_C by determining the point of maximum curvature in the thermomagnetic curve through analysis of the second derivative of the curve.

3.5.6 *Anisotropy of Magnetic Susceptibility*

The magnetization of a rock in the presence of a weak magnetic field is described by Equation 3.11:

$$\begin{aligned} M_1 &= k_{11}H_1 + k_{12}H_2 + k_{13}H_3 \\ M_2 &= k_{21}H_1 + k_{22}H_2 + k_{23}H_3 \\ M_3 &= k_{31}H_1 + k_{32}H_2 + k_{33}H_3 \end{aligned} \tag{3.11}$$

where M_i $(i = 1, 2, 3)$ are the magnetization components, H_j $(j = 1, 2, 3)$ are the magnetic field intensity components and k_{ij} are the susceptibility tensor. k_{11}, k_{22}, k_{33} are the principals susceptibilities (maximum (K1), intermediate (K2) and minimum (K3), respectively) which represents the orthogonal axes of the susceptibility ellipsoid (K1 $\geq$ K2 $\geq$ K3) that describes the anisotropic behavior of the rock (Hrouda, 1982; Rochette et al., 1992).

The magnetic fabric characterize the shape and orientation of the susceptibility ellipsoid in low-field anisotropy, it is controlled by the assemblage of dia-, para- and ferromagnetic minerals in the rock and is defined by the parameters listed in the Table 3.3 below (Hrouda, 1982; Borradaile, 1987; Rochette et al., 1992; Tarling and Hrouda, 1993). In order to estimate the parameters and direction of the principal susceptibilities usually is used the Jelínek statistics (Jelínek, 1977; Jelínek and Kropáček, 1978).

Table 3.3 - Main AMS ellipsoid parameters.

Mean Susceptibility (K_m)	$(K1 + K2 + K3)/3$
Magnetic Lineation (L)	$K1/K2$
Magnetic Foliation (F)	$K2/K3$
Anisotropy Degree (P)	$K1/K3$
Ellipsoid Shape (T)	$2\ ln(K2/K3)/ln(K1/K3) - 1$

The ellipsoide shape defines if the fabric is neutral (T= 0), oblate ($0 < T \leq 1$) or prolate ($0 > T \geq 1$).

3.5.6.1 Anisotropy of Anhysteretic Remanent Magnetization

The Anisotropy of Anhysteretic Remanent Magnetization (AARM) is performed in order to ensure that the sample AMS is carried mostly by ferromagnetic minerals. The procedure consists in applying at predetermined positions a decreasing AF field while a direct field (bias field) of small intensity is activated (Jackson, 1991; Agico Inc., 2017), then the magnetization tensor is calculated using the Jelínek statistics (Jelínek, 1977; Jelínek and Kropáček, 1978).

Chapter 4

Results

The data analyses and plots were made using Anaconda Environment, PmagPy Software Package, Remasoft and Anysoft (Chadima and Hrouda, 2006; Chadima and Jelinek, 2009; Anaconda Team, 2016; Tauxe et al., 2016).

4.1 Thermomagnetic Curves

All thermomagnetic curves were measured in a argon atmosphere using a Kappabridge KLY4 coupled with a CS3 (high temperature) or CS-L (low temperature) apparatus (Agico Inc.^{TM}). The high temperature curves are depicted in Figure 4.1 and the low temperature curves in Figure 4.2, it is possible to note that some rhyolite samples didn't provided a good outcome with noisy results given their relatively weak magnetic susceptibility. The T_C of the magnetic minerals were estimated by calculating the second derivative of high temperature curves (Tauxe, 2006) and results are displayed in Table 4.1 and Table 4.2. Individual samples results are presented in Appendix A.

Table 4.1 - T_C of representative mafic dykes samples.

Site ID	Heating $T_C[°C]$	Cooling $T_C[°C]$
SJ	577.5	576.1
SM01	587.6	588.4
SM02	590.9	591.4
SM03	579.0	582.3
SM04	583.8	591.3
SM05	582.5	581.2
SM06	609.2	579.2
SM07	579.0	581.0
SM08	581.5	582.8

Table 4.2 - T_C of representative rhyolites samples.

Site ID	Heating $T_C[°C]$	Cooling $T_C[°C]$
CR01	594.5	596.3
CR02	595.9	595.7
CR03	597.9	595.9
CR04	388.2	637.6
CR05	460.8	600.3
CR06	590.9	644.0
CR07	530.5	700.5

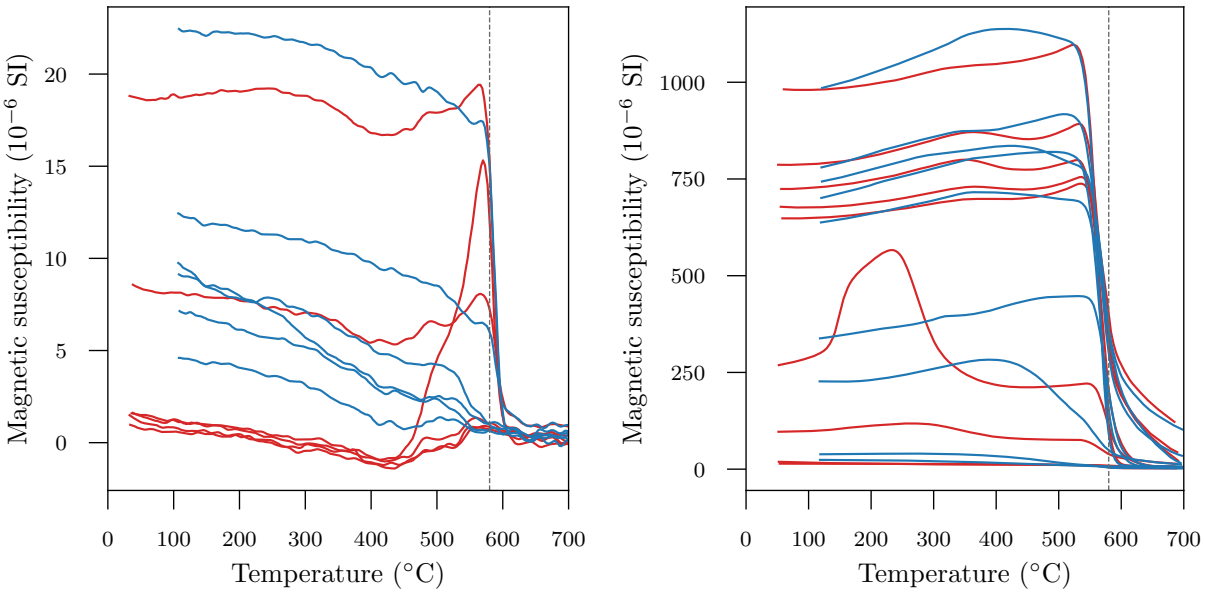

(a) Rhyolites samples *(b)* Mafic dykes samples

Figure 4.1: High temperature thermomagnetic curves of representative samples from the studied sites (heating curves in red and cooling curves in blue - dashed line indicates the T_C of magnetite [580 °C]).

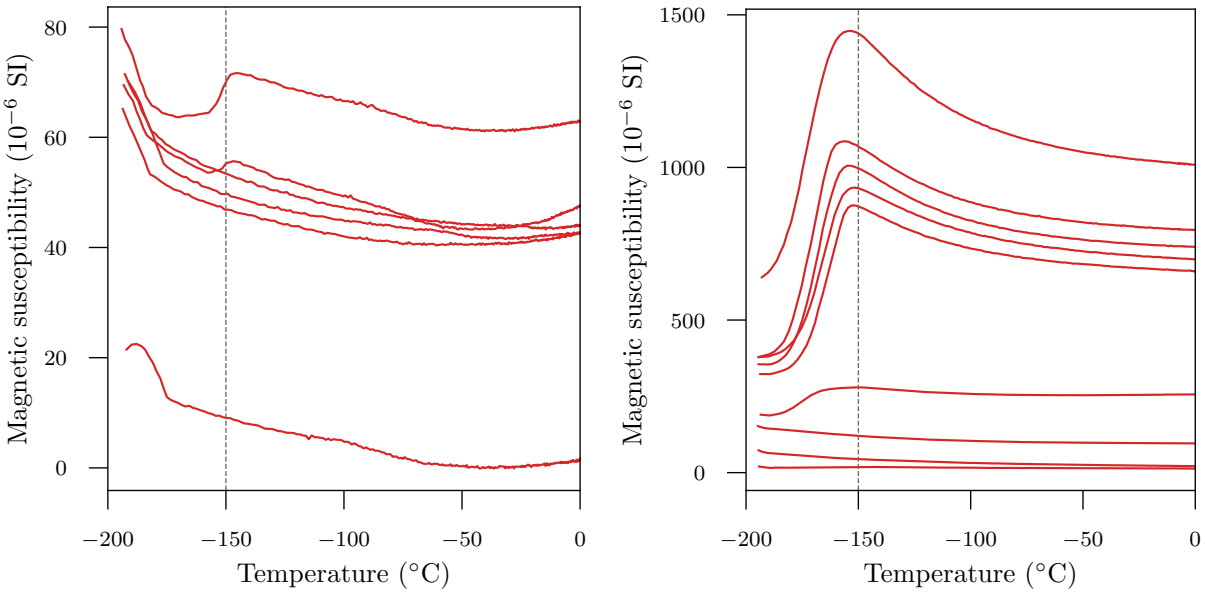

(a) Rhyolites samples *(b)* Mafic dykes samples

Figure 4.2: Low temperature thermomagnetic curves of representative samples from the studied sites (dashed line indicates the Vervey Transition temperature of magnetite [-150 °C]).

The T_C estimated values and the increase of magnetic susceptibility near −150°C indicates that the main magnetic carrier is magnetite. However, for some mafic dykes samples the magnetic susceptibility doesn't drop to 0 at the T_C of pure magnetite. These samples likely have a certain amount of hematite whose transition temperature is typically 680 °C.

4.2 FORC Diagrams

FORC diagrams were measured in a Princeton Measurements Corporation Micromag Vibrating Sample Magnetometer (VSM) at room temperature in a representative sample of each rhyolite site and at the processing analyses it was employed a smoothing factor of 20. All samples exhibit a characteristic behavior of a mixture paramagnetic + MD + PSD grains (Figure 4.3), except CR04 and CR07 whose FORC were too noisy to allow any readable map.

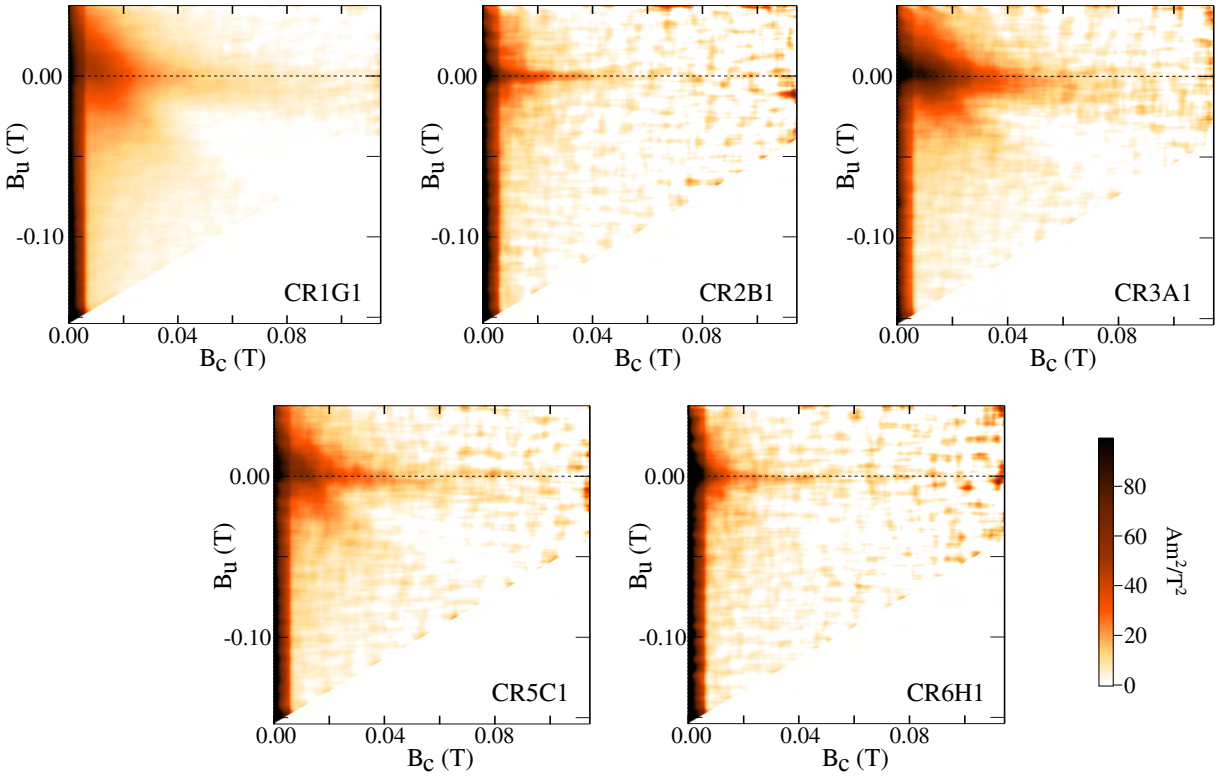

Figure 4.3: FORC diagrams of representative rhyolite samples.

4.3 Hysteresis Loops

Hysteresis loops were measured in a Princeton Measurements Corporation Micromag Vibrating Sample Magnetometer (VSM) at room temperature. Individual samples hysteresis loops are displayed in Appendix B. The sample collection hysteresis loops obtained are displayed in Figure 4.4 below. According to Figure 8.11 of Tauxe et al. (2018), the rhyolite samples presented a dominance of paramagnetic particles (except CR1G1 which presented a ferromagnetic behavior) and all mafic dykes samples exhibited a ferromagnetic pattern,

SM02 and SM07 presented a pseudo-single domain behavior. CR04 and SM06 are mainly composed of paramagnetic minerals. The hysteresis parameters estimated after applying the dia/paramagnetic correction are displayed in Table 4.3 and the corresponding Day's diagram (Day et al., 1977) is shown in Figure 4.5. Figure 4.6 represents an alternative to the Day's diagram proposed by Tauxe et al. (2002). On both diagrams it is evident the dominance of MD particles in the rhyolite samples.

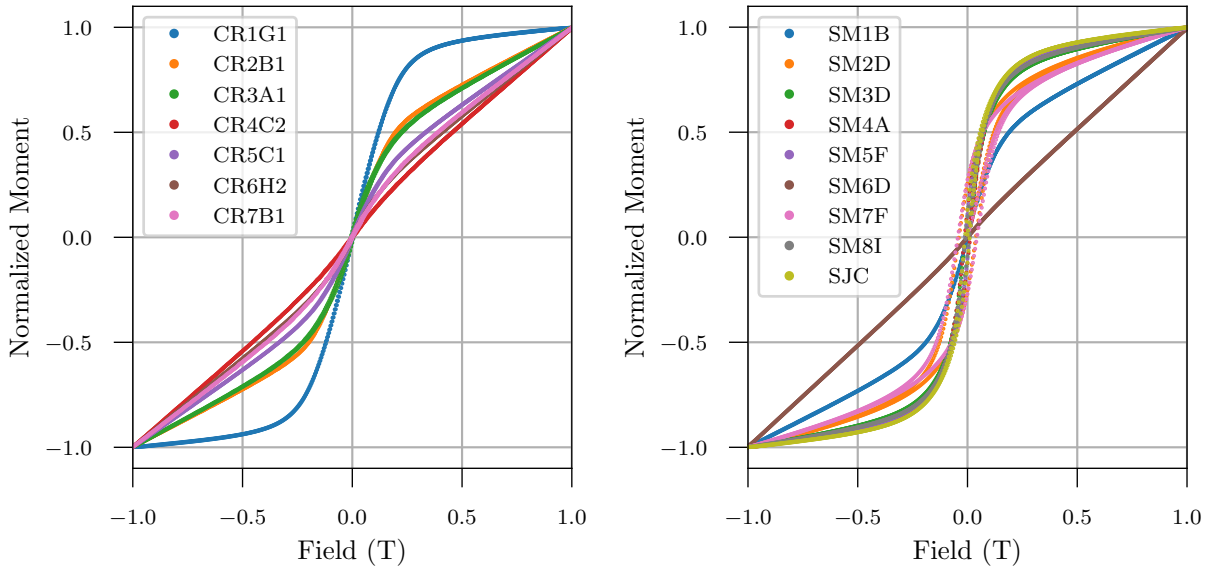

(a) Rhyolites samples

(b) Mafic dykes samples

(c) Rhyolites samples

(d) Mafic dykes samples

Figure 4.4: Hysteresis loops of representative site samples (*a*, *b* are the original hysteresis loops and *c*, *d* represents the data after dia/paramagnetic correction).

Table 4.3 - Hysteresis parameters of representative site samples

Sample	M_s $[mAm^2/kg]$	M_{rs} $[mAm^2/kg]$	H_c $[mT]$	H_{cr} $[mT]$	Sample	M_s $[mAm^2/kg]$	M_{rs} $[mAm^2/kg]$	H_c $[mT]$	H_{cr} $[mT]$
CR1G1	529.93	10.07	3.61	36.14	SM1B	68.82	0.78	1.43	16.67
CR2B1	39.62	0.74	2.95	34.52	SM2D	1142.79	393.14	40.59	63.20
CR3A1	39.09	2.41	8.39	38.47	SM3D	1128.93	134.61	10.02	21.76
CR4C2	4.56	0.23	8.40	38.99	SM4A	1657.12	242.01	12.68	24.38
CR5C1	25.00	0.95	5.29	35.24	SM5F	1491.71	184.49	9.86	20.00
CR6H2	12.23	0.27	2.69	25.94	SM6D	8.01	0.38	5.32	28.88
CR7B1	10.23	0.39	6.17	34.96	SM7F	759.69	300.47	45.61	71.66
SJC	2230.10	315.07	10.77	19.73	SM8I	1443.66	158.76	8.84	18.83

(M_s = Saturation Magnetization; M_{rs} = Saturation Remanent Magnetization; H_c = Coercivity; H_{cr} = Remanent Coercivity).

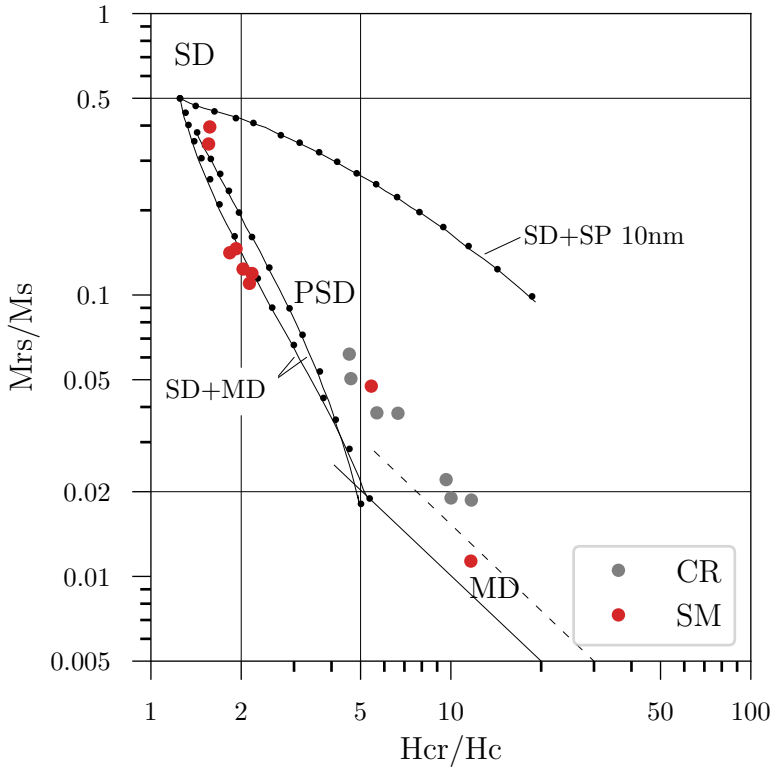

Figure 4.5: Day's diagram (Day et al., 1977) of the studied samples (particles limits and mixing curves after Dunlop (2002a,b)).

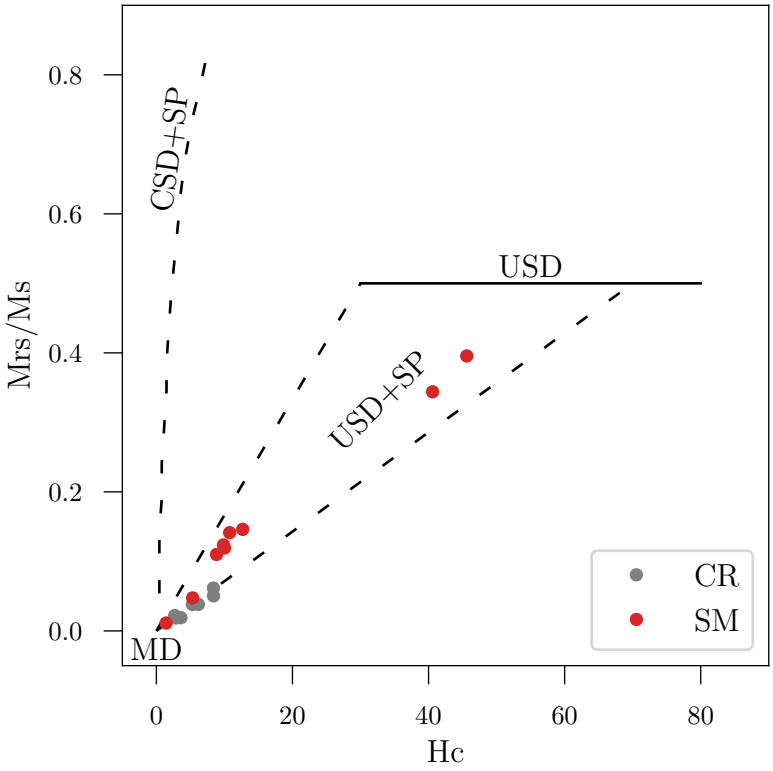

Figure 4.6: Tauxe et al. (2002) alternative $M_{rs}/M_s \times H_c$ diagram (CSD = cubic single domian; USD = uniaxial single domain).

4.4 *Isothermal Remanent Magnetization Curves*

IRM curves were measured in a Princeton Measurements Corporation Micromag Vibrating Sample Magnetometer (VSM) at room temperature. Most rhyolite samples results were of poor quality due to the low remanence of the samples achieving saturation vary rapidly around 200 mT, except CR2B1 and CR3A1 indicating the presence of a high coercivity mineral (Figure 4.7a). The mafic dykes provided some better quality results and saturate in even lower field intensity then the rhyolite samples (Figure 4.7b). In order to characterize the samples mineralogy, it was performed a decomposition of the IRM curves using the MAXUnMix Software (Maxbauer et al., 2016). The parameters obtained are shown in Table 4.5 and Table 4.4 (individual samples results are displayed in Appendix C).

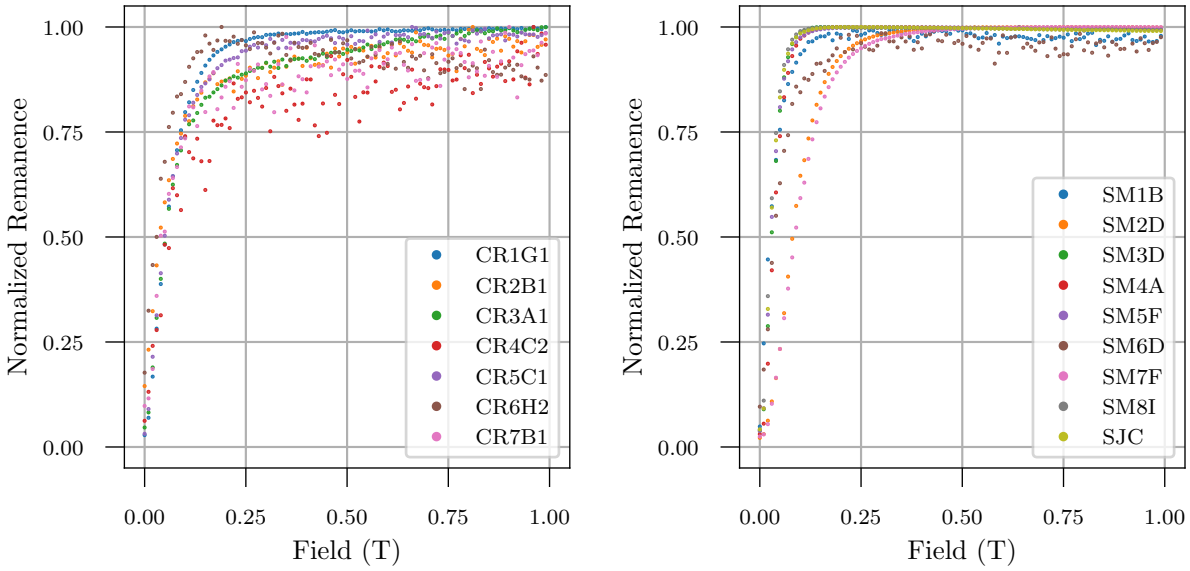

(a) Rhyolites samples

(b) Mafic dykes samples

Figure 4.7: IRM curves of representative site samples.

Table 4.4 - IRM unmixing parameters of mafic dyke samples

	SJC	SM1B			SM2D		
	Comp 1	Comp 1	Comp 2	Comp 3	Comp 1	Comp 2	Comp 3
Bh	25.86 (±1.50)	32.4 (±1.07)	245.54 (±1.08)	688.19 (±1.13)	74.66 (±1.04)	168.41 (±1.05)	46.09 (±1.22)
DP	2.00 (±1.35)	2.28 (±1.05)	1.42 (±1.09)	1.9 (±1.15)	1.44 (±1.03)	1.33 (±1.03)	2.48 (±1.15)
P	0.98 (±0.02)	1.01 (±0.01)	0.16 (±0.03)	0.11 (±0.01)	0.84 (±0.05)	0.43 (±0.07)	0.18 (±0.04)
S	0.90 (±0.07)	0.92 (±0.06)	1.06 (±0.13)	1.16 (±0.13)	0.82 (±0.09)	2.00 (±0.22)	1.11 (±0.16)
OC	1	0.85 (±0.01)	0.08 (±0.08)	0.07 (±0.05)	0.52 (±0.16)	0.20 (±0.10)	0.28 (±0.20)
EC	1	0.87 (±0.01)	0.06 (±0.05)	0.07 (±0.05)	0.55 (±0.14)	0.17 (±0.08)	0.29 (±0.21)

	SM3D	SM4A	SM5F	SM7F			SM8I
	Comp 1	Comp 1	Comp 1	Comp 1	Comp 2	Comp 3	Comp 1
Bh	27.93 (±1.19)	33.16 (±1.07)	26.47 (±1.87)	103.60 (±1.04)	140.11 (±1.09)	63.59 (±1.08)	23.28 (±2.55)
DP	1.99 (±1.14)	1.87 (±1.05)	2.06 (±1.60)	1.66 (±1.02)	1.17 (±1.10)	2.34 (±1.05)	2.12 (±2.02)
P	0.99 (±0.01)	1.00 (±0.01)	0.98 (±0.02)	0.68 (±0.05)	0.13 (±0.04)	0.34 (±0.04)	0.98 (±0.02)
S	0.79 (±0.05)	0.89 (±0.03)	0.90 (±0.07)	1.12 (±0.09)	1.67 (±0.18)	1.20 (±0.08)	0.83 (±0.07)
OC	1	1	1	0.53 (±0.17)	0.03 (±0.05)	0.44 (±0.16)	1
EC	1	1	1	0.53 (±0.18)	0.01 (±0.04)	0.45 (±0.17)	1

(Bh = Mean coercivity; DP = Dispersion parameter; P = Component proportion; S = Skewness; OC = Observed contribution to the total magnetization; EC = Extrapolated contribution to the total magnetization).

Table 4.5 - IRM unmixing parameters of rhyolite samples

	CR1G1		CR2B1		CR3A1		CR5C1	
	Comp 1	Comp 2	Comp 1	Comp 2	Comp 1	Comp 2	Comp 1	Comp 2
Bh	41.13 (±1.10)	184.55 (±1.08)	42.74 (±1.14)	453.87 (±1.15)	44.81 (±1.08)	558.12 (±1.23)	36.09 (±1.11)	194.69 (±1.12)
DP	2.19 (±1.08)	1.44 (±1.05)	2.46 (±1.09)	1.89 (±1.21)	2.49 (±1.04)	1.86 (±1.34)	2.43 (±1.06)	1.45 (±1.14)
P	0.96 (±0.02)	0.26 (±0.06)	0.94 (±0.02)	0.25 (±0.01)	0.93 (±0.02)	0.24 (±0.02)	0.92 (±0.05)	0.32 (±0.05)
S	0.61 (±0.04)	1.91 (±0.26)	0.85 (±0.05)	0.85 (±0.15)	0.89 (±0.07)	1.15 (±0.28)	0.62 (±0.04)	1.13 (±0.15)
OC	0.89 (±0.04)	0.11 (±0.06)	0.86(±0.04)	0.14 (±0.09)	0.88 (±0.08)	0.12 (±0.10)	0.89 (±0.13)	0.11 (±0.10)
EC	0.90 (±0.05)	0.10 (±0.06)	0.84 (±0.04)	0.16 (±0.11)	0.85 (±0.07)	0.15 (±0.16)	0.86 (±0.10)	0.14 (±0.11)

(Bh = Mean coercivity; DP = Dispersion parameter; P = Component proportion; S = Skewness; OC = Observed contribution to the total magnetization; EC = Extrapolated contribution to the total magnetization).

4.5 Anisotropy of Magnetic Susceptibility

The AMS data of individual samples were acquired in a Kappabridge MFK1-A (Agico^{TM}) and the AARM data were acquired using a LDA-3 AF Demagnetizer coupled with a AMU-1 Anhysteretic Magnetizer and a JR-6 Magnetometer (Agico^{TM}).

The results obtained from the AMS characterization of each studied site are displayed in Figure 4.8 and Table 4.6 below. An AARM study on two samples of each rhyolite site was also performed. Only SM01 and SM06 sites provided coherent AMS results from the mafic dykes samples and all CR sites clustered in common direction, except CR04 site which yielded a different direction. The AARM analyses of the sites CR01, CR02, CR05 and CR07 provided similar direction to that of AMS.

The T-P diagram of the mafic dykes (Figure 4.11) determined that only SM01 site exhibit higher values of anisotropy degree (P) and that the anisotropy ellipsoids do not have a preferred shape. The K-P diagram of the mafic dykes (Figure 4.12) show that the samples had a low value of mean susceptibility (< 0.07 SI) clustering around 0.05 SI and that most sites have its anisotropy characterized by ferromagnetic particles.

The rhyolite analysis provided three important characteristics. The magnetic grains have preferred oblate shape, presented a very low value of mean susceptibility, around $0.0001 < K_m < 0.0004$ SI, (Figure 4.10) and that the samples had 0.01 - 0.001 % of magnetite in its composition (Figure 4.9), agreeing with Zincone et al. (2016) which performed a whole-rock geochemistry providing a percentage of ferromagnesian elements $Fe_2O_3 + MgO + MnO + TiO_2 < 4.4$ wt.%.

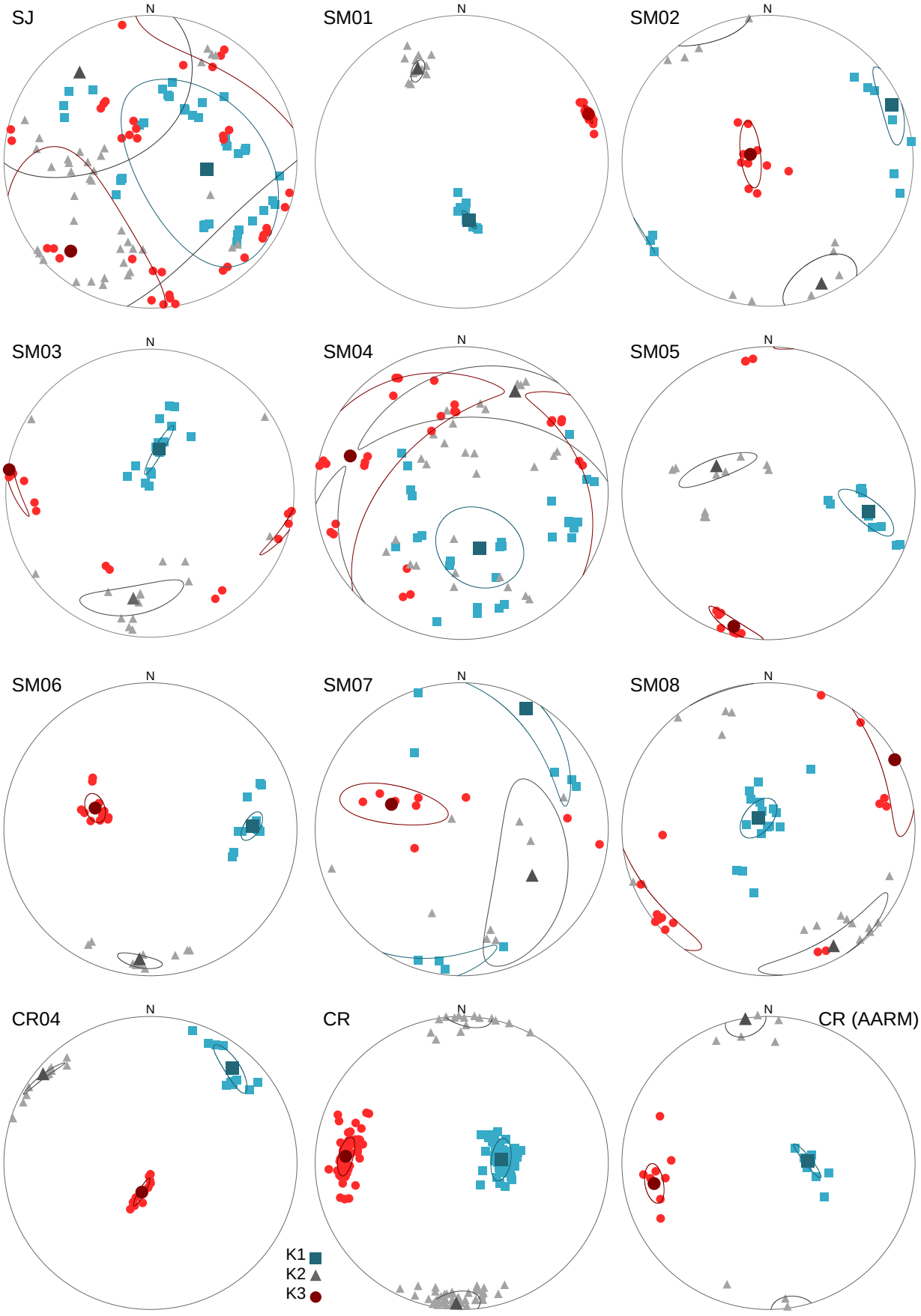

Figure 4.8: ASM results of all samples (CR sites are plotted all together, except CR04) and AARM of some CR samples.

Table 4.6 - AMS data from the studied sites

Site ID	n/N	$K_m(SI)$	P	T	L	F	K_1	$\varepsilon_{12}(K_1)$	K_2	$\varepsilon_{23}(K_2)$	K_3	$\varepsilon_{31}(K_3)$
SJ	38/38	5.20E-02 (7.53E-03)	1.032 (0.008)	-0.284 (0.447)	1.021 (0.009)	1.011 (0.007)	97.5/58.1	60.0/36.7	320.8/24.4	59.9/52.7	221.7/19.3	52.9/36.7
SM01	14/14	1.69E-02 (6.37E-03)	1.582 (0.130)	0.345 (0.206)	1.171 (0.084)	1.352 (0.061)	172.6/57.1	6.4/1.6	334.2/31.6	6.7/3.2	69.4/8.4	4.3/1.0
SM02	10/15	3.26E-02 (1.26E-02)	1.018 (0.006)	-0.122 (0.309)	1.010 (0.004)	1.008 (0.004)	65.8/7.3	17.6/7.4	156.7/7.1	19.3/16.0	290.4/79.8	18.8/5.6
SM03	15/24	5.05E-02 (9.93E-03)	1.041 (0.008)	0.012 (0.245)	1.021 (0.008)	1.020 (0.003)	11.1/64.8	16.2/2.3	189.0/25.1	26.6 /9.0	279.4/0.8	24.7/2.6
SM04	28/28	4.08E-02 (1.07E-02)	1.031 (0.012)	0.371 (0.402)	1.008 (0.005)	1.023 (0.013)	162.1/57.2	26.0/21.1	28.2/24.0	84.8/16.8	288.4/20.9	84.8/25.3
SM05	10/19	4.14E-02 (3.89E-03)	1.045 (0.005)	-0.585 (0.130)	1.036 (0.006)	1.009 (0.002)	100.4/31.4	20.8/6.0	295.5/57.7	23.2/5.6	194.6/6.8	14.6/3.9
SM06	11/13	8.08E-04 (5.61E-05)	1.052 (0.010)	0.510 (0.199)	1.013 (0.005)	1.039 (0.008)	88.4/31.2	8.6/4.5	184.7/10.4	9.9/4.4	291.0/56.7	8.4/5.3
SM07	9/9	5.42E-03 (4.10E-03)	1.023 (0.013)	0.163 (0.328)	1.009 (0.006)	1.014 (0.010)	28.0/7.6	51.0/8.9	124.7/41.2	52.5/21.1	289.5/47.8	32.8/10.0
SM08	16/27	5.24E-02 (4.45E-03)	1.024 (0.005)	-0.053 (0.308)	1.013 (0.005)	1.011 (0.004)	318.0/81.6	12.8/7.7	151.4/8.1	32.7/8.4	61.1/1.9	33.1/10.5
CR01	17/19	8.50E-03 (7.97E-03)	1.342 (0.155)	0.470 (0.160)	1.085 (0.052)	1.233 (0.087)	91.2/70.5	9.6/3.2	357.8/1.2	8.9/6.7	267.3/19.5	7.0/4.5
CR02	11/11	5.29E-03 (9.95E-03)	1.273 (0.143)	0.435 (0.149)	1.075 (0.052)	1.181 (0.073)	65.7/68.8	6.4/1.6	180.4/9.2	8.1/3.2	273.6/18.9	6.4/1.1
CR03	8/11	2.45E-04 (4.96E-05)	1.180 (0.039)	0.501 (0.250)	1.042 (0.022)	1.133 (0.039)	82.3/66.2	5.9/2.3	182.1/4.3	8.7/3.2	273.9/23.3	7.6/1.5
CR04	11/13	1.56E-04 (1.64E-05)	1.184 (0.024)	0.627 (0.056)	1.032 (0.003)	1.147 (0 024)	40.7/15.5	13.4/5.1	308.8/6.6	11.5/1.4	169.5/73.1	8.9/1.6
CR05	5/7	2.58E-04 (7.06E-05)	1.158 (0.010)	0.572 (0.087)	1.032 (0.008)	1.122 (0.005)	111.0/71.7	13.9/4.8	16.7/1.4	13.5/4.2	286.3/18.3	7.2/3.8
CR06	10/10	1.87E-04 (4.09E-05)	1.190 (0.036)	0.588 (0.174)	1.039 (0.027)	1.146 (0.010)	83.1/60.6	8.9/2.1	184.8/6.5	11.1/3.5	278.4/28.5	7.9/1.8
CR07	9/10	1.95E-04 (4.90E-05)	1.152 (0.028)	0.627 (0.127)	1.026 (0.008)	1.123 (0.026)	94.0/62.6	8.6/3.3	190.6/3.4	11.7/4.1	282.4/27.1	9.2/2.9
CR mean*	60/68	3.50E-03 (6.90E-03)	1.239 (0.127)	0.517 (0.176)	1.057 (0.044)	1.170 (0.073)	85.2/68.0	11.6/5.5	182.2/2.8	11.7/8.7	273.3/21.8	9.4/4.8
CR (AARM)	8/15	7.07E-04 (8.23E-04)	1.391 (0.266)	0.243 (0.307)	1.138 (0.121)	1.216 (0.125)	086.6/68.1	11.9/2.0	350.7/2.3	11.3/8.1	259.8/21.7	9.2/6.2

(n/N = Number of samples used to calculated the AMS mean/number of samples analyzed; K_m = Mean magnetic susceptibility; P = Anisotropy degree; T = Ellipsoid shape; L = Magnetic lineation; F = Magnetic foliation; () = Standard deviation; K_i = Declination/Inclination of main magnetic susceptibilities; ε_i = Error associated with K_i)

* site CR04 was not utilized to calculate de mean

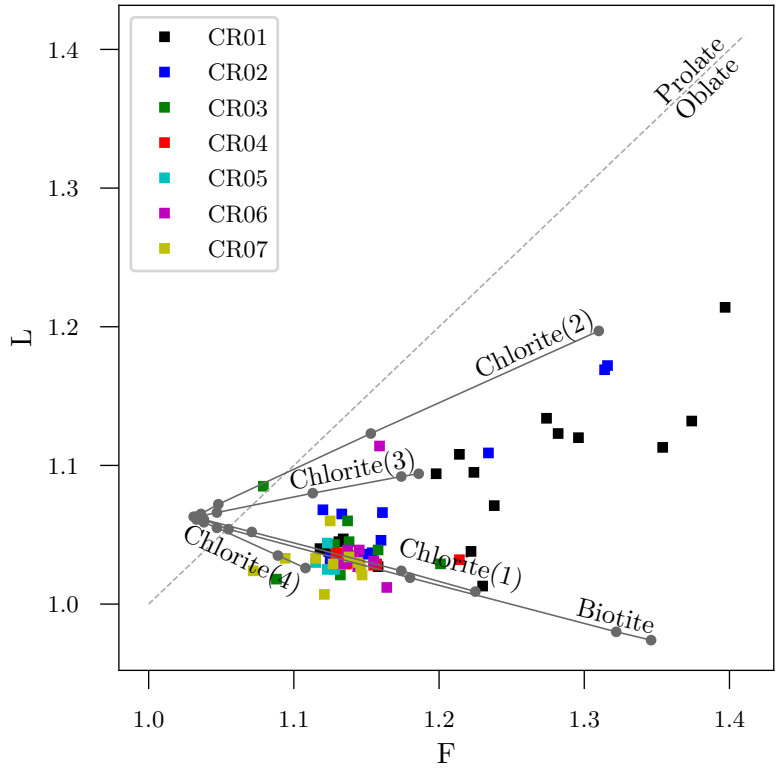

Figure 4.9: L-F diagram of the rhyolite samples. From right (0.0001%) to left (1%), each dot in the gray lines indicates a 10x increase in the magnetite percentage (after Borradaile, 1987).

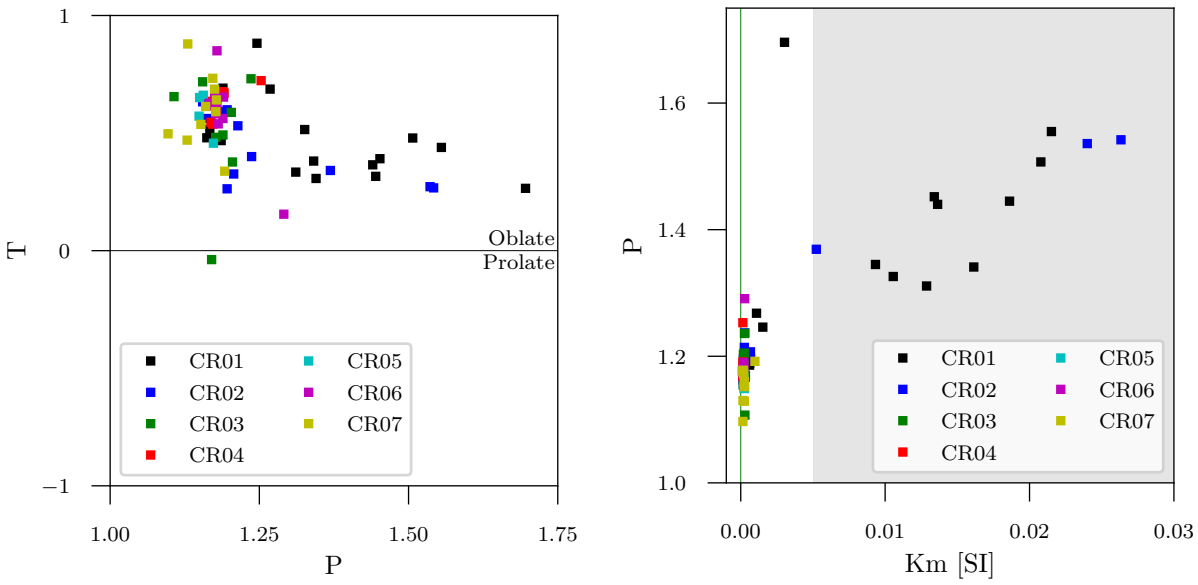

Figure 4.10: T-P diagram (left) and K-P diagram (right) of rhyolite samples (values below the green line indicates diamagnetic particles and gray area represents the ferromagnetic particles, according to Cañón-Tapia (2004)).

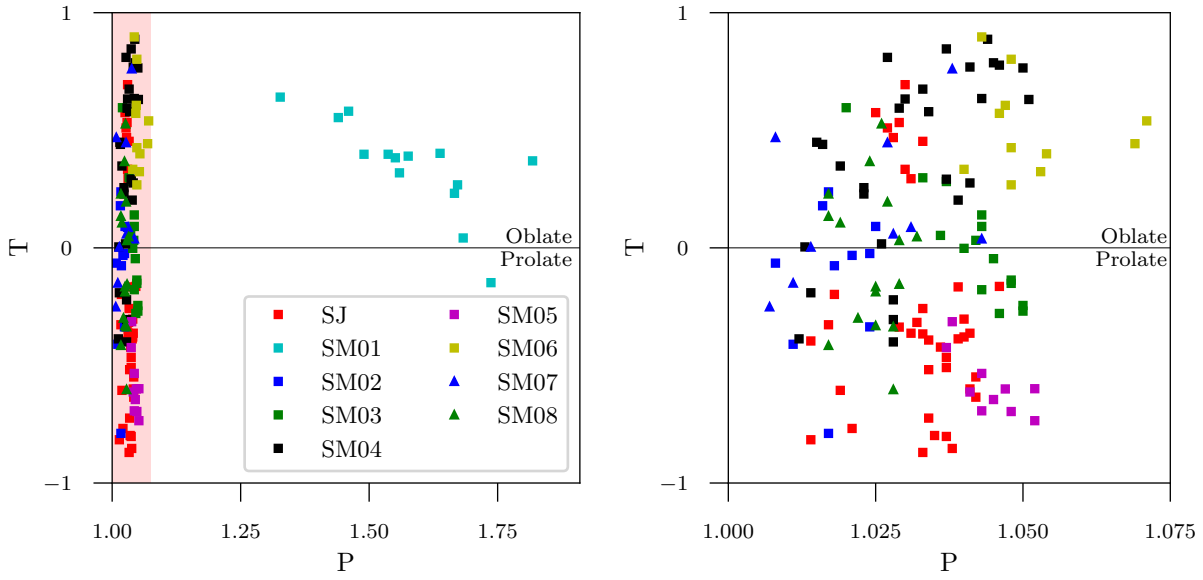

Figure 4.11: T-P diagram of mafic dikes samples. Right side plot represents a zoom of the pinkish area of the left side plot.

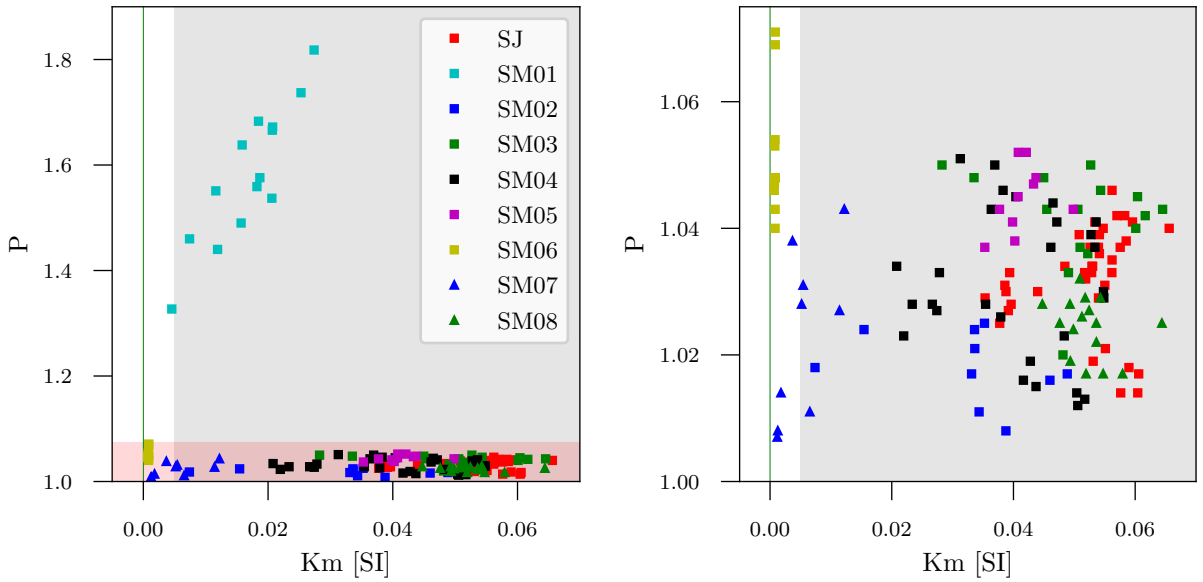

Figure 4.12: K-P diagram of mafic dikes samples. Right side plot represents a zoom of the pinkish area of the left side plot (values below the green line indicates diamagnetic particles and gray area represents the ferromagnetic particles, according to Cañón-Tapia (2004)).

4.6 Paleomagnetism

In order to obtain the paleomagnetic information, the samples were subjected to alternating magnetic field and thermal demagnetization procedures.

The AF demagnetization of sites SJ, SM02, SM03, SM04, SM05, SM07 and SM08 were performed in a LDA-5 AF Demagnetizer (Agico^{TM}) and the directional data were acquired in a JR-6 Magnetometer (Agico^{TM}). The AF demagnetization and the directional data acquisition of sites SM01, SM06 and CR were performed in a cryogenic SQUID magnetometer coupled with a AF coil (2G-Enterprises^{TM}). Each site had its own AF protocol as demonstrated in Table 4.7.

Table 4.7 - AF protocol of each site.

SM01	2, 3, 4, 5, 6, 7, 8, 9, 10, 15, 20, 25, 30, 35, 40, 45, 50, 55, 60, 65, 70, 75, 80, 85, 90, 95, 100 [mT]
SM02, SM03, SM04, SM05, SM08	2, 3, 4, 5, 6, 7, 8, 9, 10, 12, 14, 17, 20, 25, 30, 35, 40, 50, 60, 70, 80, 90, 100 [mT]
SM06, SM07	2, 3, 4, 6, 8, 10, 12, 15, 20, 25, 30, 35, 40, 45, 50, 55, 60, 65, 70, 75, 80, 85, 90, 95, 100 [mT]
SJ	2, 4, 6, 8, 10, 12, 14, 16, 18, 20, 25, 30, 35, 40, 45, 50, 55, 60, 65, 70, 80, 90, 100 [mT]
CR	2, 4, 6, 8, 10, 12, 14, 16, 18, 20, 25, 30, 35, 40, 45, 50 ,55 , 60, 65, 70 ,75, 80, 85, 90, 95, 100 [mT]

The samples provided two sets of directional data. One was obtained in the initial AF steps and another obtained in the final AF steps. Individual specimens results are shown in Figure 4.13, demonstrating the type of demagnetization characteristics found in the samples.

The thermal demagnetization treatment was performed according to the following procedures. Prior to the heating process, the samples were subjected to a Low Temperature Demagnetization (LTD) associated with a low intensity AF demagnetization (2, 4, 6, 8 and 10 mT steps) performed in a LDA-5 AF Demagnetizer (Agico^{TM}), in order to remove the multi-domain component of the magnetization information (Merrill, 1970; Borradaile, 1994). This procedure will be referred here as pre-thermal treatment.

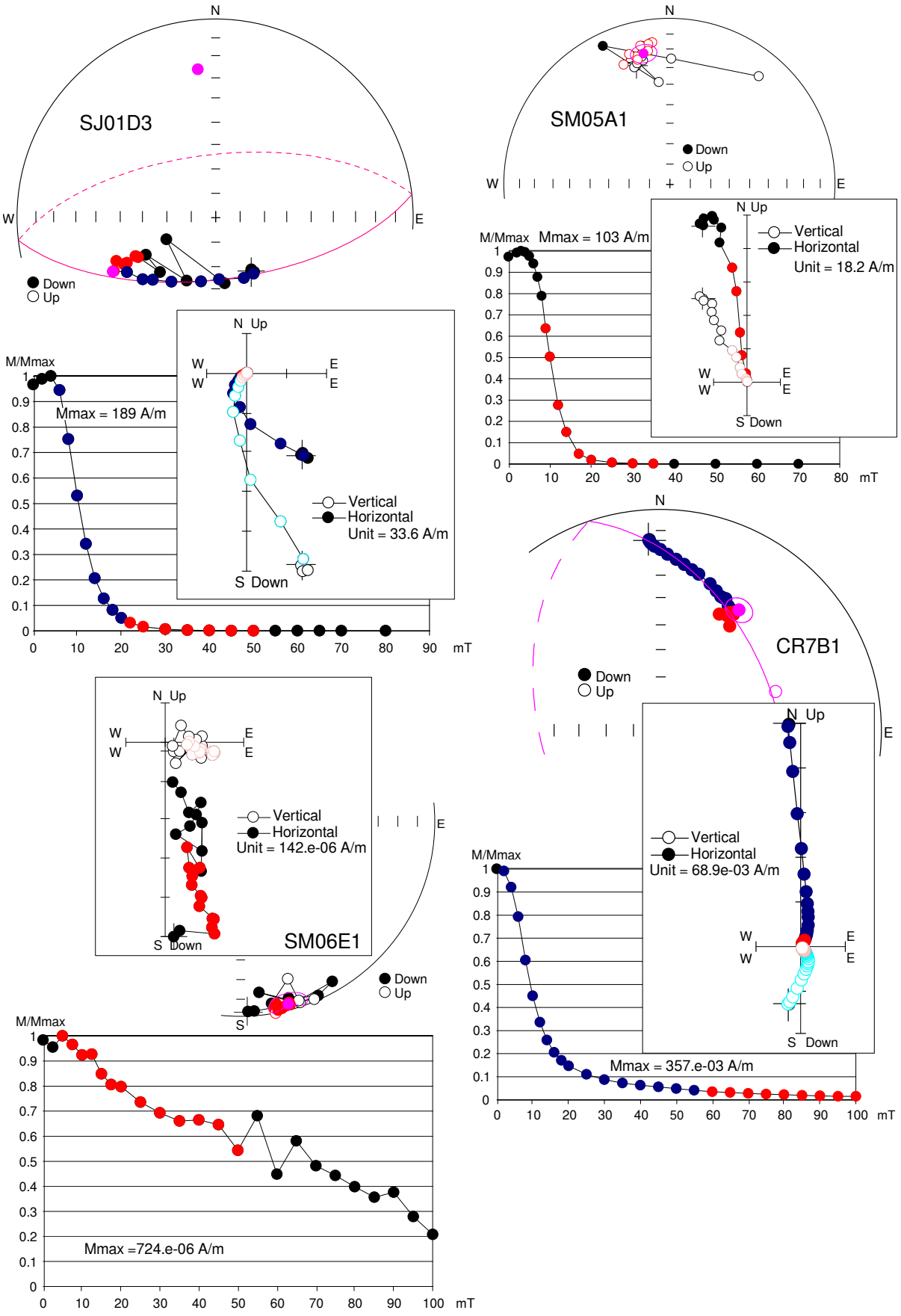

Figure 4.13: Individual samples AF demagnetization characteristics (colored dots represents the steps used to estimate a component direction [blue for great circles analysis and red for PCA, black and white dots represents the steps not used to estimate any component direction and pink dots the calculated mean direction]. Similar [dark and light] colors represents the same component).

All directional data were acquired in a cryogenic SQUID magnetometer (2G-Enterprises^{TM}) and the heating procedure was performed in a TD-48SC Thermal Demagnetizer (ASC Scientific^{TM}). The heating steps were 50, 100, 150, 200, 250, 300, 320, 340, 360, 380, 400, 420, 440, 460, 480, 500, 520, 540, 560, 580, 560, 600, 620, 640, 660 and 680 °C. Only sites SM01 and SM06 of mafic dyke samples were utilized in the thermal demagnetization because it were the only ones that provided reliable results in the previous analyses. Individual specimens results are shown in Figure 4.14, demonstrating the type of demagnetization characteristics found in each sample (the decrease of magnetization intensity values in the LTD steps by almost half NRM implies that the samples have a significant amount of MD particles).

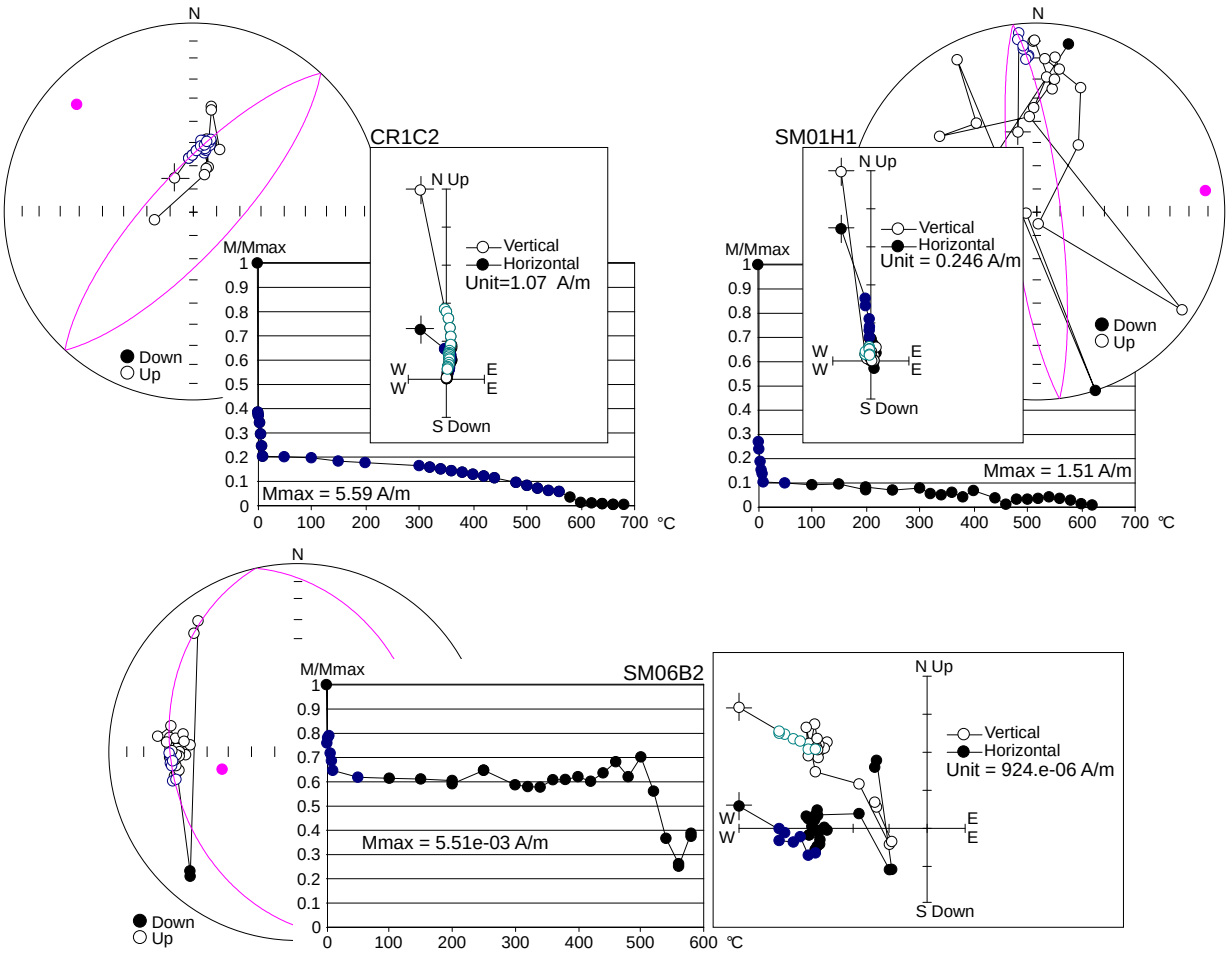

Figure 4.14: Individual samples thermal demagnetization characteristics (blue dots represents the steps used to estimate a component direction with great circles analysis, black and white dots represents the steps not used to estimate any component direction and pink dots the calculated mean direction. Similar (dark and light) colors represents the same component).

The mafic dykes samples did not provide coherent results at site level. Therefore to

calculate the sites mean directions, only rhyolite samples were taken in consideration. It is important to point out that to calculate the sites mean directions, only the reliable specimens demagnetization steps were taken in consideration (both pre-thermal and heating treatment). Both vectorial and great circle analyses were applied for all sites, and results were then combined using the method of McFadden and McElhinny (1988). In great circle analyses the range of AF and temperature steps were wide enough to incorporate low and high coercivities/unblocking temperatures. The vectors considered in the site means comprise only the high coercivity and high unblocking temperatures. The final results are shown in Figure 4.15 and the samples mean direction obtained are displayed in Appendix D. Mean directions obtained from each site are also displayed Figure 4.15 (*CR Means*) and Table 4.8 alongside with VGP location.

Table 4.8 - Thermal + AF demagnetization directional data

				Site mean direction				VGPs			
Site	Long (°W)	Lat (°S)	n/N	Dec (°)	Inc (°)	α_{95} (°)	K	Plong (°E)	Plat (°N)	*dp*	*dm*
CR01	40.90600	13.66968	11/15	36.10	11.80	15.80	9.00	22.70	49.14	8.16	16.05
CR02	40.90644	13.66975	6/10	29.40	6.90	14.30	25.00	20.76	56.17	7.23	14.38
CR03	40.90591	13.66989	8/8	64.10	-5.10	13.40	19.00	45.29	25.76	6.74	13.44
CR04	40.90515	13.66791	8/14	61.50	-23.30	12.20	23.00	55.36	30.20	6.91	12.99
CR05	40.90546	13.66500	5/5	33.80	-26.40	31.60	8.00	53.71	57.20	18.55	34.24
CR06	40.90493	13.66594	5/10	32.60	39.70	26.20	11.00	0.90	41.72	18.88	31.45
CR07	40.90416	13.66591	5/9	24.40	25.90	16.30	29.00	1.58	53.53	9.51	17.61
Mean	**40.90544**	**13.66773**		**40.52**	**4.32**	**22.67**	**8.04**	**30.68**	**46.82**	**11.38**	**22.72**

(Lat = Latitude; Long = Longitude; n/N = Number of samples used to calculated the mean direction/Number of samples analyzed; Dec = Declination; Inc = Inclination; α_{95} = Radius of the 95% confidence cone; K = Precision parameter; VGP = Virtual Geomagnetic Pole; Plong = Paleolongitude; Plat = Paleolatitude; *dp* = semi-axis parallel to the latitude; *dm* = semi-axis parallel to the longitude).

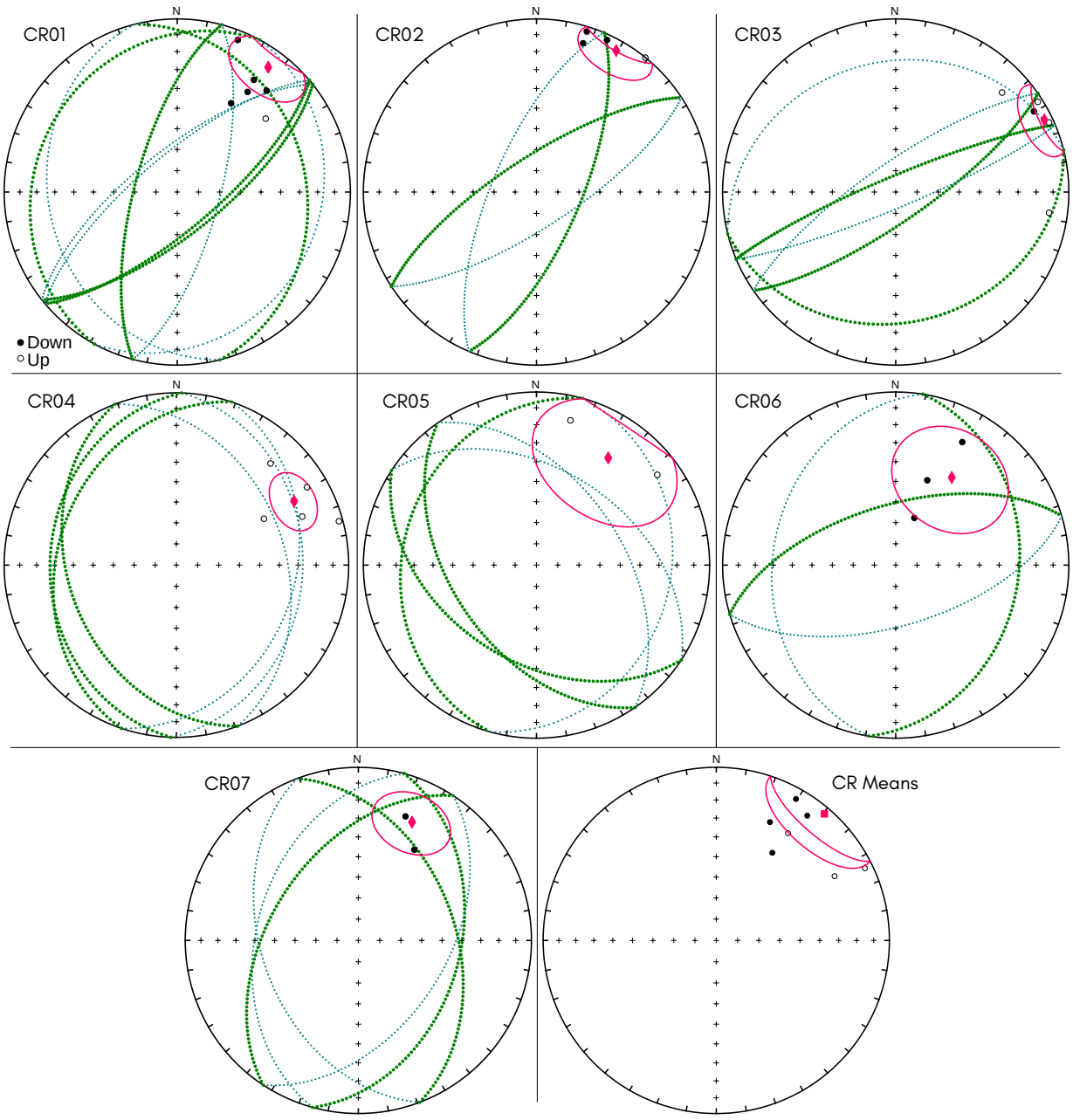

Figure 4.15: Sites mean directions acquired from both thermal and AF demagnetization procedures. *CR Means* represents the mean directions obtained from each site.

Chapter 5

Discussion

5.1 *Magnetic mineralogy*

Magnetite is the main magnetic carrier of the rhyolite samples, characterized through thermomagnetic curves and obtained coercivity values by IRM analyses (Figure 4.1a, 4.2a, 4.7a and Table 4.2, 4.5). The uncorrected hysteresis loops behavior, low values of K_m and noisy data quality in the FORC diagrams evidenced a large amount of paramagnetic particles in the samples (Figure 4.4a, 4.7a, 4.10, 4.3). Despite this scarcity of ferromagnetic particles, the FORC diagrams associated with the corrected hysteresis loops behavior and parameters analysis also indicates the presence of multi-domain particles (Figure 4.3, 4.4c, 4.5, 4.6).

Most mafic dykes thermomagnetic curves presented reversible behavior with a well pronounced Vervey transition and a "tail"feature at high temperatures (Dunlop and Özdemir, 1997), suggesting that the main magnetic carrier is magnetite, but some high T_c mineral is also present in a few samples, most likely been hematite (Figure 4.1b, 4.2b and Table 4.1). The coercivity values obtained in the IRM analyses confirms the presence of both minerals (Figure 4.7a and Table 4.4). Hysteresis loops exhibits a dominantly superparamagnetic pattern in most of the samples (Figure 4.4d), however the hysteresis parameters analysis demonstrated that the mafic dykes do not have a preferred behavior, it is composed of a mixture of SP + SD + PSD + MD particles (Figure 4.5, 4.6).

5.2 *Magnetic fabric*

The AMS directional data (Figure 4.8) obtained from the mafic dykes was of poor quality, only SM01 and SM06 provided reliable results (associated error $\leq 15°$). However it is

also possible to noticed some preferred NE-SE lineation direction for the sites SM02, SM03 and SM05 (SM08 exhibit a NW lineation trend). The observed trends are in agreement with those reported for the dyke swarms in the São Francisco Craton (Girardi et al., 2017), which exhibit a NW or NE preferred trend.

All rhyolite sites provided similar results both in anisotropy and susceptibility parameters with an Eastward high inclination lineation dipping pattern, except CR04 which provided a NE sub-horizontal pattern, most likely because its location near the border of the outcrop region (Figure 5.1). The low values of mean magnetic susceptibility and P parameter associated with a preferred oblate ellipsoid shape is an usual feature in silicic flows (Haag et al., 2020, and references there in).

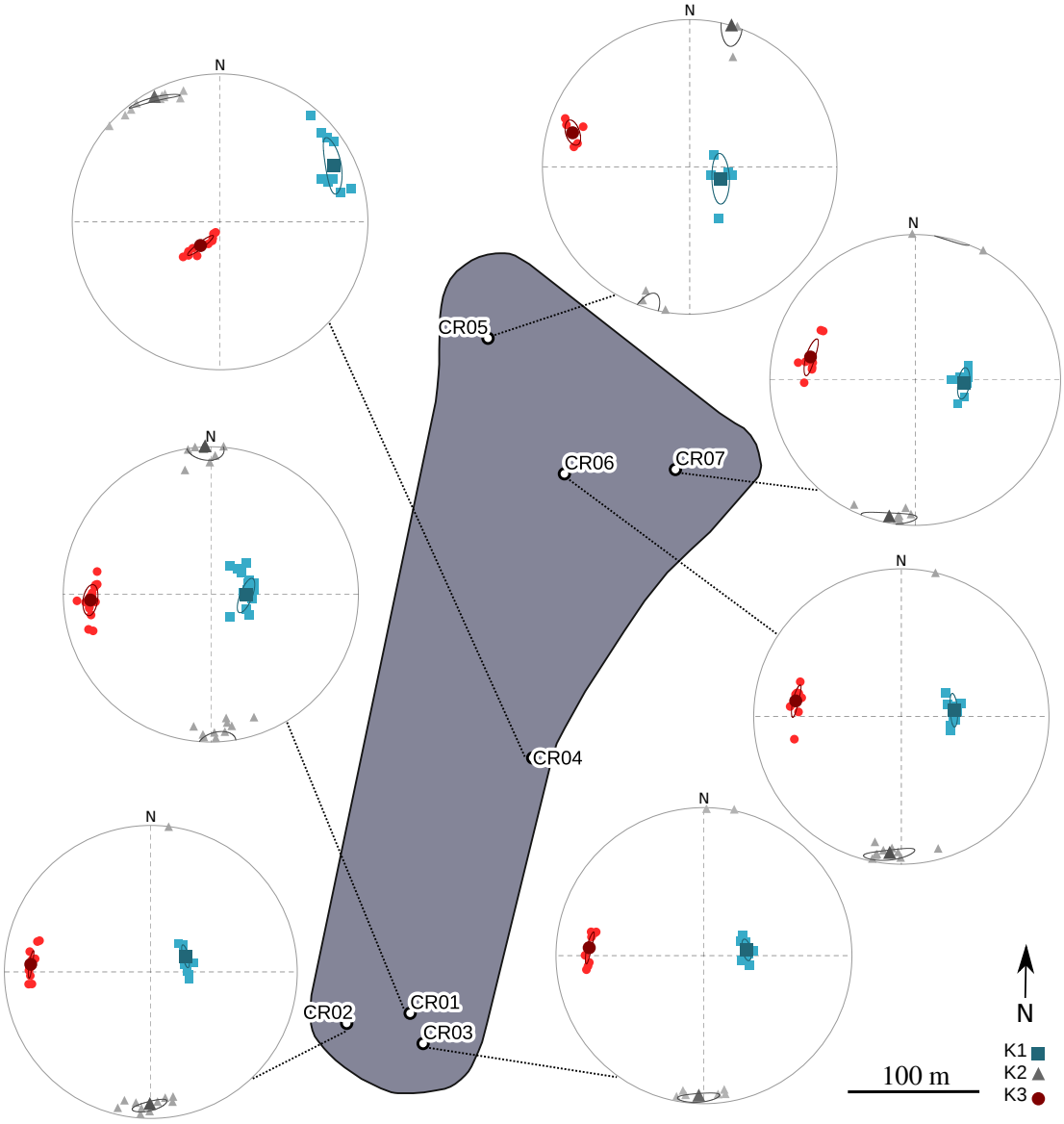

Figure 5.1: Map showing the AMS results for each site from the rhyolite.

The similarity in the AMS results indicates that the body presented a coherent lava flow direction during its formation. This is the first time that an AMS characterization is performed in a Precambrian magmatic body of that portion of the São Francisco Craton. It suggests that others magmatic bodies of the region with similar age could present the same feature and new AMS studies should be carried out.

5.3 *Paleomagnetic direction*

Rhyolite samples were subjected to detailed demagnetization procedures. Despite the effort, the rock samples only provided a secondary magnetization direction ($D_m = 40.52°$, $I_m = 4.32°$, $\alpha_{95} = 22.67°$, $K = 8.04$). In the next sections will be discussed a selected group of paleomagnetic poles available in the literature.

The mafic dykes didn't provide any paleomagnetic direction in both thermal and AF demagnetization procedures. Therefore, from this point forward, only the rhyolite results will be discussed. These rocks provided a coherent magnetic component for the rhyolite sites (Table 4.8). No field test was possible in these rhyolites due to the poor outcropping conditions. Therefore, the interpretation of the significance of this characteristic direction is difficult. The fact that the characteristic component obtained from vector analyses and great circles is very different form the present-day field or the dipolar field for the site locations, and is also different from expected Cretaceous components (Ernesto, 2006), suggest this component represents an old record of the geomagnetic field. The position of the corresponding pole in relation to other results obtained for the same region provide some hints on their significance. The mean direction obtained in the rhyolites is similar to the finds of D'Agrella-Filho et al. (2011) in the study of a collection of samples from the Jequié Block when considering the antipodal direction ($D_m = 212.6°$; $I_m = 4.1°$; $\alpha_{95} = 9.9°$; k = 38.2). Evans et al. (2016), Salminen et al. (2016) and D'Agrella-Filho et al. (2020) also reported secondary S/SW component with low inclinations, the first two relate it with the Brasiliano orogeny (late Neoproterozoic).

5.4 *São Francisco Craton paleomagnetic poles*

There are very few well constrained Precambrian paleomagnetic poles for the São Francisco Craton in the literature (D'Agrella-Filho and Pacca, 1998; D'Agrella-Filho et al.,

1990, 2004, 2011, 2020; Evans et al., 2016; Salminen et al., 2016, 2019; Trindade et al., 2004). By comparing the VGP obtained from the rhyolite samples (Table 5.1) and the Apparent Polar Wander Path (APWP) generated by those selected Precambrian CSF paleomagnetic poles (Figure 5.2), it is possible to estimate the age of the remagnetization process that the rhyolites were subjected.

Table 5.1 - Selected paleomagnetic poles from São Francisco Craton

Rock unit	Code	Age (Ma)	B/N	Plat (°N)	Plon (°E)	A_{95} (°)	K	$Q_{(7)}$	Ref.
Uauá	Ua	2623.8 ± 7.0	25/89	25.2	330.5	7.4	16.4	5	Salminen et al. (2019)
Jequié Charnockites	JQ	2035 ± 4	12/100	-0.5	342.1	9.6	21.6	4	D'Agrella-Filho et al. (2011)
Pará de Minas*	PM	1798 ± 4	10/36	39.8	16.8	17.0	9.0	4	D'Agrella-Filho et al. (2020)
Curaça	Cu	1506.7 ± 6.9	7/51	10.1	9.6	15.8	15.6	5	Salminen et al. (2016)
Bahia costal dykes*	Bcd	923.2± 2.6	46/267	7.3	106.4	6.2	12.5	6	Evans et al. (2016)
Jequié other Comps*	JoC	———	—	55.7	32.9	9.0	46.3	—	D'Agrella-Filho et al. (2011)
Rhyolites	Ry	———	7/48	46.82	30.68	—	—	3	This work

(B/N = Number of sites/Number of samples; Plat = Paleolatitude; Plon = Paleolongitude; $Q_{(7)}$ = Van der Voo (1990) seven quality criteria; * indicates that the antipole has been taken into consideration)

The Uauá basic dyke swarm was early analyzed by D'Agrella-Filho and Pacca (1998). At that time, the authors classified the calculated magnetization direction as secondary mostly due to the lack of any field tests. More recently, Salminen et al. (2019) revisited the region and performed a new paleomagnetic study in which the authors were able to perform a positive baked contact test, ensuring the primary nature of the magnetization. Therefore, the Uauá pole is the oldest Precambrian paleomagnetic pole of the São Francisco Craton, with both geochronological and paleomagnetic information well established.

The Jequié Charnockites represents high grade metamorphic rocks of the eastern border of the block (D'Agrella-Filho et al., 2011). The authors were able to characterized two magnetization components in the studied samples. One corresponding to the JQ pole and another (JoC) that was only present in the samples retrieved from the inner areas of the Jequié Block and the Salvador-Itabuna-Curaça Belt. This second direction yielded a paleomagnetic pole located at 55.7°S, 212.9°E (A_{95}=9.0°; K=46.3), which is very similar to the Rhyolite VGP (Table 4.8). No interpretation was provided regarding JoC, the authors were only able to relate it with the formation of the Salvador-Itabuna-Curaça Belt because of its magnetic fabric, structural features and sampling location.

The Pará de Minas is the most recent pole (among the selected ones) published in the literature (D'Agrella-Filho et al., 2020). It essentially consists of diabase to gabbro mafic

dykes located at the southernmost part of the SFC at Minas Gerais state. One of the most important features of the work is the new insights regarding the reconstruction of the supercontinent Columbia (Meert and Santosh, 2017, and references there in), in which the authors suggests a new paleogeographic connection between the São Francisco/Congo, Rio de la Plata, North China and India Cratons.

The Curaça pole represents the inner sector of the SFC at the Chapada Diamantina and also provides a different approach for the paleogeographic reconstruction of the Nuna/Columbia supercontinent at 1.5 Ga (Salminen et al., 2016). The key aspect of the proposal is the relation between SW Congo and S-SE Baltica in two possible configuration, one with SF/C close to Baltica and another with a gap between them.

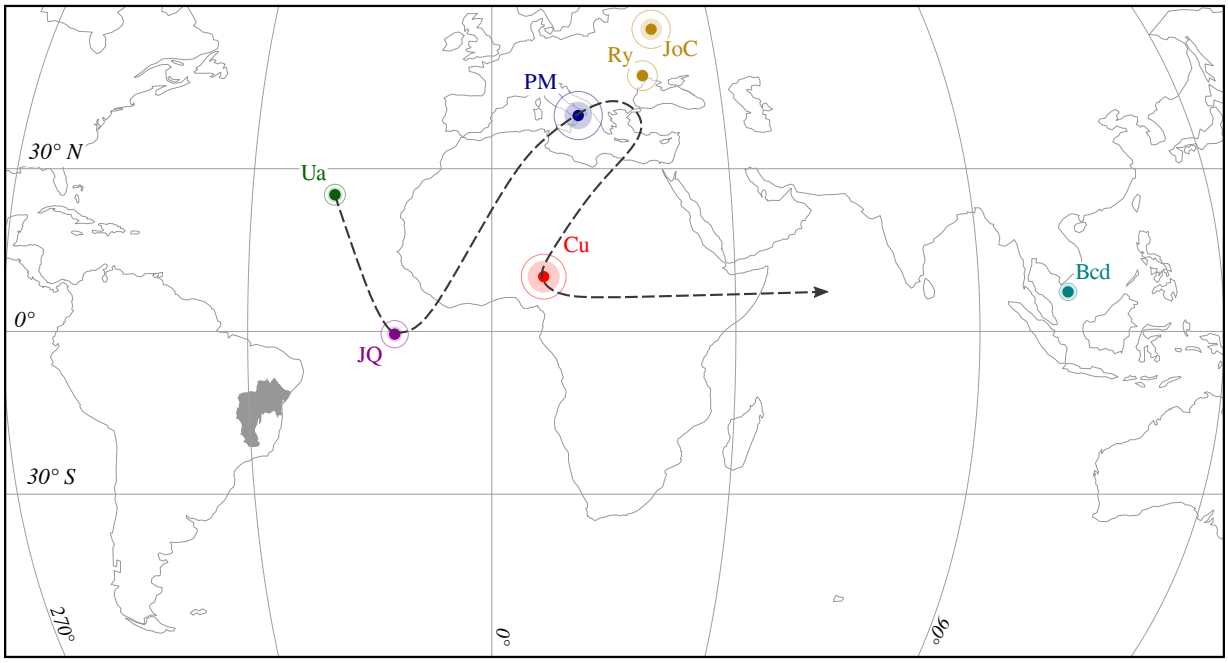

Figure 5.2: Selected SFC paleomagnetic poles in present day map coordinates (SFC highlighted in gray; Poles codes in agreement with Table 5.1; The size of the pole marker represents the A_{95} value and the shaded area inside the Q_7 value; Dashed line assists the identification of the age relations of each pole, does not represent the apparent polar wander path of the SFC).

The paleomagnetic information regarding the Ilhéus, Itaju do Colônia and Olivença mafic dykes that outcrops in the Bahia beach coast has been intensively studied over the past decades (D'Agrella-Filho et al., 1990, 2004; Evans et al., 2016). The most recent work by Evans et al. (2016) review all of the paleomagnetic data available for the region, adds new data and constrains the geochronological information of the studied area. The authors correlated the mafic dykes occurrence with a possible large igneous province proposed by

Ernst and Buchan (1997) and demonstrated that there were several possible locations that the SF/C Craton could be located at the period of the Rodinia supercontinent (Meert and Torsvik, 2003; Evans, 2009).

Chapter 6

Conclusions

The main conclusions of this study is summarized below:

- Magnetite is the main magnetic carrier in both mafic dykes and rhyolite samples.
- The magnetic mineralogy characterization indicates that the samples are mainly composed of a mixture PSD + MD grains, but also present a high amount of paramagnetic particles.
- The mafic dykes didn't provided satisfactory results in both magnetic fabric and paleomagnetic direction characterization.
- The rhyolite magnetic fabric indicates low values of magnetic susceptibility and anisotropy degree (P). It was possible to identify that the outcrop region posses a coherent eastward sub-vertical lava flow direction.
- The paleomagnetic characterization of the rhyolites samples provided a magnetization component ($D_m = 40.52°$, $I_m = 4.32°$, $\alpha_{95} = 22.67°$, $K = 8.04$), yielding a VGP at 46.82°N, 30.68°E ($dp = 11.38$, $dm = 22.72$), which is similar to other paleomagnetic poles obtained for the same region. Following previous interpretations for these components, and given the lack of field tests for the rhyolites studied here, suggests that this component is old, but secondary.

Bibliography

Agico Inc., 2017 REMA6W - Control software for JR-6/JR-6A spinner magnetometers (Version 6.2.4). Brno, Czech Republic, https://www.agico.com

Alkmim F. F., O que faz de um cráton um cráton? O Cráton do São Francisco e as revelações almeidianas ao delimitá-lo, In: *Geologia do continente Sul-Americano: evolução da obra de Fernando Flávio Marques de Almeida*, 2004, pp 17–34

Alkmim F. F., Teixeira W., The paleoproterozoic mineiro belt and the quadrilátero ferrífero, In: *São Francisco Craton, Eastern Brazil. Regional Geology Reviews. Springer, Cham*, 2017, pp 71–94

Almeida F. F. M., O Cráton do São Francisco, *Revista Brasileira de Geociências*, 1977, vol. 7, p. 349

Anaconda Team, 2016 *Anaconda Software Distribution.* Computer software. Vers. 2-2.4.0.. Web. https://anaconda.com

As J. A., AC demagnetization of rocks: analysis of results, In: *Methods in Palaeomagnetism. Developments in Solid Earth Geophysics*, 2013, vol. 3, p. 221

Barbosa J. S. F., Barbosa R. G., The paleoproterozoic eastern bahia orogenic domain, In: *São Francisco Craton, Eastern Brazil. Regional Geology Reviews. Springer, Cham*, 2017, pp 57–69

Barbosa J. S. F., Cruz S. C. P., Souza J. S., Terrenos metamórficos do embasamento, In: *Geologia da Bahia: pesquisa e atualização*, CBPM, 2012, vol. 1, p. 101

Barbosa J. S. F., Sabaté P., Geological features and the Paleoproterozoic collision of four Archean crustal segments of the São Francisco Craton, Bahia, Brazil: a synthesis, *Anais da Academia Brasileira de Ciências*, 2002, vol. 74, p. 343

Barbosa J. S. F., Sabaté P., Archean and Paleoproterozoic crust of the São Francisco craton, Bahia, Brazil: geodynamic features, *Precambrian Research*, 2004, vol. 133, p. 1

Barbosa J. S. F., Sabaté P., Marinho M. M., O Cráton do São Francisco na Bahia: uma síntese, *Revista Brasileira de Geociências*, 2003, vol. 33, p. 3

Bingham C., An antipodally symmetric distribution on the sphere, *The Annals of Statistics*, 1974, vol. 2, p. 1201

Bleeker W., The late Archean record: a puzzle in ca. 35 pieces, *Lithos*, 2003, vol. 71, p. 99

Bleeker W., Ernst R., Short-lived mantle generated magmatic events and their dyke swarms: the key unlocking Earth's paleogeographic record back to 2.6 Ga, *Dyke swarms—time markers of crustal evolution*, 2006, pp 3–26

Borradaile G., Anisotropy of magnetic susceptibility: rock composition versus strain, *Tectonophysics*, 1987, vol. 138, p. 327

Borradaile G. J., Low-temperature demagnetization and ice-pressure demagnetization in magnetite and haematite, *Geophysical Journal International*, 1994, vol. 116, p. 571

Brenner A. R., Fu R. R., Evans D. A. D., Smirnov A. V., Trubko R., Rose I. R., Paleomagnetic evidence for modern-like plate motion velocities at 3.2 Ga, *Science Advances*, 2020, vol. 6, p. eaaz8670

Buddington A. F., Lindsley D. H., Iron-titanium oxide minerals and synthetic equivalents, *Journal of petrology*, 1964, vol. 5, p. 310

Butler R. F., Paleomagnetism: Magnetic Domains to Geologic Terranes, Boston, MA: Blackwell Scientific, 1992

Cañón-Tapia E., Anisotropy of magnetic susceptibility of lava flows and dykes: a historical account, *Geological Society, London, Special Publications*, 2004, vol. 238, p. 205

Chadima M., Hrouda F., Remasoft 3.0 a user-friendly paleomagnetic data browser and analyzer, *Travaux Géophysiques*, 2006, vol. **XXVII**, p. 20

Chadima M., Jelinek V., Anisoft 4.2: Anisotropy data browser for windows, Agico Inc., Brno, Czech Republic, https://www.agico.com, https://www.agico.com, 2009

Collinson D. W., Methods in rock magnetism and palaeomagnetism *techniques and instrumentation*, Springer Science & Business Media, 1983

Condie K. C., How to make a continent: thirty-five years of TTG research, In: *Evolution of Archean Crust and Early Life. Modern Approaches in Solid Earth Sciences, vol 7. Springer, Dordrecht*, 2014, pp 179–193

Cordani U. G., Kei S., Marinho M. M., The geologic evolution of the ancient granite—greenstone terrane of central-southern Bahia, Brazil, *Precambrian Research*, 1985, vol. 27, p. 187

Cordani U. G., Ramos V. A., Fraga L. M., Cegarra M., Delgado I., de Souza K. G., Gomes F. E. M., Schobbenhaus C., Tectonic Map of South America at 1:5.9 M, *CGMW-CPRM-SEGEMAR*, 2016

Creer K. M., Thermal Demagnetization by the Continuous Method, In: *Methods in Palaeomagnetism. Developments in Solid Earth Geophysics*, 2013, vol. 3, p. 287

Cunha J. C., Barbosa J. S. F., Mascarenhas J. F., Greenstone belts e sequências similares, In: *Geologia da Bahia: pesquisa e atualização, CBPM*, 2012, vol. 1, p. 203

D'Agrella-Filho M. S., Cordani U. G., The paleomagnetic record of the São Francisco-Congo Craton, In: *São Francisco Craton, Eastern Brazil*, 2017, pp 305–320

D'Agrella-Filho M. S., Pacca I. G., Paleomagnetism of Paleoproterozoic mafic dyke swarm from the Uauá region, northeastern São Francisco Craton, Brazil: tectonic implications, *Journal of South American Earth Sciences*, 1998, vol. 11, p. 23

D'Agrella-Filho M. S., Pacca I. G., Renne P. R., Onstott T. C., Teixeira W., Paleomagnetism of Middle Proterozoic (1.01 to 1.08 Ga) mafic dykes in southeastern Bahia State-São Francisco craton, Brazil, *Earth and Planetary Science Letters*, 1990, vol. 101, p. 332

D'Agrella-Filho M. S., Pacca I. I. G., Trindade R. I. F., Teixeira W., Raposo M. I. B., Onstott T. C., Paleomagnetism and 40Ar/39Ar ages of mafic dikes from Salvador (Brazil): new constraints on the São Francisco craton APW path between 1080 and 1010 Ma, *Precambrian Research*, 2004, vol. 132, p. 55

D'Agrella-Filho M. S., Teixeira W., da Trindade R. I. F., Patroni O. A. L., Prieto R. F., Paleomagnetism of 1.79 Ga Pará de Minas mafic dykes: Testing a São Francisco/Congo-North China-Rio de la Plata connection in Columbia, *Precambrian Research*, 2020, vol. 338, p. 105584

D'Agrella-Filho M. S., Trindade R. I. F., Tohver E., Janikian L., Teixeira W., Hall C., Paleomagnetism and 40Ar/39Ar geochronology of the high-grade metamorphic rocks of the Jequié block, São Francisco Craton: Atlantica, Ur and beyond, *Precambrian Research*, 2011, vol. 185, p. 183

Day R., Fuller M., Schmidt V. A., Hysteresis properties of titanomagnetites: grain-size and compositional dependence, *Physics of the Earth and planetary interiors*, 1977, vol. 13, p. 260

de Kock M. O., Evans D. A. D., Beukes N. J., Validating the existence of Vaalbara in the Neoarchean, *Precambrian Research*, 2009, vol. 174, p. 145

Dunlop D. J., Magnetic Mineralogy of Unheated and Heated Red Sediments by Coercivity Spectrum Analysis*, *Geophysical Journal International*, 1972, vol. 27, p. 37

Dunlop D. J., On the use of Zijderveld vector diagrams in multicomponent paleomagnetic studies, *Physics of the Earth and Planetary Interiors*, 1979, vol. 20, p. 12

Dunlop D. J., Theory and application of the Day plot (Mrs/Ms versus Hcr/Hc) 1. Theoretical curves and tests using titanomagnetite data, *Journal of Geophysical Research: Solid Earth*, 2002a, vol. 107, p. EPM

Dunlop D. J., Theory and application of the Day plot (Mrs/Ms versus Hcr/Hc) 2. Application to data for rocks, sediments, and soils, *Journal of Geophysical Research: Solid Earth*, 2002b, vol. 107, p. EPM

Dunlop D. J., Özdemir Ö., Rock Magnetism: fundamentals and frontiers. Cambridge university press, 1997

Dunlop D. J., Özdemir Ö., Magnetizations in Rocks and Minerals, In: *Treatise on Geophysics (Second Edition)*, 2015, vol. 5, p. 255

Ernesto M., Drift of South American platform since early Cretaceous: reviewing the apparent polar wander path, *Geociências*, 2006, vol. 25, p. 83

Ernst R. E., Buchan K. L., Giant Radiating Dyke Swarms: Their Use in Identifying Pre-Mesozoic Large Igneous Provinces and Mantle Plumes, In: *Large Igneous Provinces: Continental, Oceanic, and Planetary Flood Volcanism*, 1997, vol. 100, p. 297

Evans D. A. D., The palaeomagnetically viable, long-lived and all-inclusive Rodinia supercontinent reconstruction, *Geological Society, London, Special Publications*, 2009, vol. 327, p. 371

Evans D. A. D., Pisarevsky S. A., Plate tectonics on early Earth? Weighing the paleomagnetic evidence, In: *When did plate tectonics begin on planet Earth*, 2008, vol. 440, p. 249

Evans D. A. D., Smirnov A. V., Gumsley A. P., Paleomagnetism and U—Pb geochronology of the black range dykes, Pilbara Craton, Western Australia: A neoarchean crossing of the polar circle, *Australian Journal of Earth Sciences*, 2017, vol. 64, p. 225

Evans D. A. D., Trindade R. I. F., Catelani E. L., D'Agrella-Filho M. S., Heaman L. M., Oliveira E. P., Söderlund U., Ernst R. E., Smirnov A. V., Salminen J. M., Return to Rodinia? Moderate to high palaeolatitude of the São Francisco/Congo craton at 920 Ma, *Geological Society, London, Special Publications*, 2016, vol. 424, p. 167

Fisher R. A., Dispersion on a sphere, *Proceedings of the Royal Society of London. Series A. Mathematical and Physical Sciences*, 1953, vol. 217, p. 295

Girardi V. A. V., Teixeira W., Mazzucchelli M., Oliveira E. P., Costa P. C. C., Mafic dykes: Petrogenesis and tectonic inferences, In: *São Francisco Craton, Eastern Brazil. Regional Geology Reviews. Springer, Cham*, 2017, pp 145–169

Griffiths D. J., Introduction To Electrodynamics 3 edn. Prentics Hall Upper Saddle River, NJ, 1999

Grommé C. S., Wright T. L., Peck D. L., Magnetic properties and oxidation of iron-titanium oxide minerals in Alae and Makaopuhi lava lakes, Hawaii, *Journal of Geophysical Research*, 1969, vol. 74, p. 5277

Haag M. B., de Freitas R. B., Sommer C. A., Savian J. F., Lima E. F., Gambeta J. H., da Silveira Lyra D., da Trindade R. I. F., Multi-proxy case study of a Neoproterozoic rhyolite flow in southernmost Brazil: Emplacement mechanisms and implications for ancient felsic lavas, *Journal of South American Earth Sciences*, 2020, p. 102982

Halls H., The use of converging remagnetization circles in palaeomagnetism, *Physics of the Earth and Planetary Interiors*, 1978, vol. 16, p. 1

Halls H. C., A least-squares method to find a remanence direction from converging remagnetization circles, *Geophysical Journal International*, 1976, vol. 45, p. 297

Hasui Y., Carneiro C. D. R., Almeida F. F. M., Bartorelli A., Geologia do Brasil. Beca São Paulo, 2012

Hawkesworth C. J., Cawood P. A., Dhuime B., Tectonics and crustal evolution, *GSA today*, 2016, vol. 26, p. 4

Hawkesworth C. J., Dhuime B., Pietranik A. B., Cawood P. A., Kemp A. I. S., Storey C. D., The generation and evolution of the continental crust, *Journal of the Geological Society*, 2010, vol. 167, p. 229

Heilbron M., Cordani U. G., Alkmim F. F., The São Francisco craton and its margins, In: *São Francisco Craton, Eastern Brazil. Regional Geology Reviews. Springer, Cham*, 2017, pp 3–13

Herrero-Bervera E., Krasa D., Van Kranendonk M. J., A whole rock absolute paleointensity determination of dacites from the Duffer Formation (ca. 3.467 Ga) of the Pilbara Craton, Australia: An impossible task?, *Physics of the Earth and Planetary Interiors*, 2016, vol. 258, p. 51

Hoffman K. A., Day R., Separation of multi-component NRM: a general method, *Earth and Planetary Science Letters*, 1978, vol. 40, p. 433

Hrouda F., Magnetic anisotropy of rocks and its application in geology and geophysics, *Geophysical Surveys*, 1982, vol. 5, p. 37

Hrouda F., A technique for the measurement of thermal changes of magnetic susceptibility of weakly magnetic rocks by the CS-2 apparatus and KLY-2 Kappabridge, *Geophysical Journal International*, 1994, vol. 118, p. 604

Jackson M., Anisotropy of magnetic remanence: a brief review of mineralogical sources, physical origins, and geological applications, and comparison with susceptibility anisotropy, *Pure and Applied Geophysics*, 1991, vol. 136, p. 1

Jelínek V., The statistical theory of measuring anisotropy of magnetic susceptibility of rocks and its application. Geofyzika Brno, Czech Republic, 1977

Jelínek V., Kropáček V., Statistical processing of anisotropy of magnetic susceptibility measured on groups of specimens, *Studia geophysica et geodaetica*, 1978, vol. 22, p. 50

Kent J. T., The Fisher-Bingham distribution on the sphere, *Journal of the Royal Statistical Society: Series B (Methodological)*, 1982, vol. 44, p. 71

Kirschvink J. L., The least-squares line and plane and the analysis of palaeomagnetic data, *Geophysical Journal International*, 1980, vol. 62, p. 699

Kröner A., Layer P. W., Crust formation and plate motion in the early Archean, *Science*, 1992, vol. 256, p. 1405

Kruiver P. P., Dekkers M. J., Heslop D., Quantification of magnetic coercivity components by the analysis of acquisition curves of isothermal remanent magnetisation, *Earth and Planetary Science Letters*, 2001, vol. 189, p. 269

Lascu I., Einsle J. F., Ball M. R., Harrison R. J., The vortex state in geologic materials: A micromagnetic perspective, *Journal of Geophysical Research: Solid Earth*, 2018, vol. 123, p. 7285

Leite C. M. M., Marinho M. M., Serra de Jacobina e Contendas-Mirante, In: *Geologia da Bahia Pesquisa e Atualização. Salvador: CBPM-Companhia Baiana de Pesquisa Mineral*, 2012, vol. 1, p. 397

Lowrie W., Identification of ferromagnetic minerals in a rock by coercivity and unblocking temperature properties, *Geophysical Research Letters*, 1990, vol. 17, p. 159

Lowrie W., Fichtner A., Fundamentals of Geophysics. Cambridge university press, 2007

Macêdo E. P., Carta geológica Preliminar: Folha Vitória da Conquista SD.24-Y-A-VI, CPRM, 2016

McElhinny M. W., Senanayake W. E., Paleomagnetic evidence for the existence of the geomagnetic field 3.5 Ga ago, *Journal of Geophysical Research: Solid Earth*, 1980, vol. 85, p. 3523

McFadden P. L., The best estimate of Fisher's precision parameter κ, *Geophysical Journal International*, 1980, vol. 60, p. 397

McFadden P. L., McElhinny M. W., The combined analysis of remagnetization circles and direct observations in palaeomagnetism, *Earth and Planetary Science Letters*, 1988, vol. 87, p. 161

Marchesin W. F., Geologia, geoquímica e geocronologia do domo da Serra dos Meiras, Bloco Gavião, Bahia, UNICAMP, 2015, Master Dissertation

Marinho M. M., Costa P. H., Silva E. F. A., Torquato J. R. F., A seqüência vulcanos-sedimentar Contendas-Mirante, uma estrutura do tipo *Greenstone Belt*?, *Companhia Baiana de Pesquisa Mineral (CBPM), Série Arquivos Abertos*, 2009, vol. 32, p. 68

Marinho M. M., Galvão C. F., Nonato I. F., Brito R. S. C., Geologia e potencialidade mineral da borda nordeste da Faixa Contendas-Mirante e do *Sill* do Rio Jacaré, Bahia, *Companhia Baiana de Pesquisa Mineral (CBPM), Série Arquivos Abertos*, 1994, vol. 6, p. 17

Marinho M. M., Sabaté P., Barbosa J. S. F., The Contendas-Mirante volcano-sedimentary belt, In: *Petrologic and Geochronologic Evolution of the oldest segments of the São Francisco Craton, Brazil. Bol. IG-USP: Pub. Especial*, 1993, vol. 17, p. 37

Martin H., Peucat J. J., Sabaté P., Cunha J. C., Crustal evolution in the early Archaean of South America: example of the Sete Voltas Massif, Bahia State, Brazil, *Precambrian Research*, 1997, vol. 82, p. 35

Martin H., Sabaté P., Peucat J. J., Cunha J. C., Un segment de croute continentale d age Archéean ancien (3.4 milliards données): le Massif de Sete Voltas (Bahia-Brésil), *CR Acad. Sci. Paris*, 1991, vol. 313, p. 531

Martins A. A. M., Lopes C. G., Pires A. S., Projeto Contendas-Macajuba: Mirante, Folha SD.24-Y-A-III. Carta Geológica Preliminar. Salvador: CPRM. 1 mapa colorido. Escala 1:100.000. Programa Gestão Estratégica da Geologia, da Mineração e da Transformação Mineral, 2017a

Martins A. A. M., Lopes C. G., Pires A. S., Projeto Contendas-Macajuba: Olho D'agua do Cruzeiro, Folha SD.24-V-C-VI. Carta Geológica Preliminar. Salvador: CPRM. 1 mapa colorido. Escala 1:100.000. Programa Gestão Estratégica da Geologia, da Mineração e da Transformação Mineral, 2017b

Mascarenhas J. F., Ledru P., Souza S. L., Conceição Filho V. M., Melo L. F. A., Lorenzo C. L., Milési J. P., Geologia e recursos minerais do Grupo Jacobina e da parte sul do Greenstone Belt de Mundo Novo, *Companhia Baiana de Pesquisa Mineral (CBPM), Série Arquivos Abertos*, 1998, vol. 13, p. 55

Mascarenhas J. F., Silva E. F. A., Greenstone Belt de Mundo Novo: caracterização e implicações metalogenéticas e geotectônicas no Cráton do São Francisco, *Companhia Baiana de Pesquisa Mineral (CBPM), Série Arquivos Abertos*, 1994, vol. 5, p. 31

Maxbauer D. P., Feinberg J. M., Fox D. L., MAX UnMix: A web application for unmixing magnetic coercivity distributions, *Computers & Geosciences*, 2016, vol. 95, p. 140

Meert J. G., Pivarunas A. F., Evans D. A. D., Pisarevsky S. A., Pesonen L. J., Li Z.-X., Elming S.-Å., Miller S. R., Zhang S., Salminen J. M., The magnificent seven: A proposal for modest revision of the Van der Voo (1990) quality index, *Tectonophysics*, 2020, vol. 790, p. 228549

Meert J. G., Santosh M., The Columbia supercontinent revisited, *Gondwana Research*, 2017, vol. 50, p. 67

Meert J. G., Torsvik T. H., The making and unmaking of a supercontinent: Rodinia revisited, *Tectonophysics*, 2003, vol. 375, p. 261

Merrill R. T., Low-temperature treatments of magnetite and magnetite-bearing rocks, *Journal of Geophysical Research*, 1970, vol. 75, p. 3343

Mertanen S., Korhonen F., Paleomagnetic constraints on an Archean—Paleoproterozoic Superior–Karelia connection: new evidence from Archean Karelia, *Precambrian Research*, 2011, vol. 186, p. 193

Moskowitz B. M., Methods for estimating Curie temperatures of titanomaghemites from experimental Js-T data, *Earth and Planetary Science Letters*, 1981, vol. 53, p. 84

Moyen J. F., Martin H., Forty years of TTG research, *Lithos*, 2012, vol. 148, p. 312

Néel L., Some theoretical aspects of rock-magnetism, *Advances in physics*, 1955, vol. 4, p. 191

Newell D. B., Tiesinga E., The International System of Units (SI) 2019 Edition, *NIST SP 330*, 2019, https://doi.org/10.6028/NIST.SP.330-2019

Nutman A. P., Cordani U. G., SHRIMP U-Pb zircon geochronology of Archaean granitoids from the Contendas-Mirante area of the São Francisco Craton, Bahia, Brazil, *Precambrian Research*, 1993, vol. 63, p. 179

Nutman A. P., Cordani U. G., Sabaté P., SHRIMP U-Pb ages of detrital zircons from the early proterozoic Contendas-Mirante supracrustal belt, São Francisco Craton, Bahia, Brazil, *Journal of South American Earth Sciences*, 1994, vol. 7, p. 109

Oliveira E., Mcnaughton N., Zincone S., Talavera C., 3.6-3.7 Ga Gneisses of the São Francisco Craton, Brazil: South America's Oldest Rocks, in 2019 Goldschmidt Conference, Barcelona, Spain, August, 2019, pp 18–23

Parry L. G., Physical Principles of Demagnetization, In: *Methods in Palaeomagnetism. Developments in Solid Earth Geophysics*, 2013, vol. 3, p. 217

Petrovskỳ E., Kapička A., On determination of the Curie point from thermomagnetic curves, *Journal of Geophysical Research: Solid Earth*, 2006, vol. 111

Peucat J. J., Mascarenhas J. F., Barbosa J. S. F., de Souza S. L., Marinho M. M., Fanning C. M., Leite C. M. M., 3.3 Ga SHRIMP U–Pb zircon age of a felsic metavolcanic rock from the Mundo Novo greenstone belt in the São Francisco craton, Bahia (NE Brazil), *Journal of South American Earth Sciences*, 2002, vol. 15, p. 363

Pullaiah G., Irving E., Buchan K. L., Dunlop D. J., Magnetization changes caused by burial and uplift, *Earth and Planetary Science Letters*, 1975, vol. 28, p. 133

Roberts A. P., The Philosophy of FORCs: What to do, how to do it, and why..., *2015 First Order Reversal Curve (FORC) Workshop*, Retrieved from the University of Minnesota Digital Conservancy, http://hdl.handle.net/11299/173858, 2015

Roberts A. P., Heslop D., Zhao X., Pike C. R., Understanding fine magnetic particle systems through use of first-order reversal curve diagrams, *Reviews of Geophysics*, 2014, vol. 52, p. 557

Roberts A. P., Pike C. R., Verosub K. L., First-order reversal curve diagrams: A new tool for characterizing the magnetic properties of natural samples, *Journal of Geophysical Research: Solid Earth*, 2000, vol. 105, p. 28461

Rochette P., Jackson M., Aubourg C., Rock magnetism and the interpretation of anisotropy of magnetic susceptibility, *Reviews of Geophysics*, 1992, vol. 30, p. 209

Salminen J., Pesonen L. J., Lahti K., Kannus K., Lightning-induced remanent magnetization—the Vredefort impact structure, South Africa, *Geophysical Journal International*, 2013, vol. 195, p. 117

Salminen J. M., Evans D. A. D., Trindade R. I. F., Oliveira E. P., Piispa E. J., Smirnov A. V., Paleogeography of the Congo/São Francisco craton at 1.5 Ga: Expanding the core of Nuna supercontinent, *Precambrian Research*, 2016, vol. 286, p. 195

Salminen J. M., Oliveira E. P., Piispa E. J., Smirnov A. V., Trindade R. I. F., Revisiting the paleomagnetism of the Neoarchean Uauá mafic dyke swarm, Brazil: Implications for Archean supercratons, *Precambrian Research*, 2019, vol. 329, p. 108

Smirnov A. V., Evans D. A. D., Ernst R. E., Söderlund U., Li Z.-X., Trading partners: Tectonic ancestry of southern Africa and western Australia, in Archean supercratons Vaalbara and Zimgarn, *Precambrian Research*, 2013, vol. 224, p. 11

Smirnov A. V., Tarduno J. A., Thermochemical remanent magnetization in Precambrian rocks: Are we sure the geomagnetic field was weak?, *Journal of Geophysical Research: Solid Earth*, 2005, vol. 110

Smirnov A. V., Tarduno J. A., Kulakov E. V., McEnroe S. A., Bono R. K., Palaeointensity, core thermal conductivity and the unknown age of the inner core, *Geophysical Journal International*, 2016, vol. 205, p. 1190

Tarduno J. A., Cottrell R. D., Watkeys M. K., Bauch D., Geomagnetic field strength 3.2 billion years ago recorded by single silicate crystals, *Nature*, 2007, vol. 446, p. 657

Tarling D., Hrouda F., Magnetic anisotropy of rocks. Springer Science & Business Media, 1993

Tauxe L., Paleomagnetic principles and practice. vol. 17, Springer Science & Business Media, 2006

Tauxe L., Banerjee S. K., Butler R. F., Van der Voo R., Essentials of Paleomagnetism, 5th Web Edition, 2018

Tauxe L., Bertram H. N., Seberino C., Physical interpretation of hysteresis loops: Micromagnetic modeling of fine particle magnetite, *Geochemistry, Geophysics, Geosystems*, 2002, vol. 3, p. 1

Tauxe L., Shaar R., Jonestrask L., Swanson-Hysell N. L., Minnett R., Koppers A. A. P., Constable C. G., Jarboe N., Gaastra K., Fairchild L., PmagPy: Software package for paleomagnetic data analysis and a bridge to the Magnetics Information Consortium (MagIC) Database, *Geochemistry, Geophysics, Geosystems*, 2016, vol. 17, p. 2450

Teixeira W., Oliveira E. P., Marques L. S., Nature and evolution of the Archean crust of the São Francisco Craton, In: *São Francisco Craton, Eastern Brazil. Regional Geology Reviews. Springer, Cham*, 2017, pp 29–56

Teixeira W., Sabaté P., Barbosa J., Noce C. M., Carneiro M. A., Archean and Paleoproterozoic tectonic evolution of the São Francisco craton, Brazil, In: *Tectonic Evolution of South America*, 2000, pp 101–137

Trindade R. I. F., D'Agrella-Filho M. S., Babinski M., Font E., Neves B. B. B., Paleomagnetism and geochronology of the Bebedouro cap carbonate: evidence for continental-scale Cambrian remagnetization in the São Francisco craton, Brazil, *Precambrian Research*, 2004, vol. 128, p. 83

Turner G. M., Rasson J., Reeves C., Observation and Measurement Techniques, In: *Treatise on Geophysics (Second Edition)*, 2015, vol. 5, p. 91

Van der Voo R., The reliability of paleomagnetic data, In: *Reliability of paleomagnetic data. Tectonophysics*, 1990, vol. 184, p. 1

Zijderveld J. D. A., AC demagnetization of rocks: analysis of results, In: *Methods in Palaeomagnetism. Developments in Solid Earth Geophysics*, 2013, vol. 3, p. 254

Zincone S. A., Oliveira E. P., Laurent O., Zhang H., Zhai M., 3.30 Ga high-silica intraplate volcanic-plutonic system of the Gavião Block, São Francisco Craton, Brazil: Evidence of an intracontinental rift following the creation of insulating continental crust, *Lithos*, 2016, vol. 266, p. 414

Appendix

Appendix A

Thermomagnetic Curves

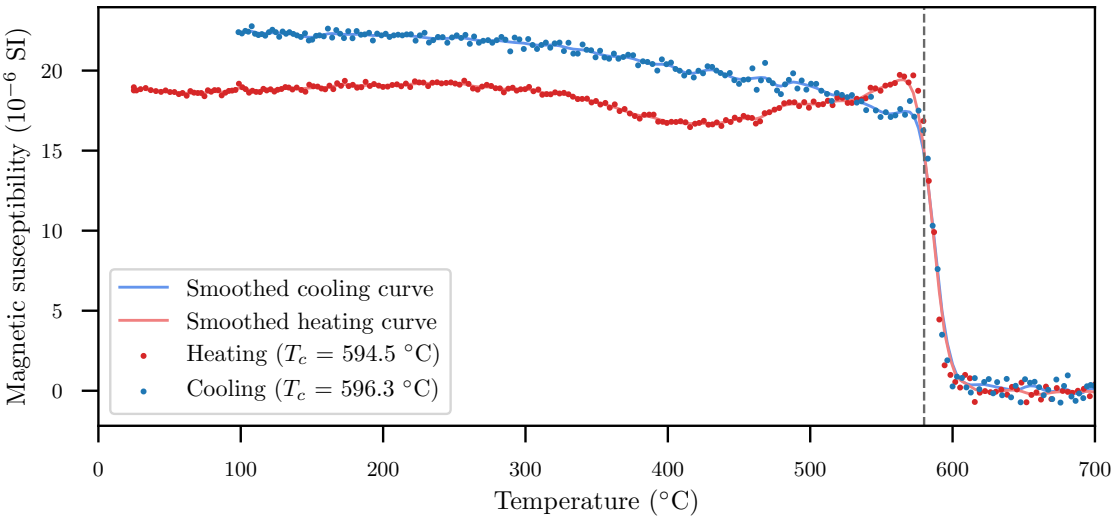

Figure A.1: High temperature thermomagnetic curve of representative sample from site CR01 (dashed line indicates the T_C of magnetite [580 °C]).

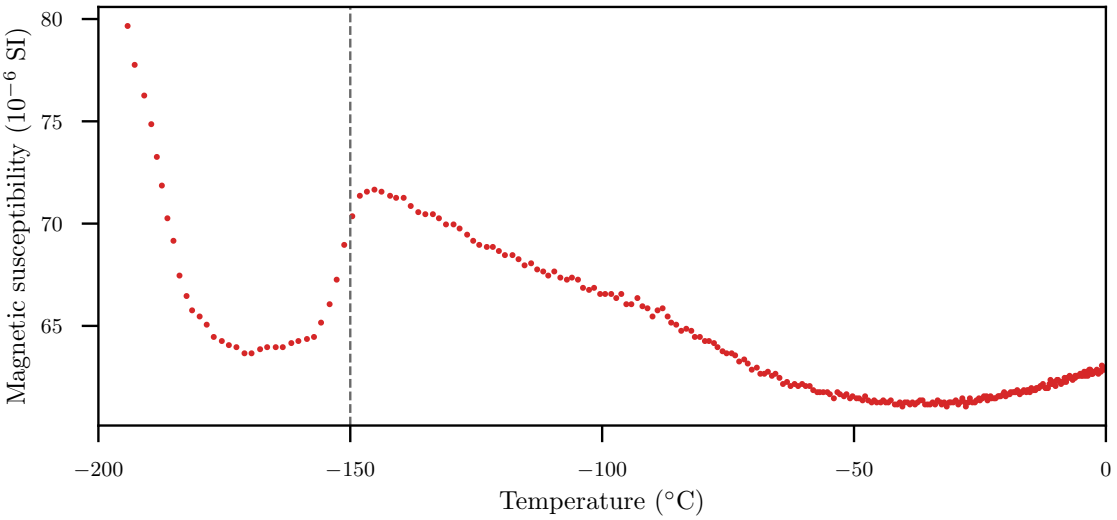

Figure A.2: Low temperature thermomagnetic curve of representative sample from site CR01 (dashed line indicates the Vervey Transition temperature of magnetite [-150 °C]).

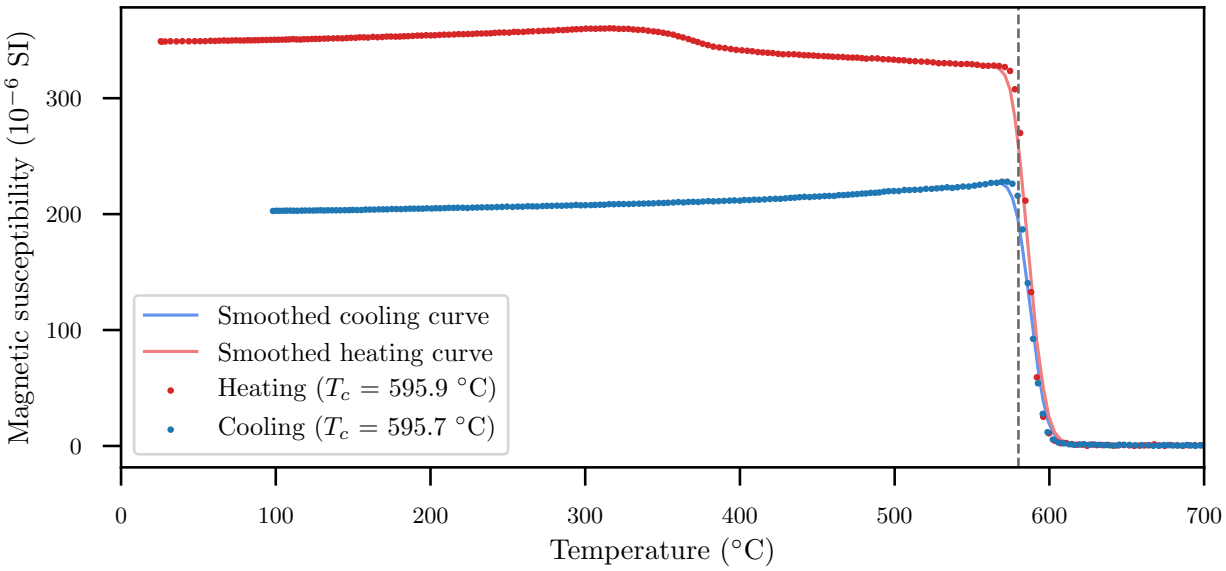

Figure A.3: High temperature thermomagnetic curve of representative sample from site CR02 (dashed line indicates the T_C of magnetite [580 °C]).

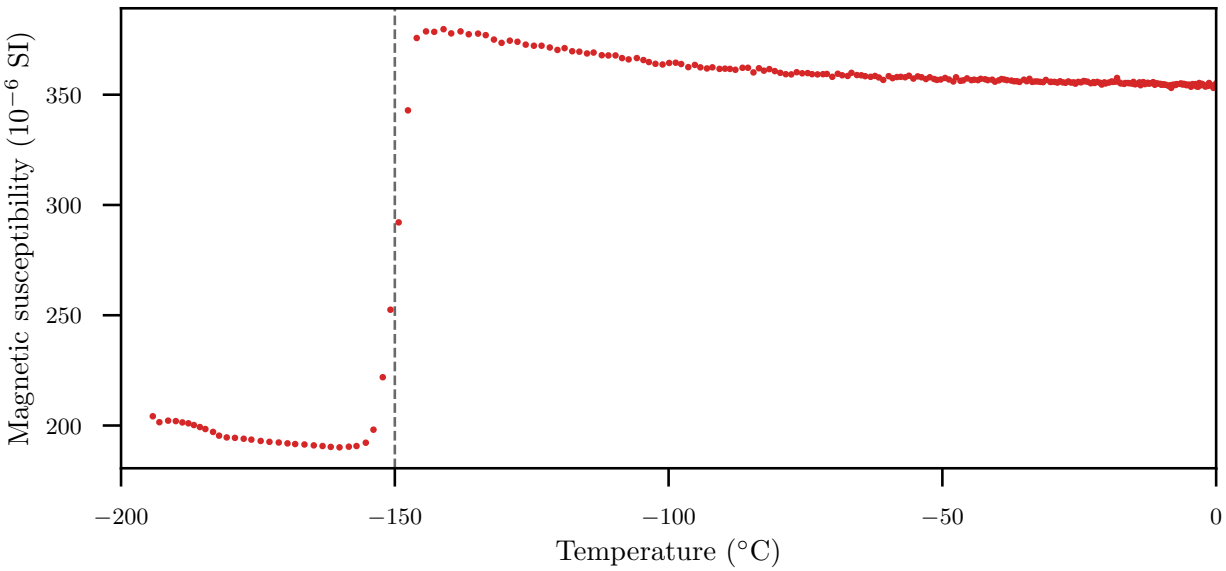

Figure A.4: Low temperature thermomagnetic curve of representative sample from site CR02 (dashed line indicates the Vervey Transition temperature of magnetite [-150 °C]).

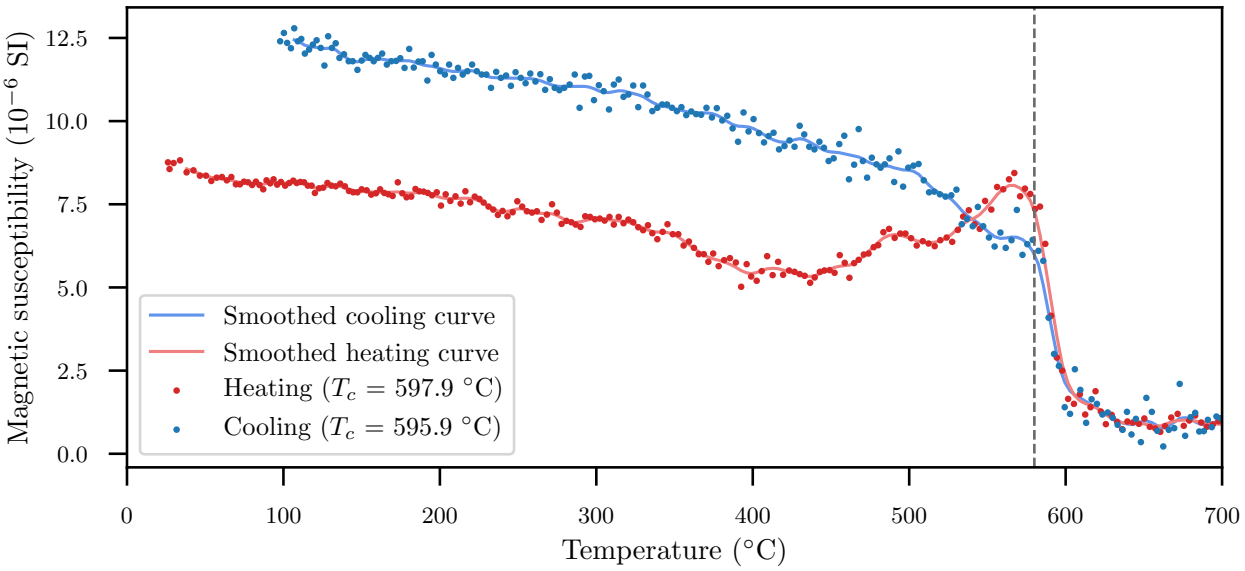

Figure A.5: High temperature thermomagnetic curve of representative sample from site CR03 (dashed line indicates the T_C of magnetite [580 °C]).

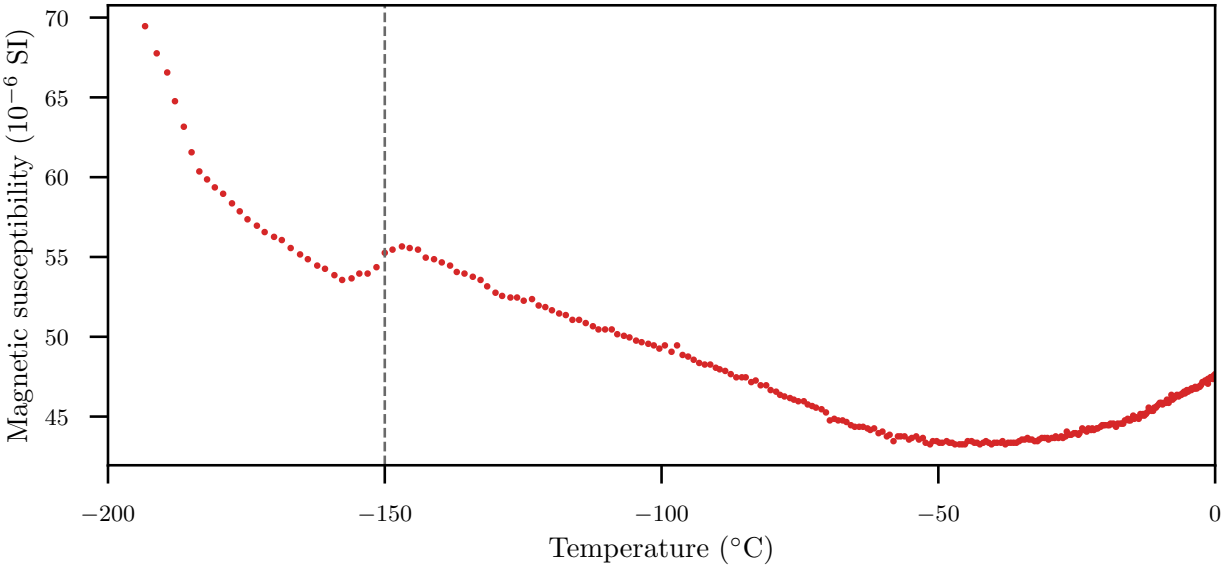

Figure A.6: Low temperature thermomagnetic curve of representative sample from site CR03 (dashed line indicates the Vervey Transition temperature of magnetite [-150 °C]).

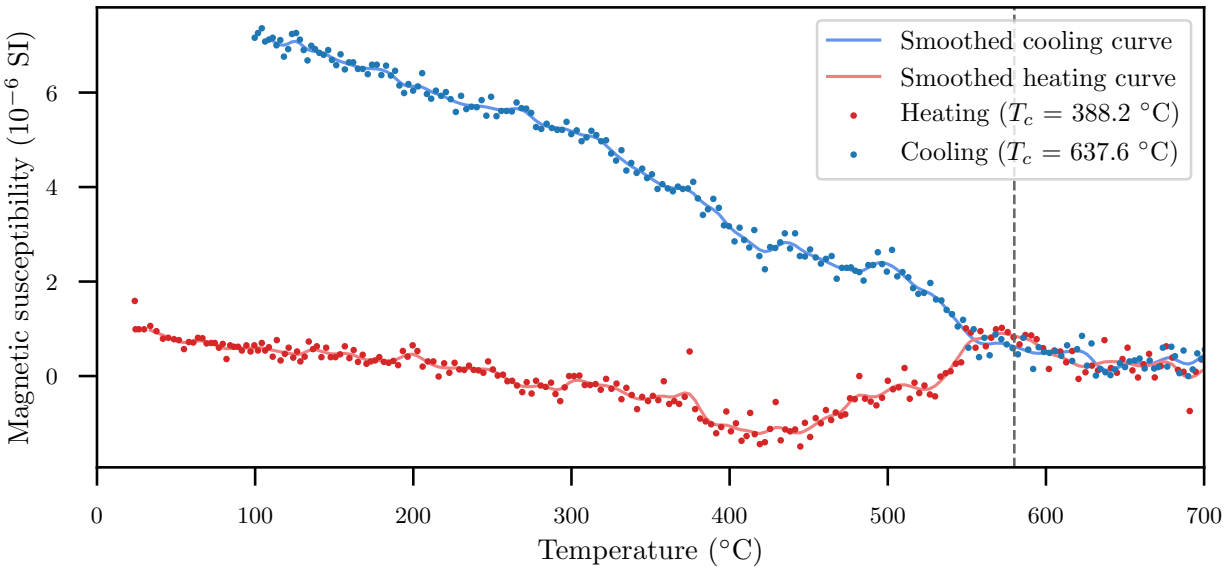

Figure A.7: High temperature thermomagnetic curve of representative sample from site CR04 (dashed line indicates the T_C of magnetite [580 °C]).

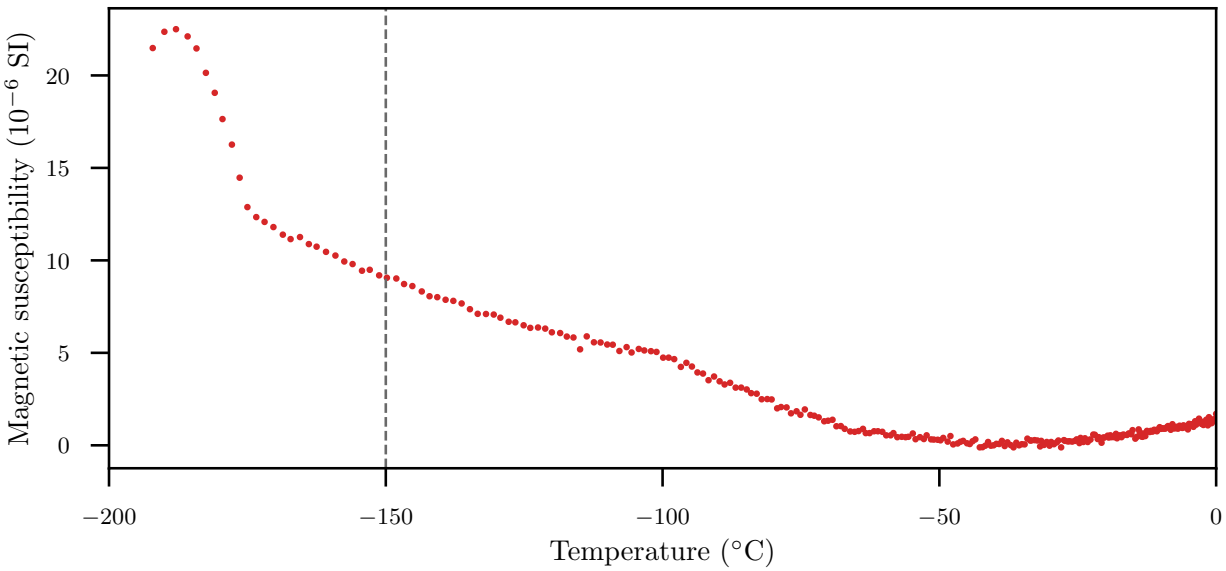

Figure A.8: Low temperature thermomagnetic curve of representative sample from site CR04 (dashed line indicates the Vervey Transition temperature of magnetite [-150 °C]).

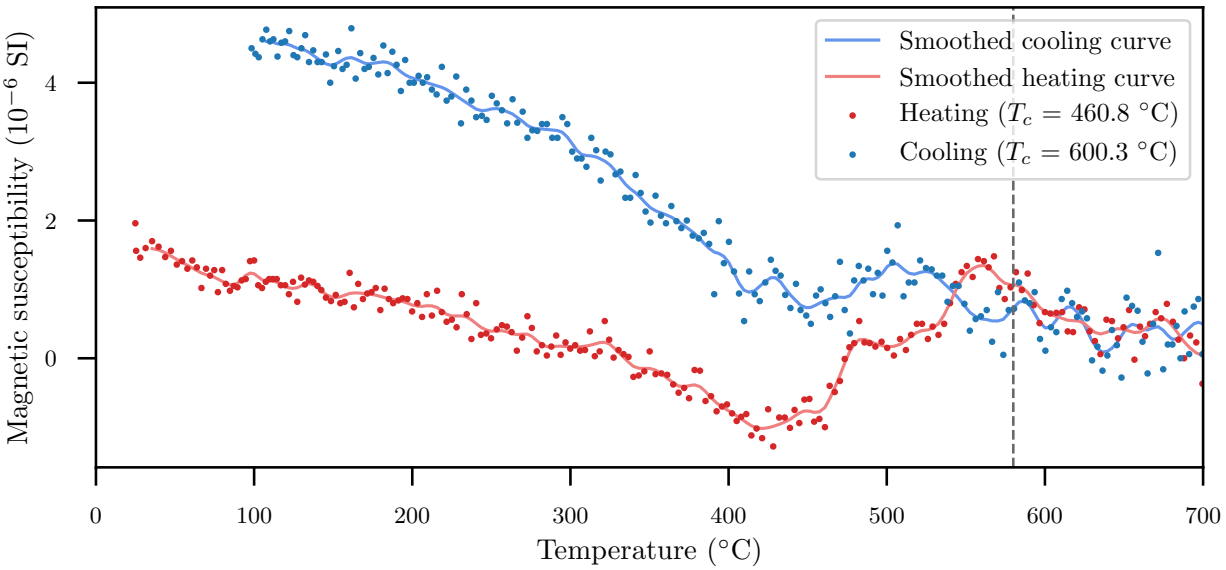

Figure A.9: High temperature thermomagnetic curve of representative sample from site CR05 (dashed line indicates the T_C of magnetite [580 °C]).

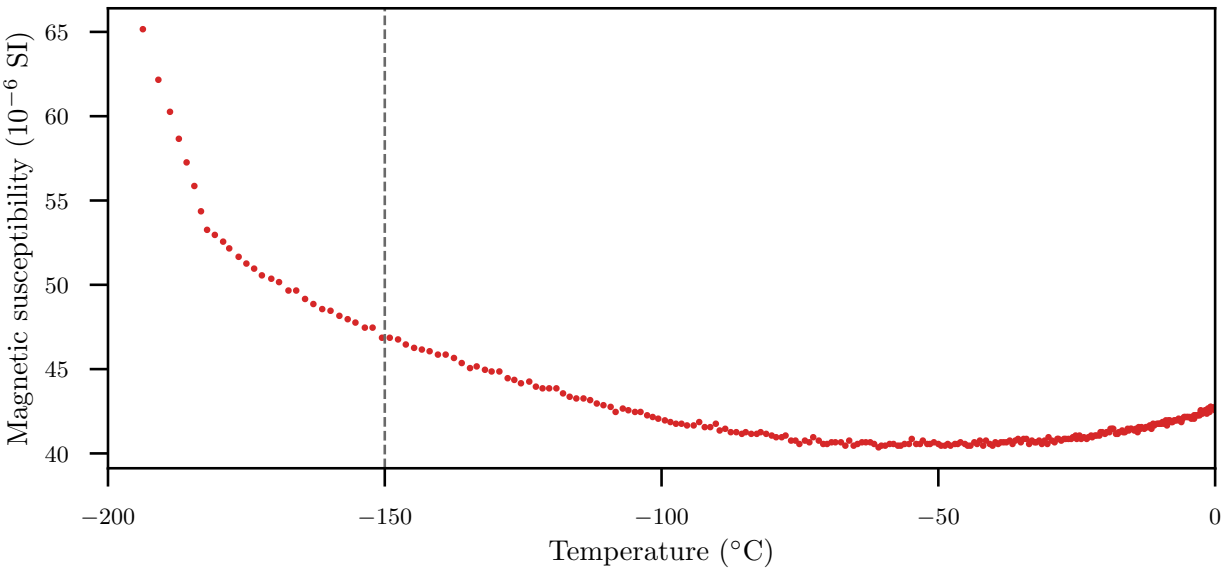

Figure A.10: Low temperature thermomagnetic curve of representative sample from site CR05 (dashed line indicates the Vervey Transition temperature of magnetite [-150 °C]).

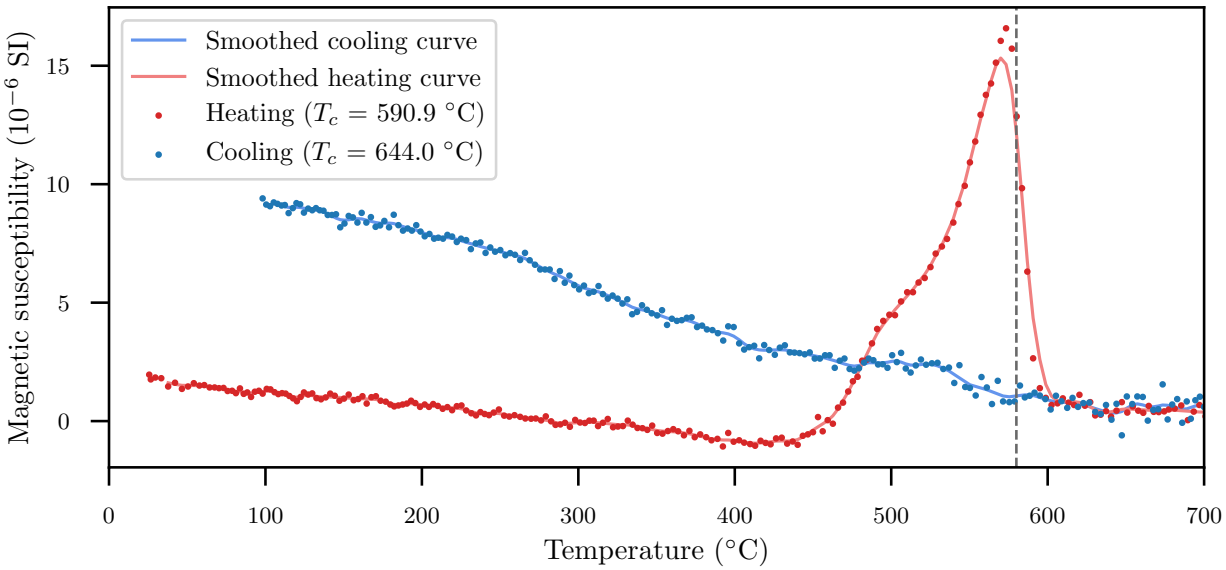

Figure A.11: High temperature thermomagnetic curve of representative sample from site CR06 (dashed line indicates the T_C of magnetite [580 °C]).

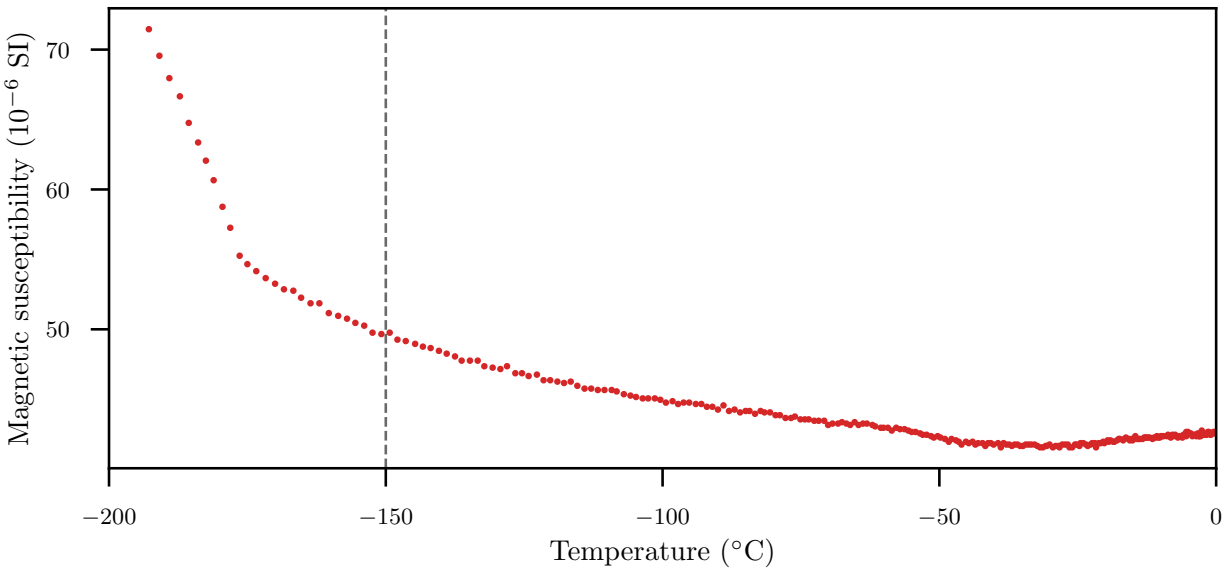

Figure A.12: Low temperature thermomagnetic curve of representative sample from site CR06 (dashed line indicates the Vervey Transition temperature of magnetite [-150 °C]).

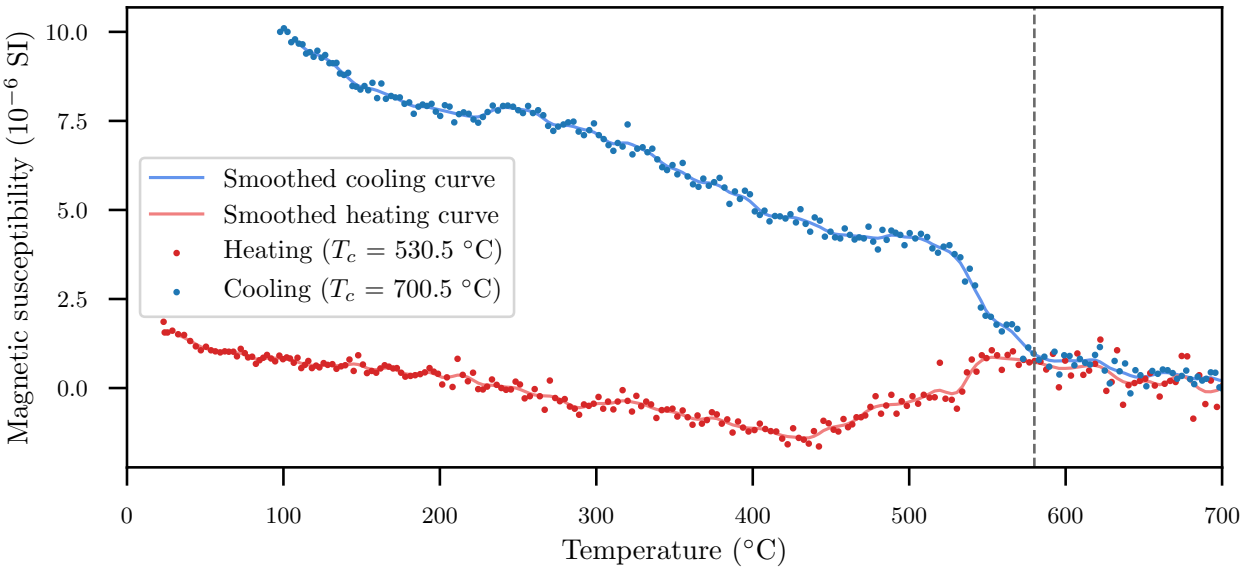

Figure A.13: High temperature thermomagnetic curve of representative sample from site CR07 (dashed line indicates the T_C of magnetite [580 °C]).

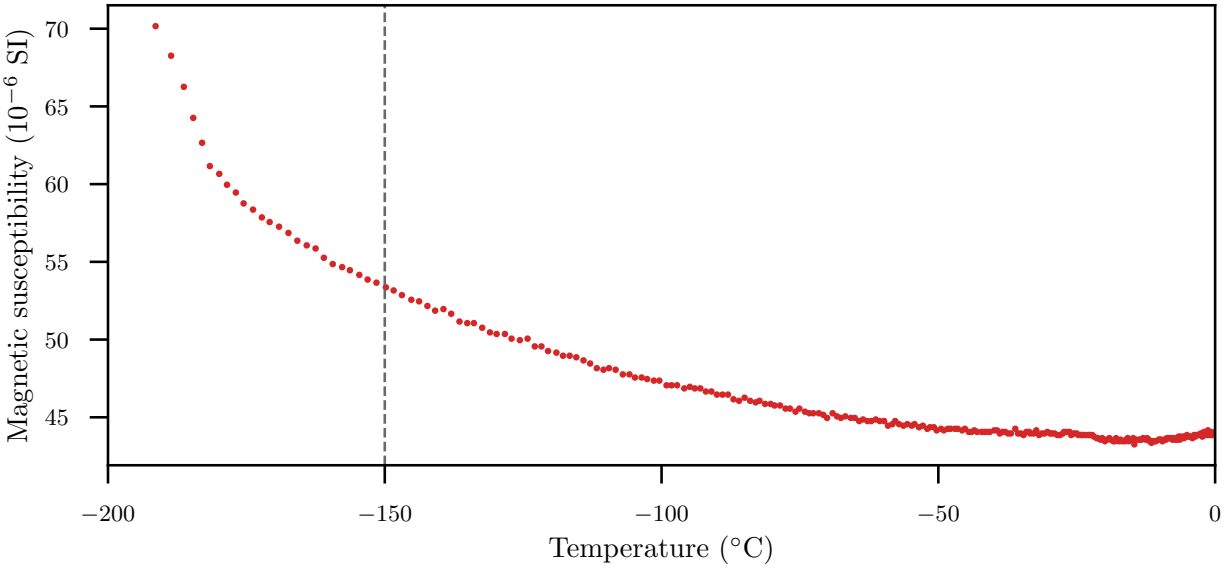

Figure A.14: Low temperature thermomagnetic curve of representative sample from site CR07 (dashed line indicates the Vervey Transition temperature of magnetite [-150 °C]).

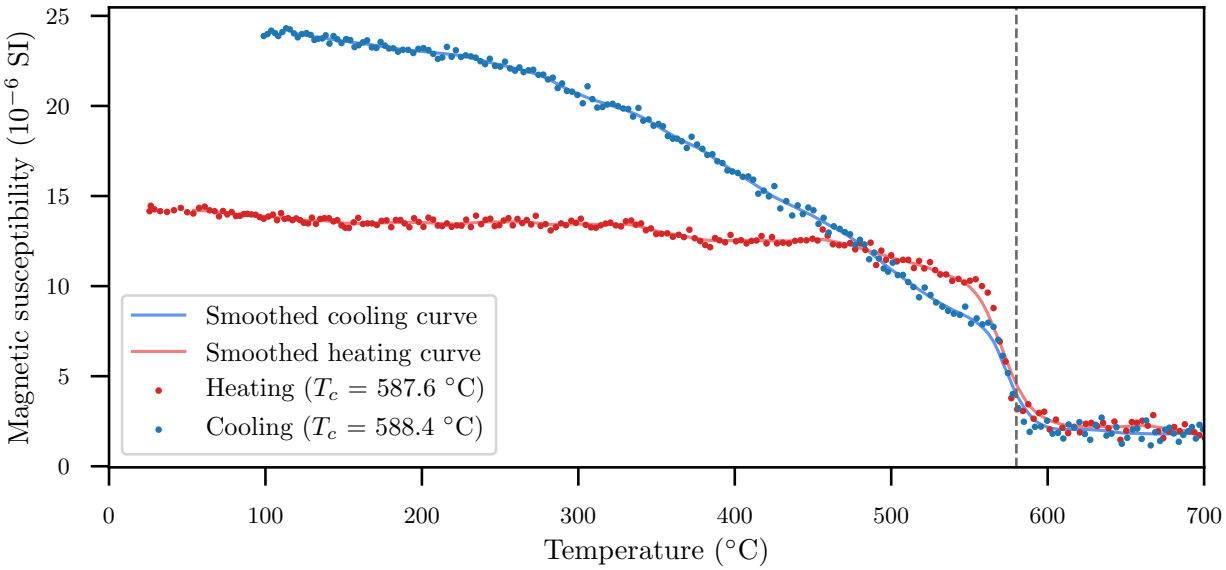

Figure A.15: High temperature thermomagnetic curve of representative sample from site SM01 (dashed line indicates the T_C of magnetite [580 °C]).

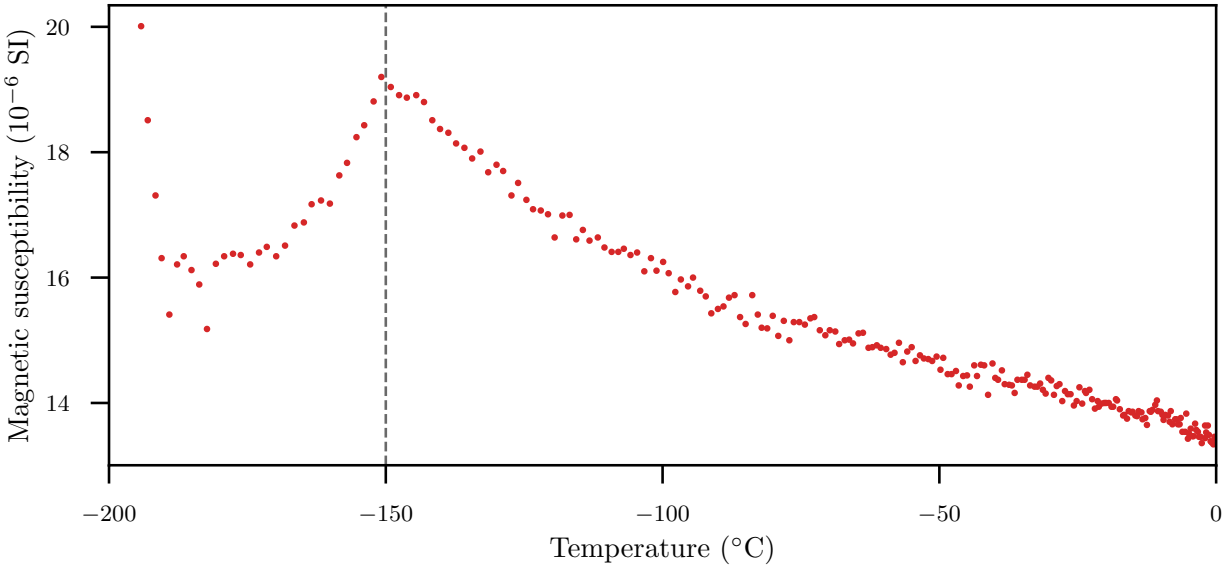

Figure A.16: Low temperature thermomagnetic curve of representative sample from site SM01 (dashed line indicates the Vervey Transition temperature of magnetite [-150 °C]).

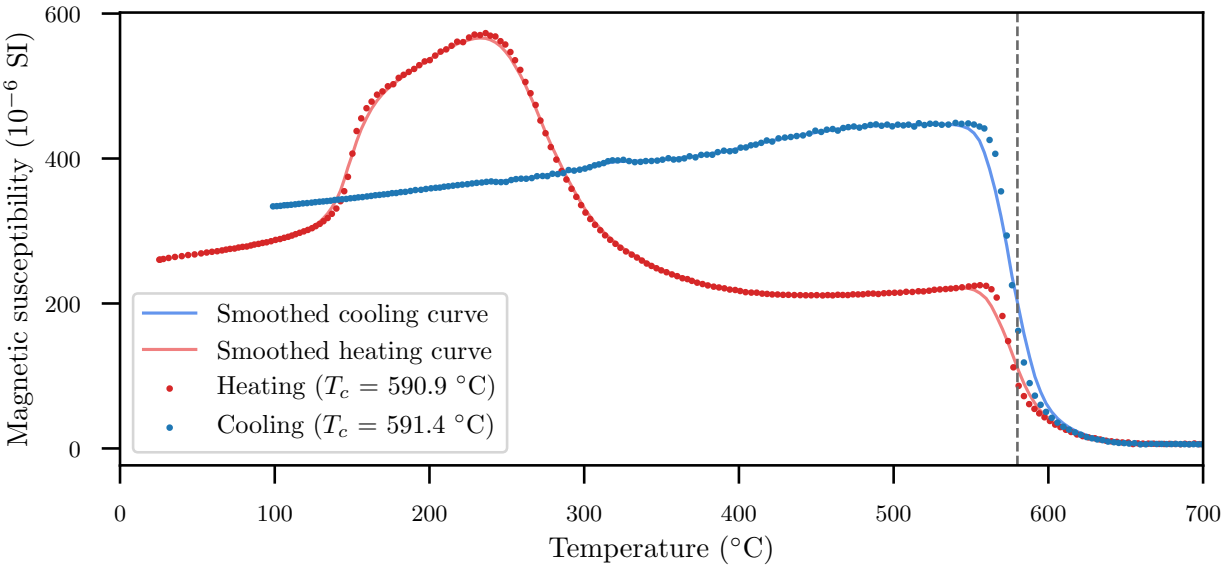

Figure A.17: High temperature thermomagnetic curve of representative sample from site SM02 (dashed line indicates the T_C of magnetite [580 °C]).

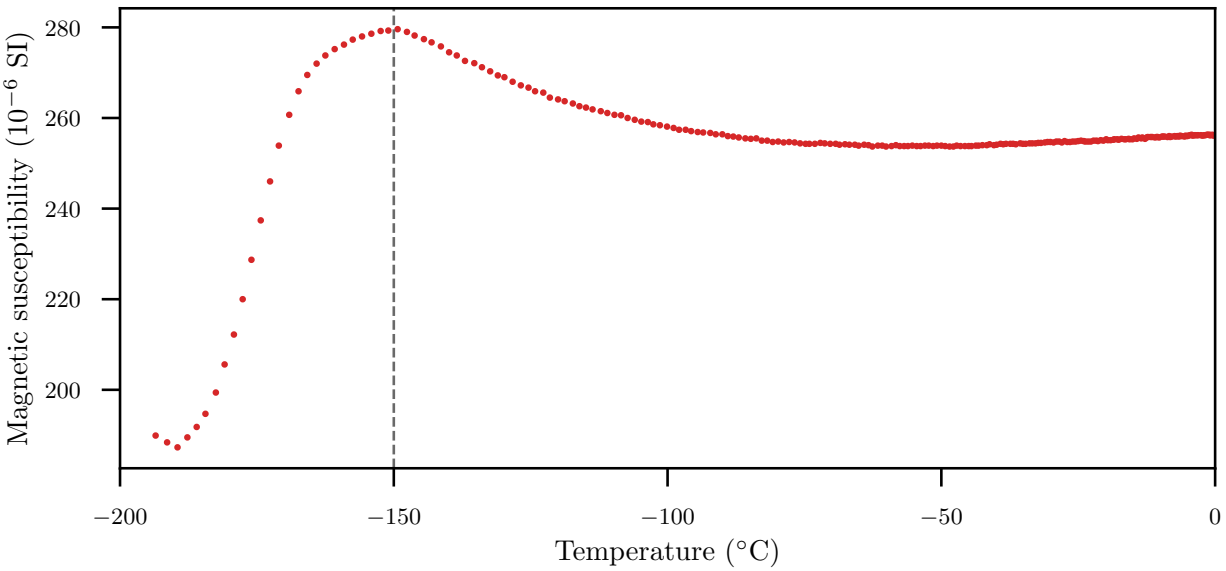

Figure A.18: Low temperature thermomagnetic curve of representative sample from site SM02 (dashed line indicates the Vervey Transition temperature of magnetite [-150 °C]).

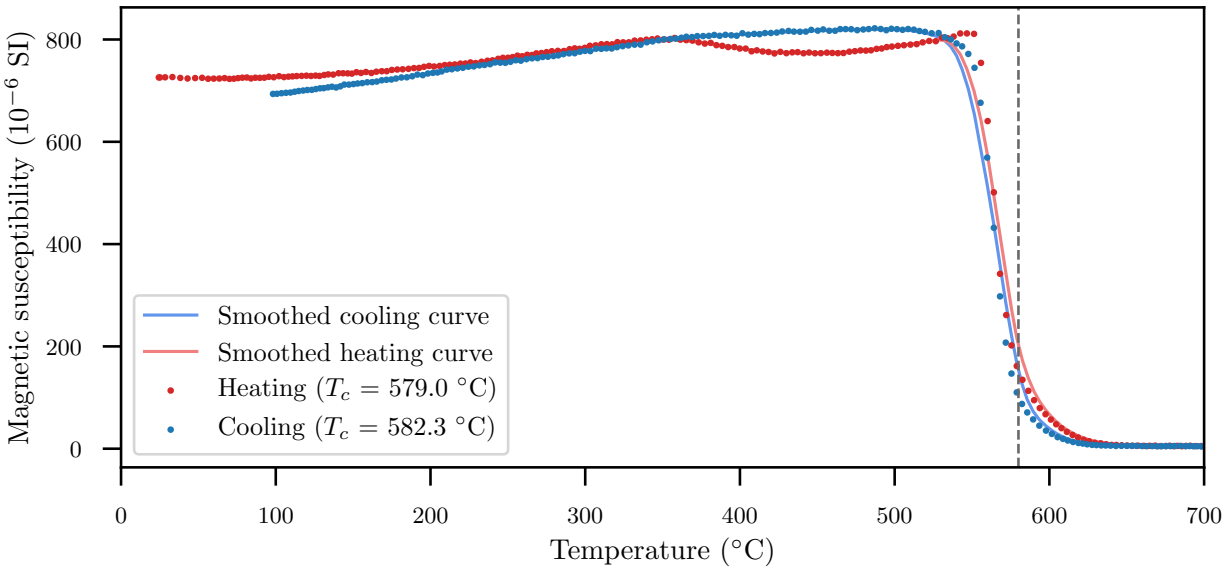

Figure A.19: High temperature thermomagnetic curve of representative sample from site SM03 (dashed line indicates the T_C of magnetite [580 °C]).

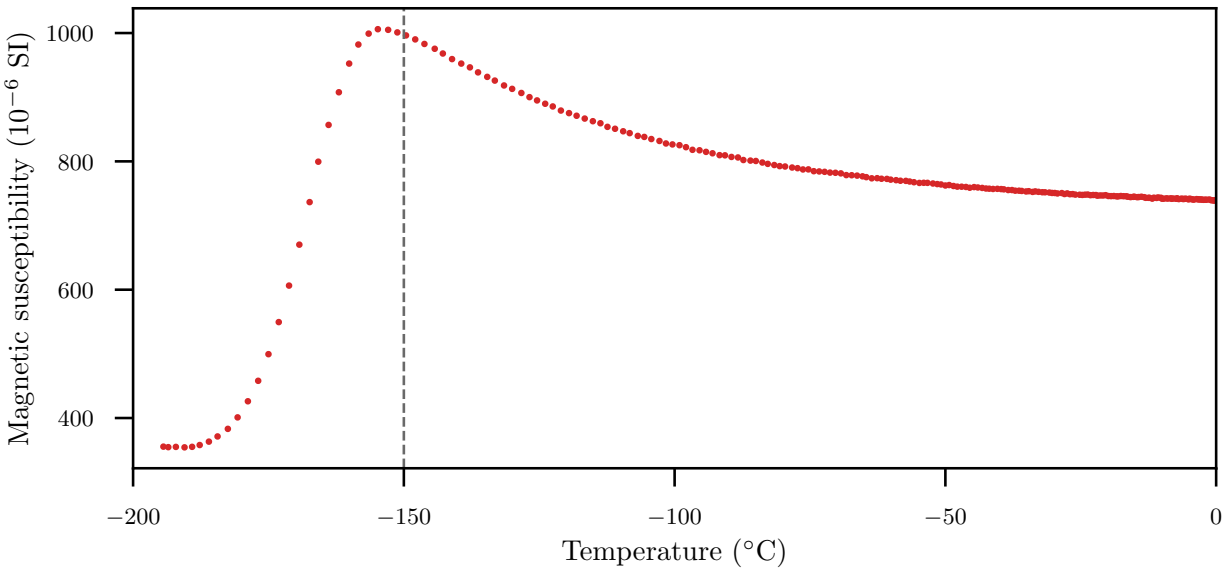

Figure A.20: Low temperature thermomagnetic curve of representative sample from site SM03 (dashed line indicates the Vervey Transition temperature of magnetite [-150 °C]).

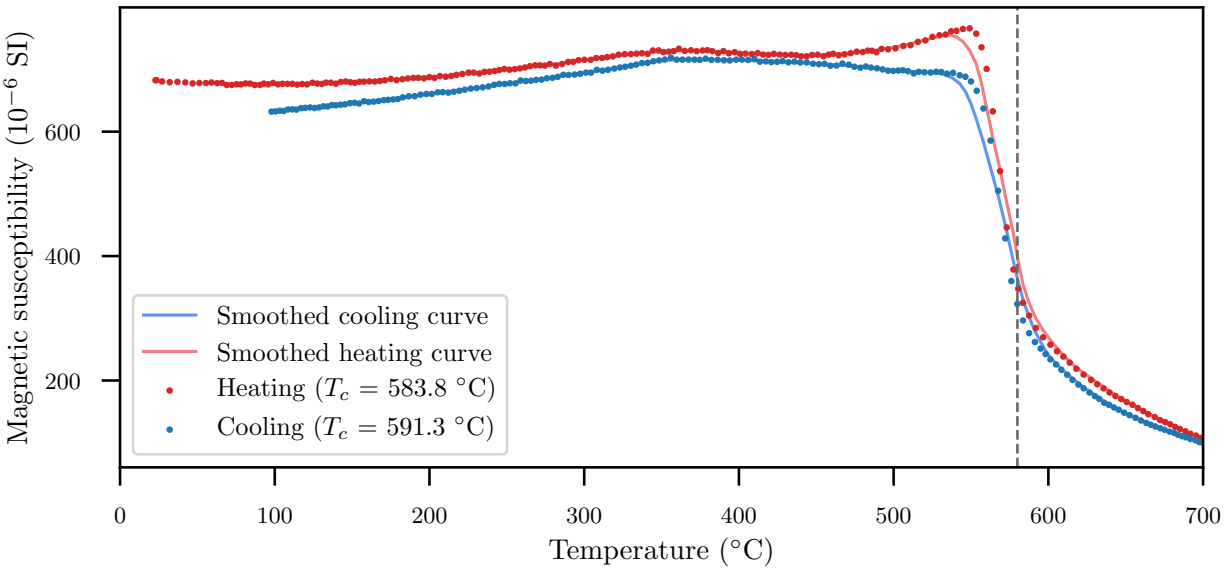

Figure A.21: High temperature thermomagnetic curve of representative sample from site SM04 (dashed line indicates the T_C of magnetite [580 °C]).

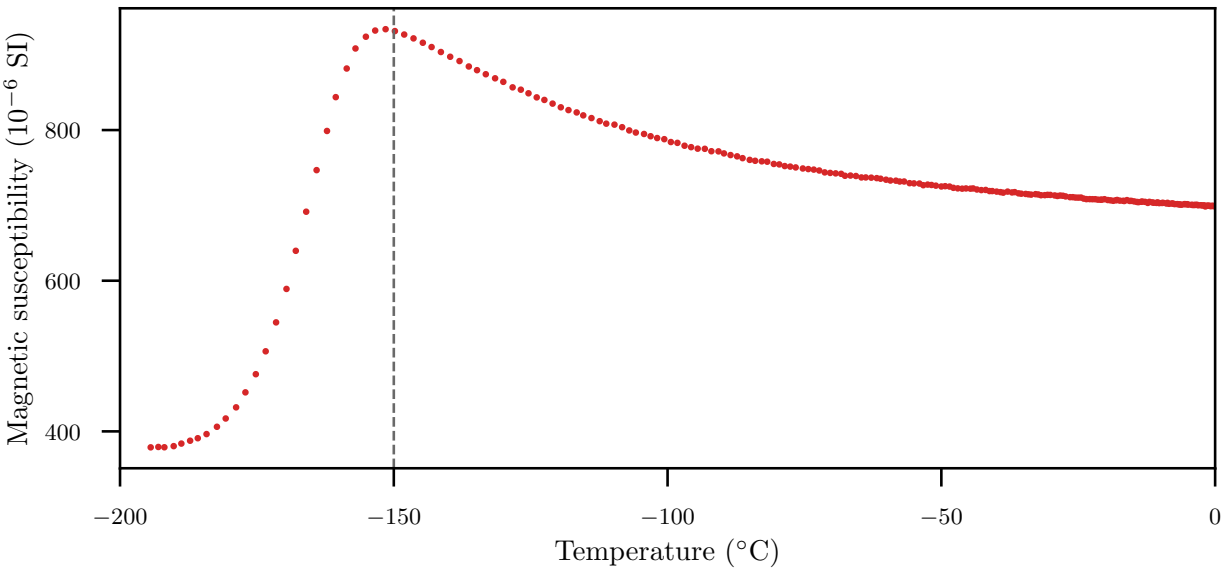

Figure A.22: Low temperature thermomagnetic curve of representative sample from site SM04 (dashed line indicates the Vervey Transition temperature of magnetite [-150 °C]).

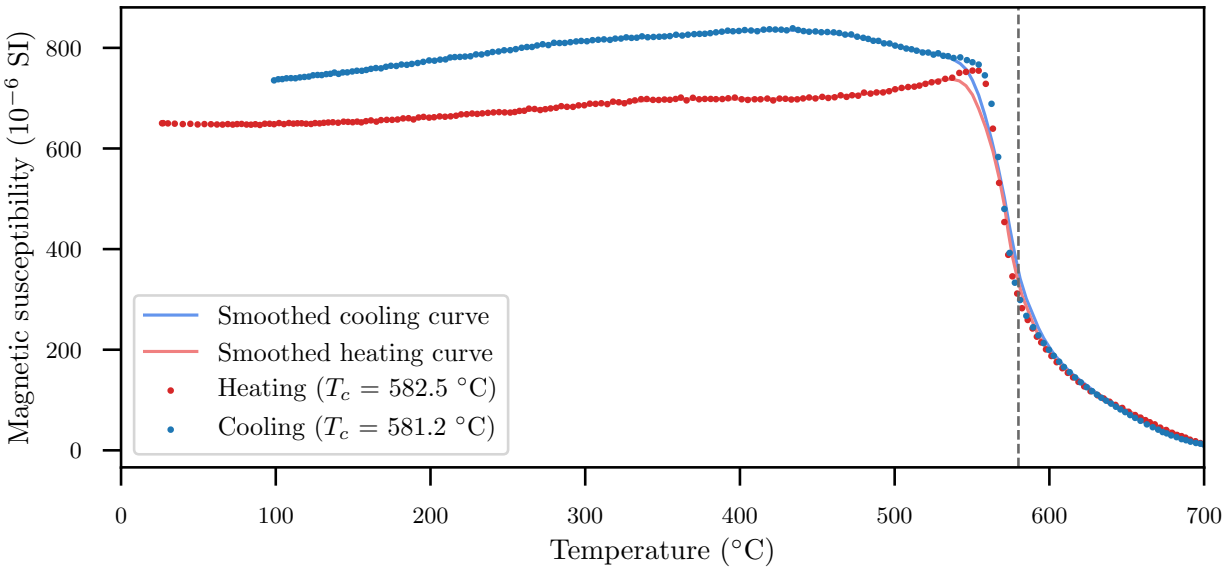

Figure A.23: High temperature thermomagnetic curve of representative sample from site SM05 (dashed line indicates the T_C of magnetite [580 °C]).

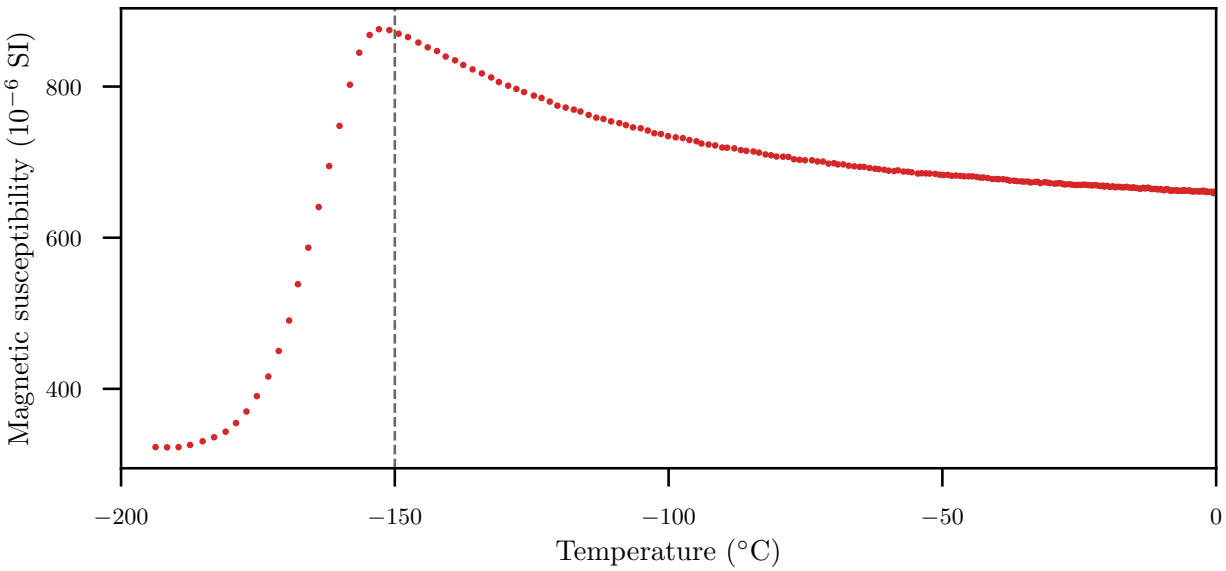

Figure A.24: Low temperature thermomagnetic curve of representative sample from site SM05 (dashed line indicates the Vervey Transition temperature of magnetite [-150 °C]).

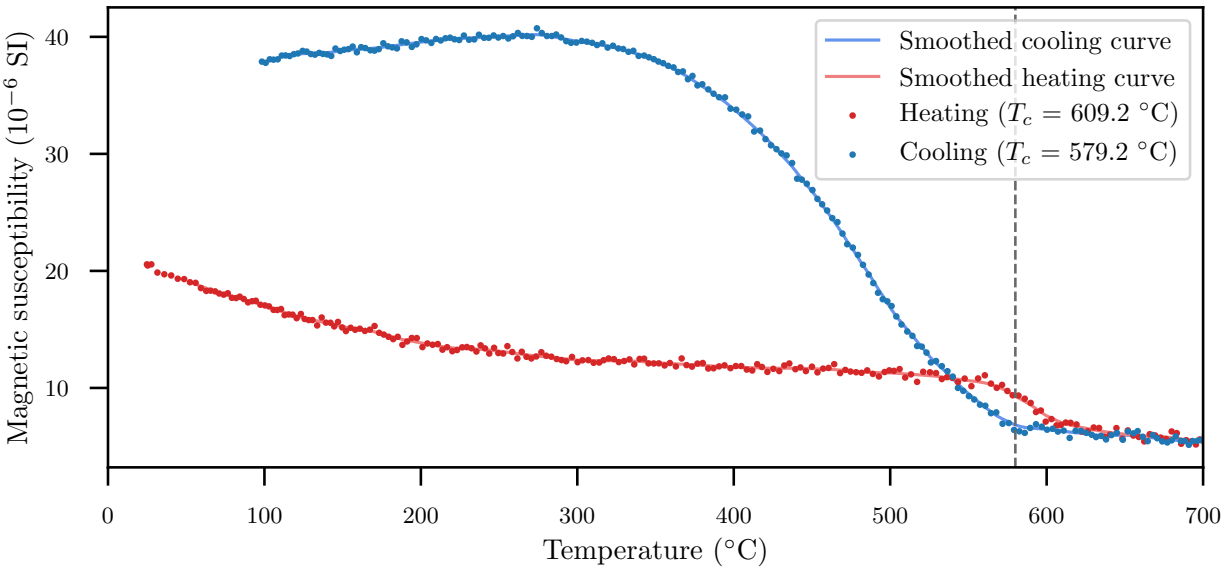

Figure A.25: High temperature thermomagnetic curve of representative sample from site SM06 (dashed line indicates the T_C of magnetite [580 °C]).

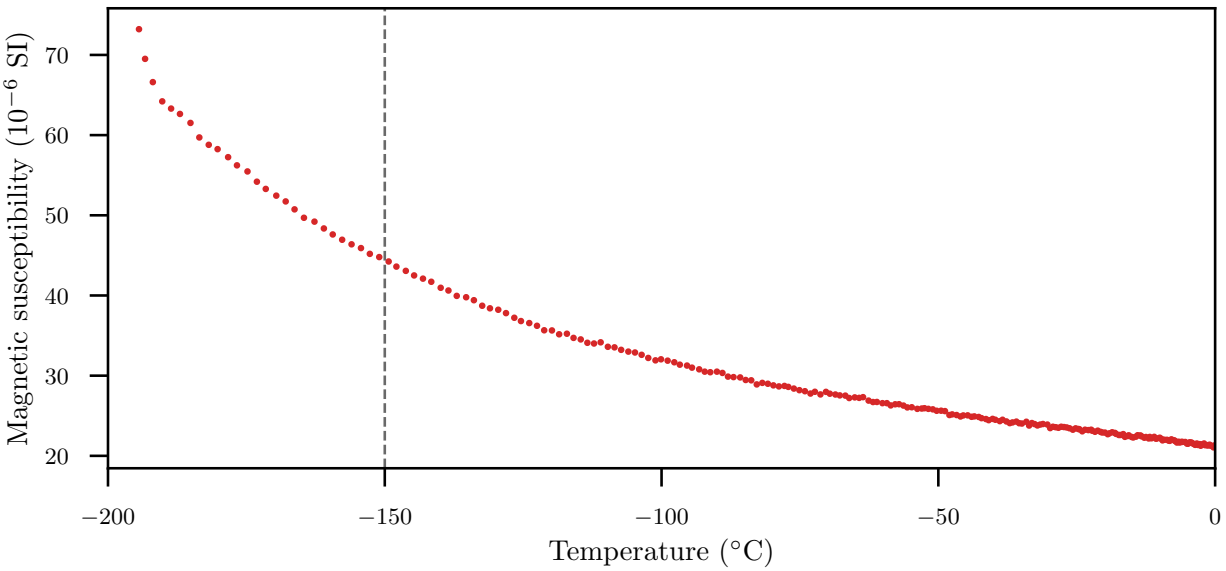

Figure A.26: Low temperature thermomagnetic curve of representative sample from site SM06 (dashed line indicates the Vervey Transition temperature of magnetite [-150 °C]).

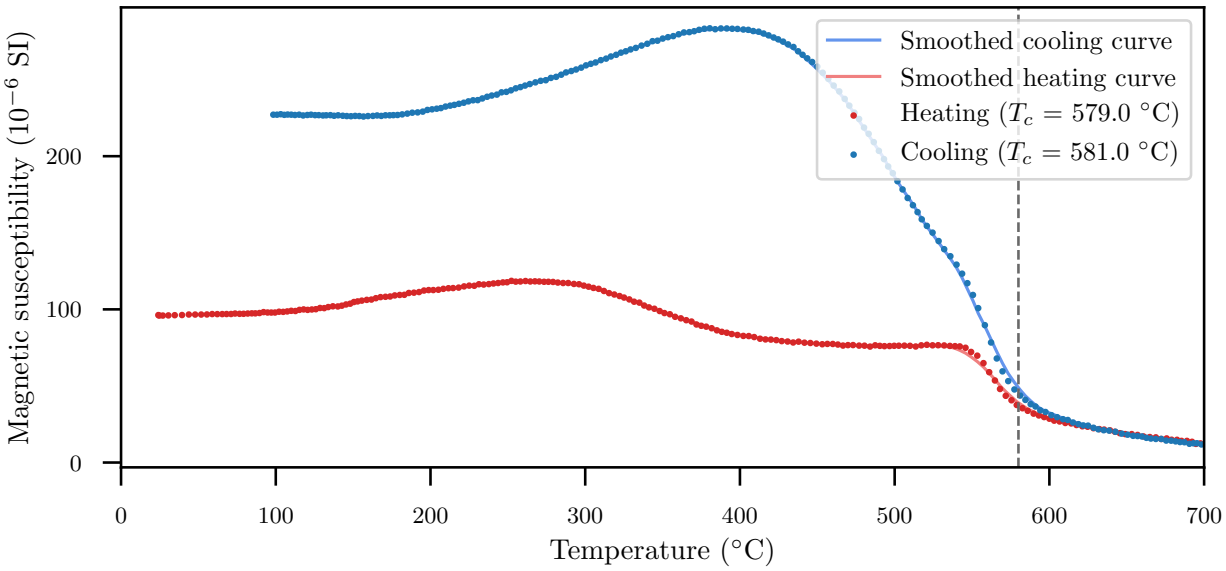

Figure A.27: High temperature thermomagnetic curve of representative sample from site SM07 (dashed line indicates the T_C of magnetite [580 °C]).

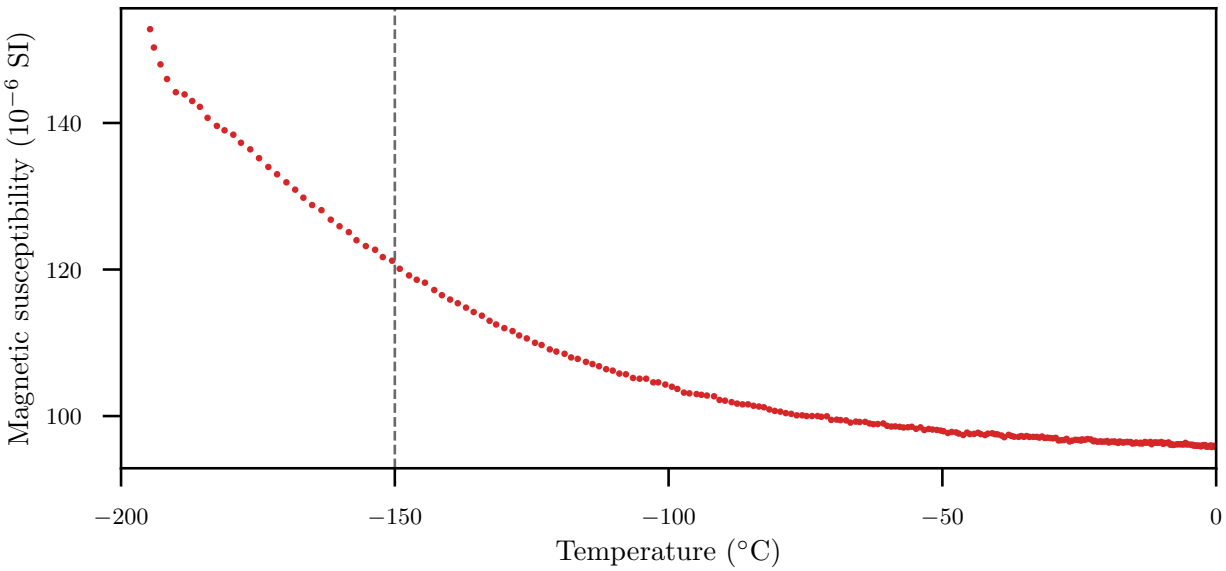

Figure A.28: Low temperature thermomagnetic curve of representative sample from site SM07 (dashed line indicates the Vervey Transition temperature of magnetite [-150 °C]).

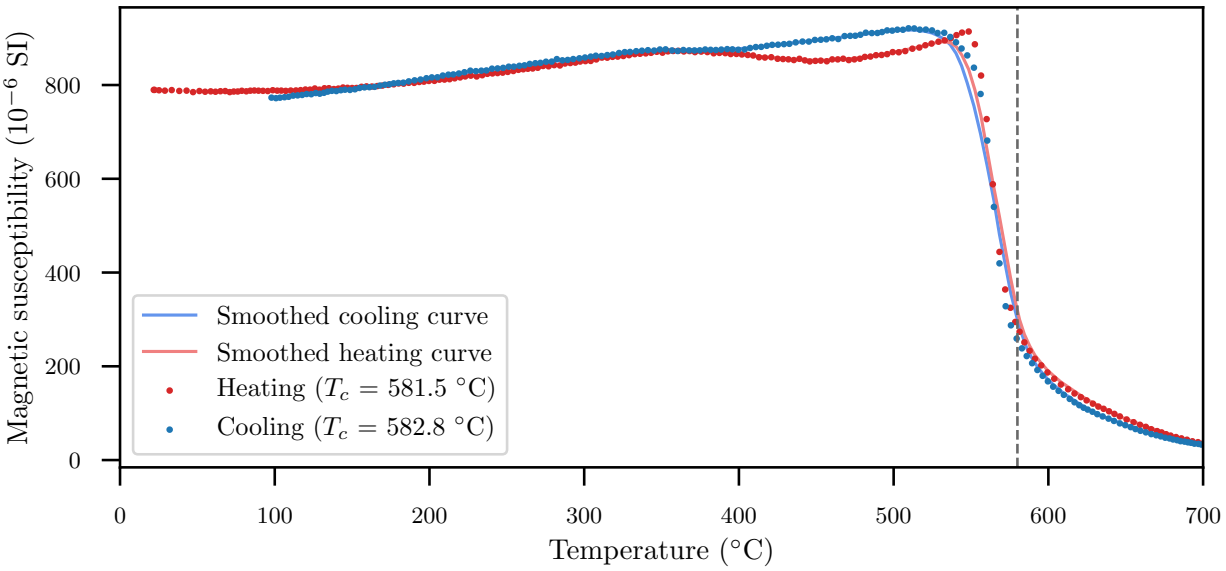

Figure A.29: High temperature thermomagnetic curve of representative sample from site SM08 (dashed line indicates the T_C of magnetite [580 °C]).

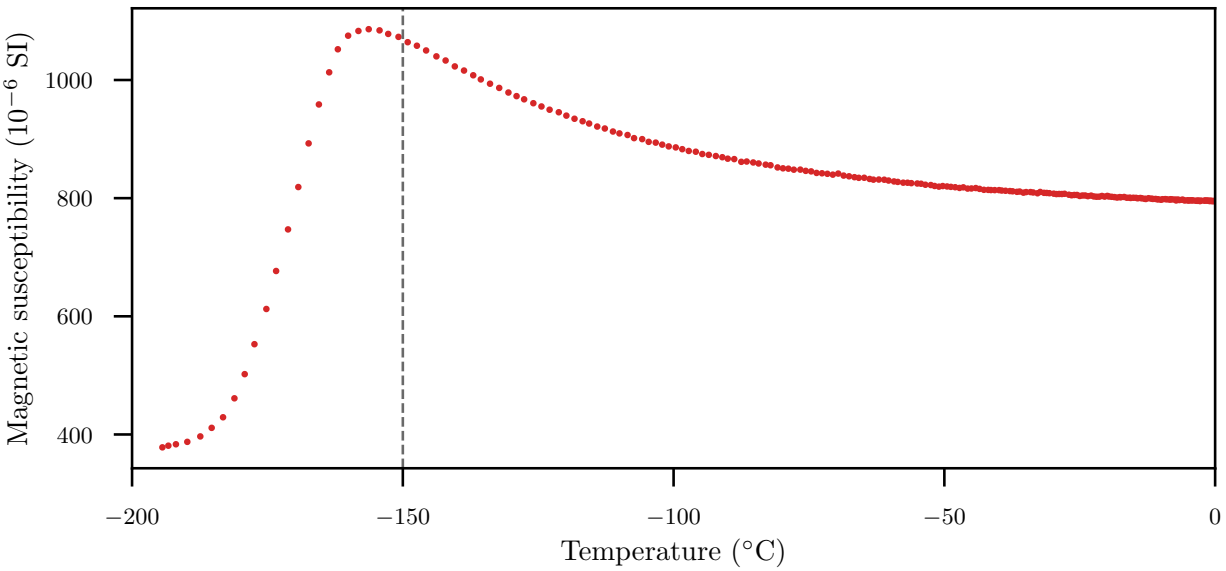

Figure A.30: Low temperature thermomagnetic curve of representative sample from site SM08 (dashed line indicates the Vervey Transition temperature of magnetite [-150 °C]).

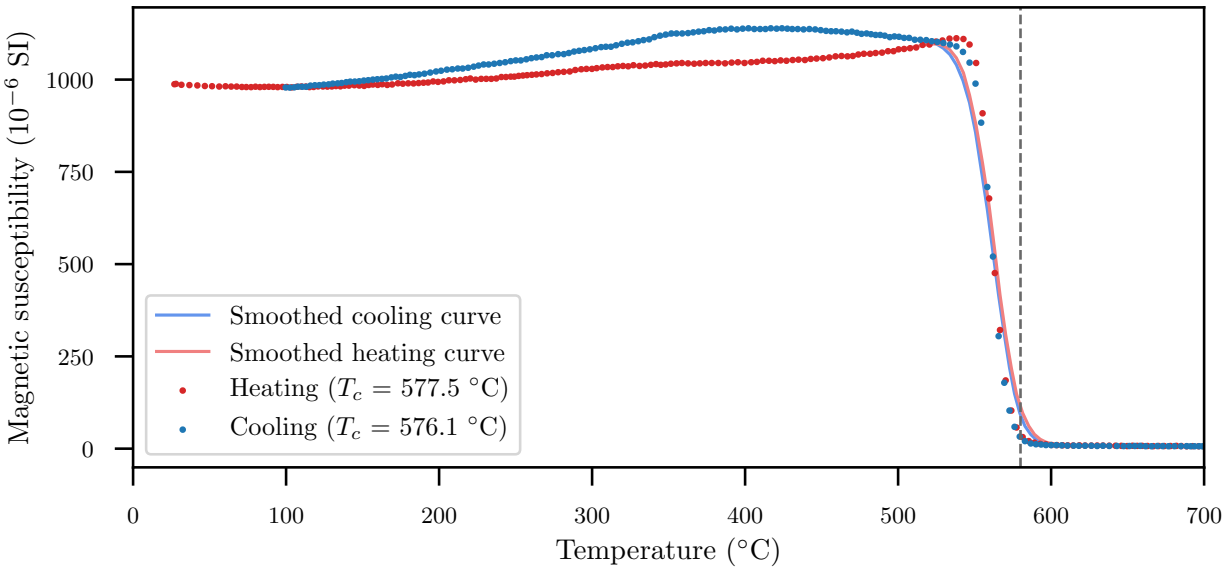

Figure A.31: High temperature thermomagnetic curve of representative sample from site SJ (dashed line indicates the T_C of magnetite [580 °C]).

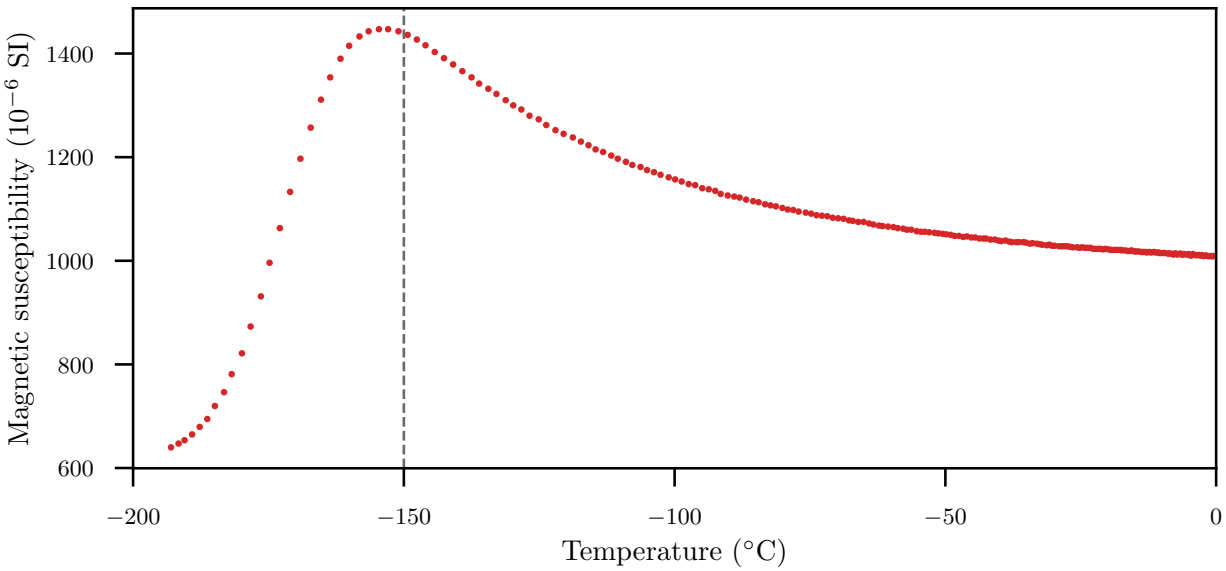

Figure A.32: Low temperature thermomagnetic curve of representative sample from site SJ (dashed line indicates the Vervey Transition temperature of magnetite [-150 °C]).

Appendix B

Hysteresis Loops

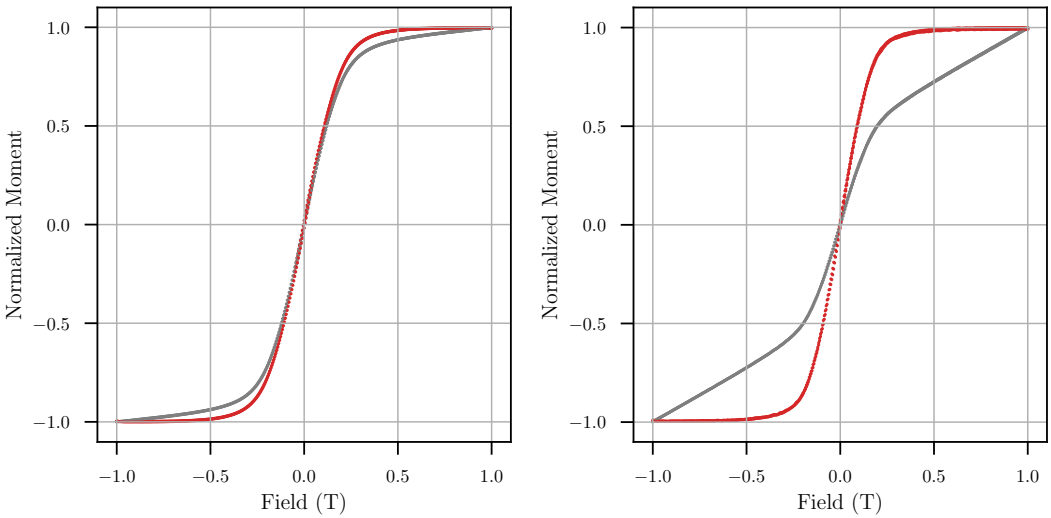

(a) CR1G1

(b) CR2B1

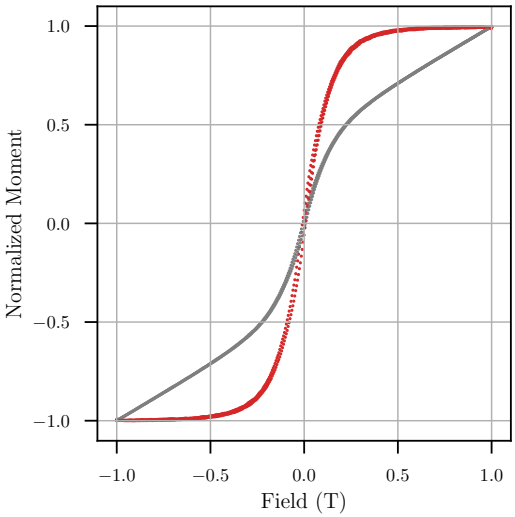

(c) CR3A1

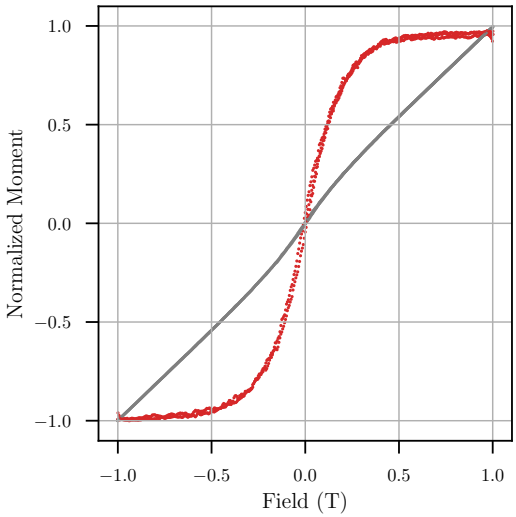

(d) CR4C2

Figure B.1: Hysteresis loops of representative samples (gray loop represent uncorrected dia/paramagnetic data and red loop represent corrected data).

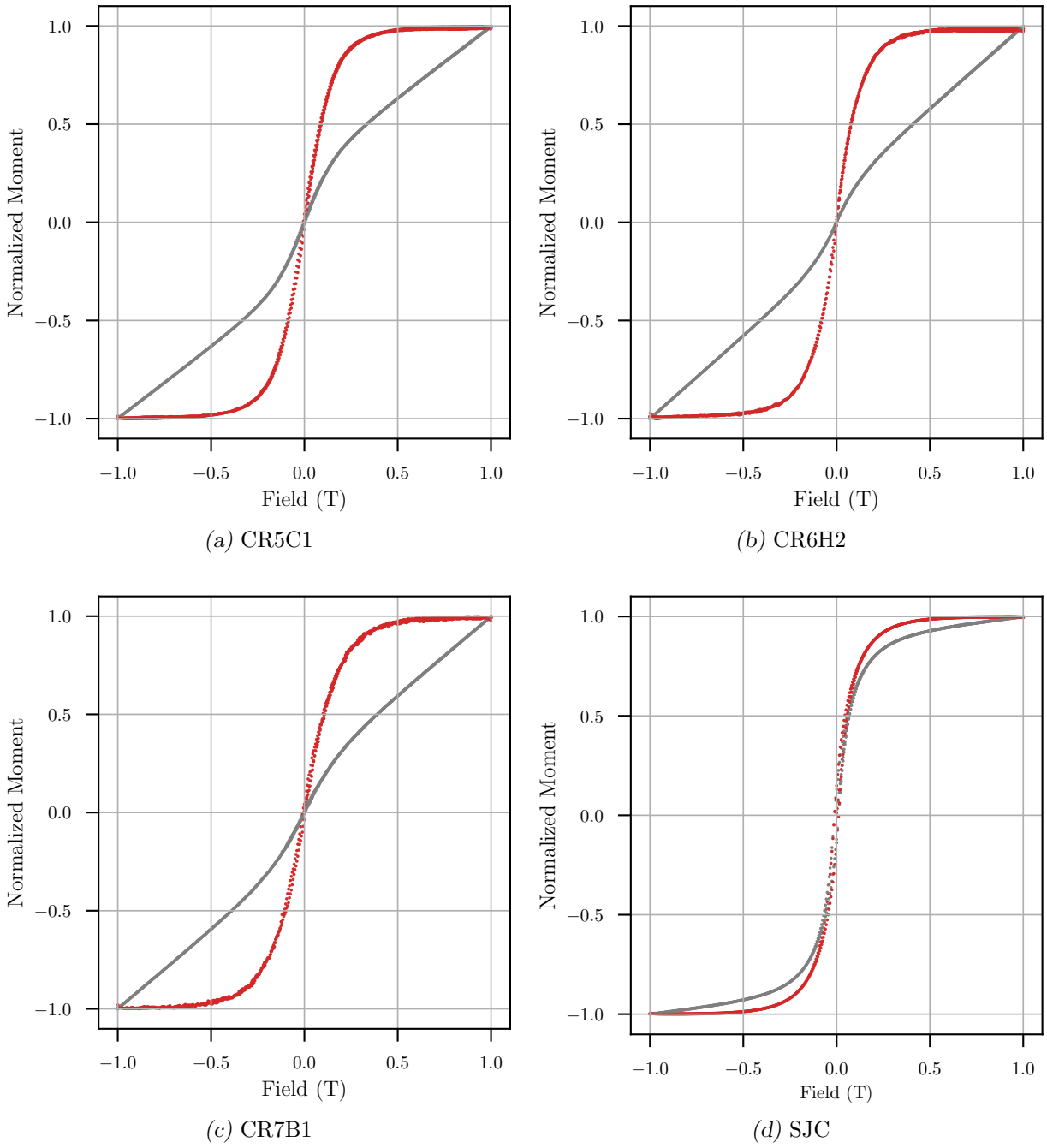

(a) CR5C1

(b) CR6H2

(c) CR7B1

(d) SJC

Figure B.2: Hysteresis loops of representative samples (gray loop represent uncorrected dia/paramagnetic data and red loop represent corrected data).

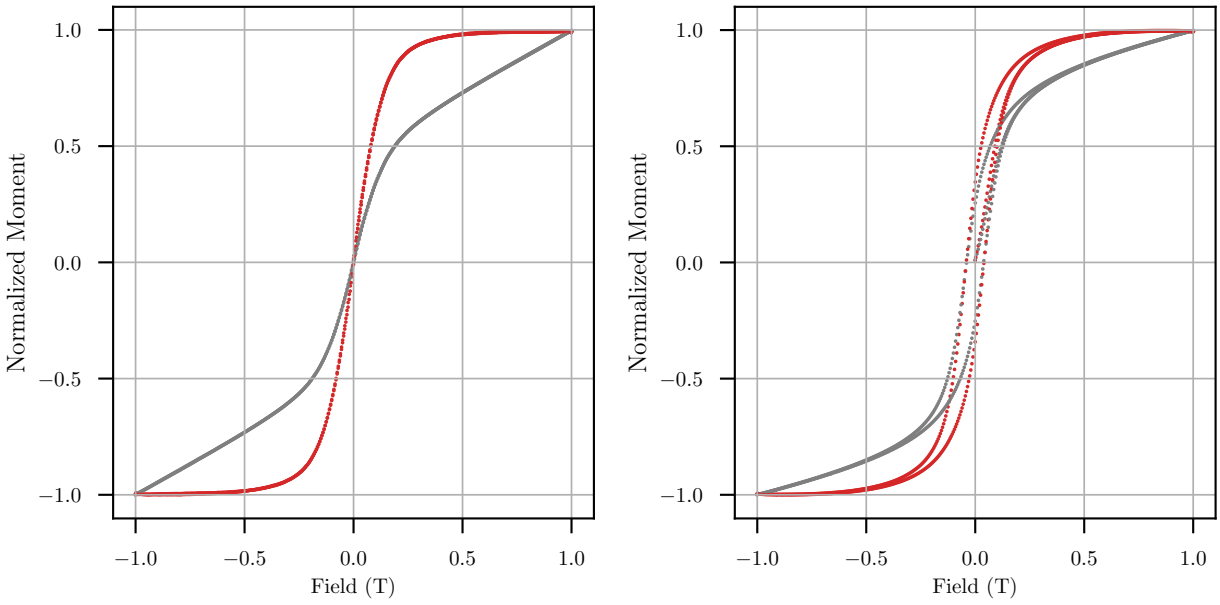

(a) SM1B

(b) SM2D

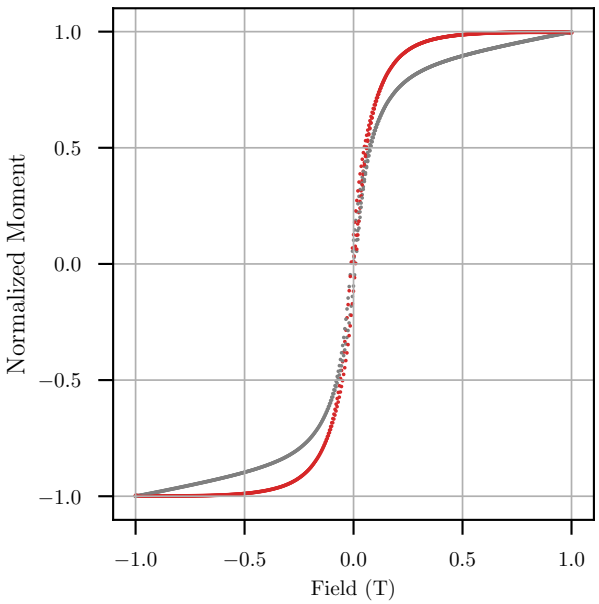

(c) SM3D

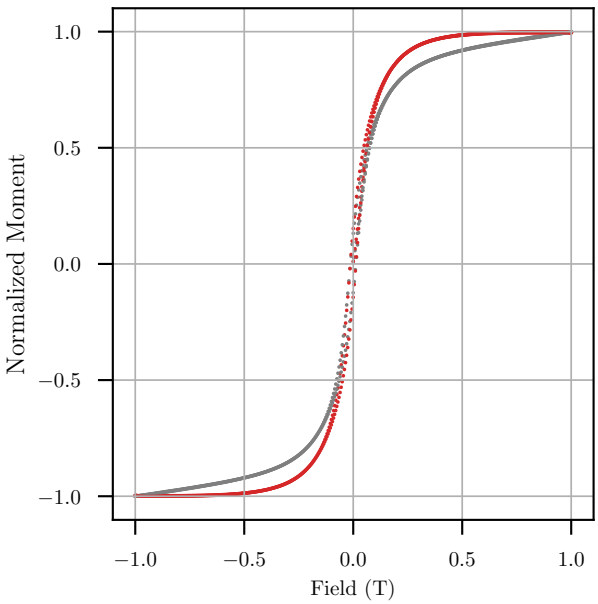

(d) SM4A

Figure B.3: Hysteresis loops of representative samples (gray loop represent uncorrected dia/paramagnetic data and red loop represent corrected data).

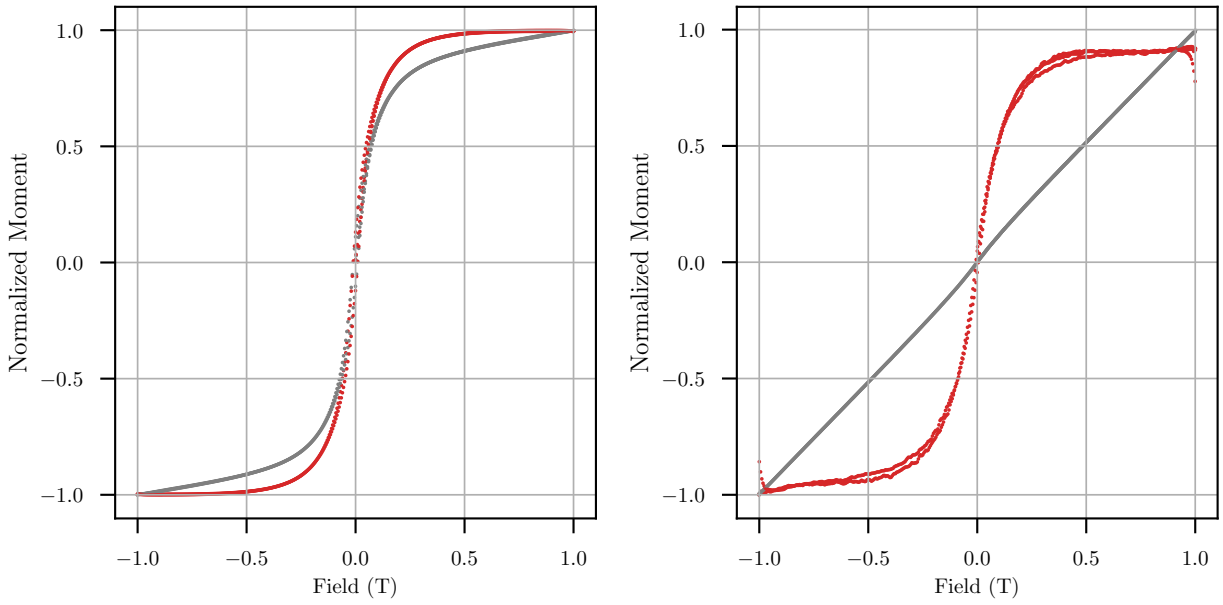

(a) SM5F *(b)* SM6D

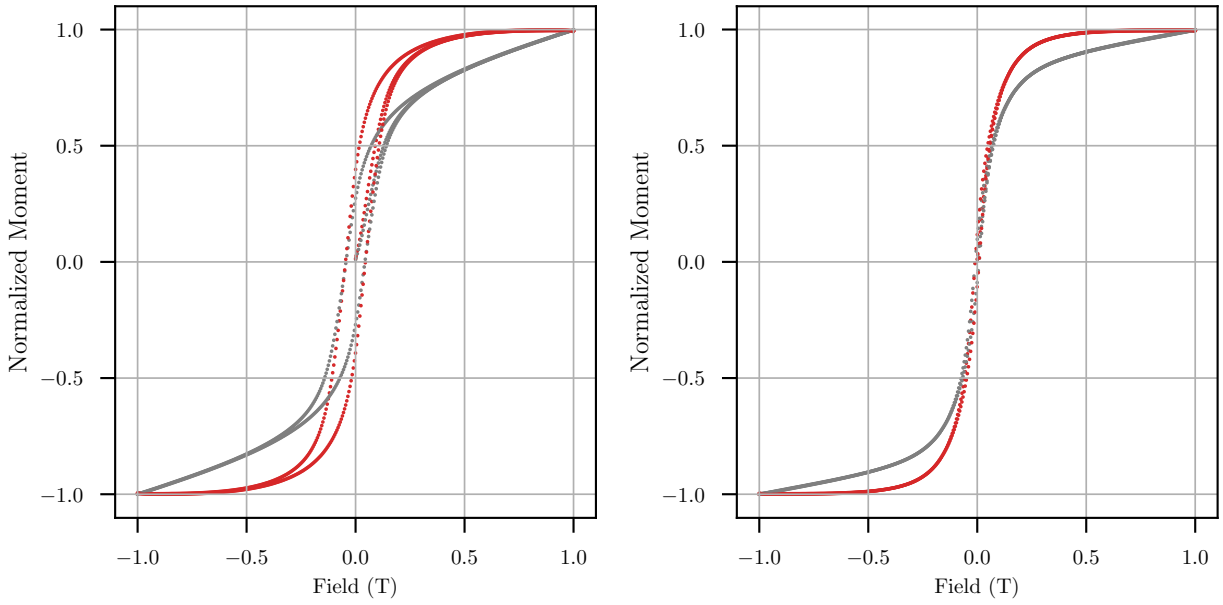

(c) SM7F *(d)* SM8I

Figure B.4: Hysteresis loops of representative samples (gray loop represent uncorrected dia/paramagnetic data and red loop represent corrected data).

Appendix C

Isothermal Remanent Curves

C.1 Rhyolite

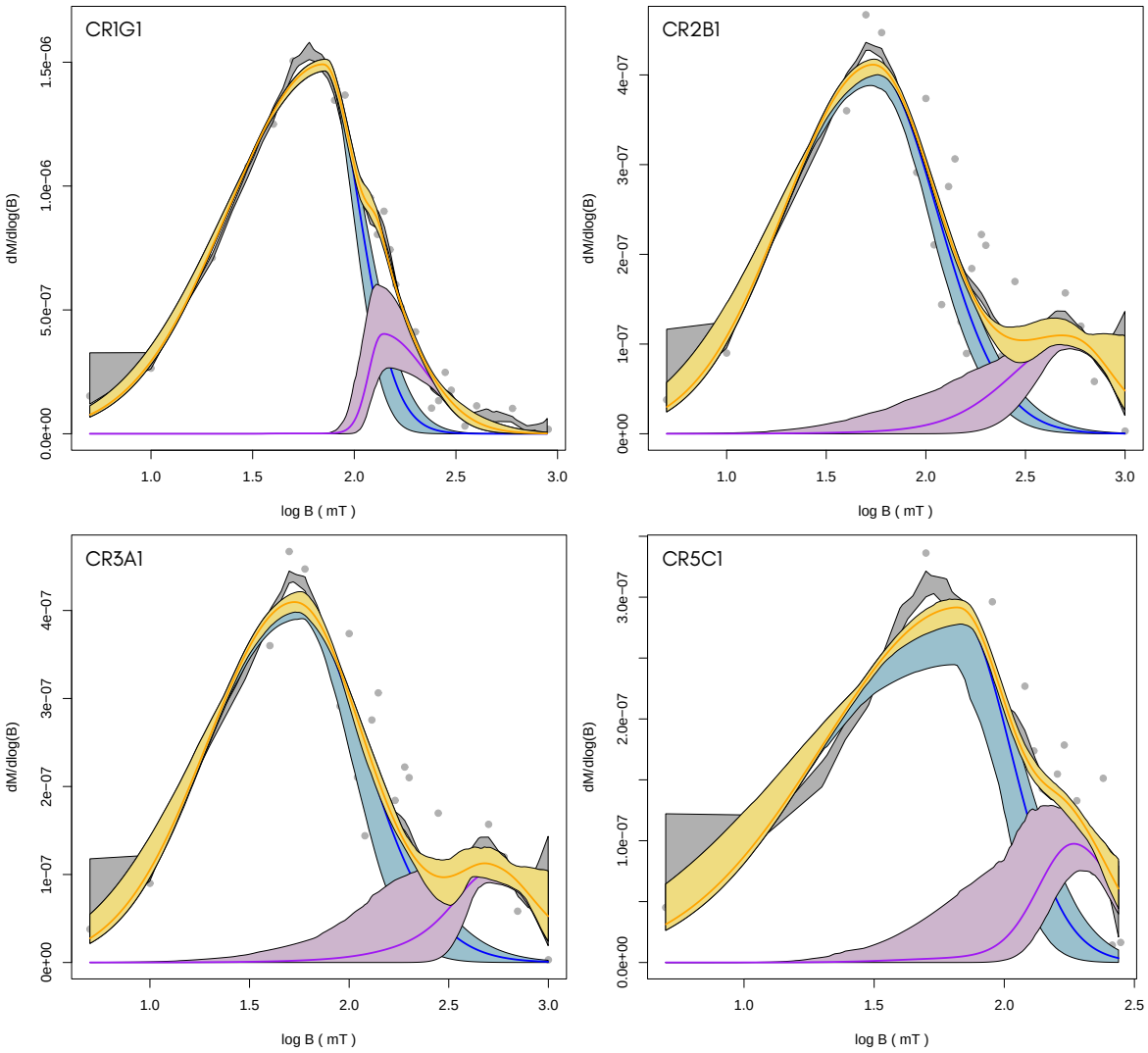

Figure C.1: Rhyolite IRM samples results obtained from MAXUnMix Software (Maxbauer et al., 2016) (gray circles are the original data, yellow line is the adjusted curve, colored lines represents each component and colored shaded areas are the error envelopes of 95% confidence intervals associated to each curve).

C.2 Mafic Dyke

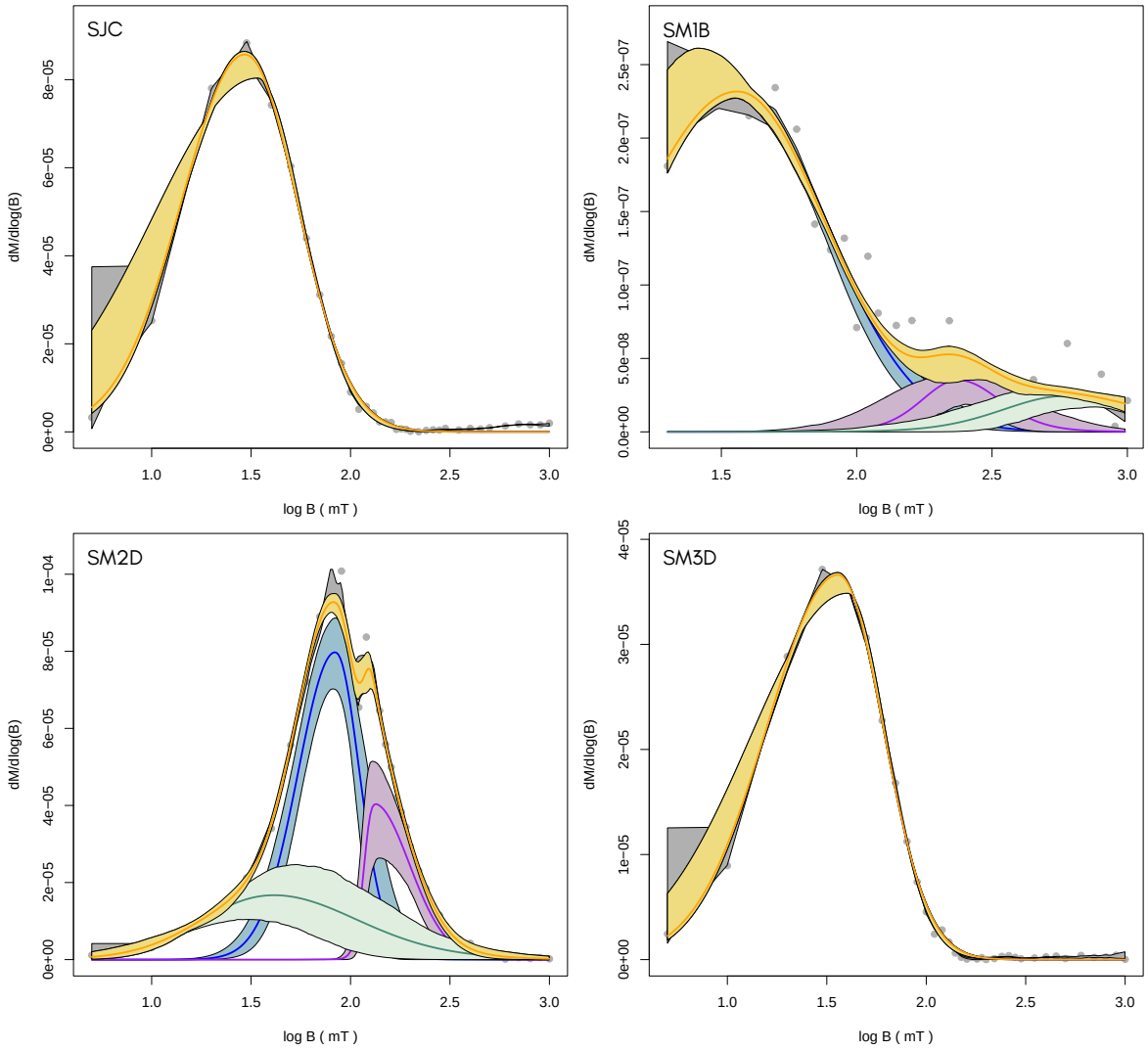

Figure C.2: Mafic dyke IRM samples results obtained from MAXUnMix Software (Maxbauer et al., 2016) (gray circles are the original data, yellow line is the adjusted curve, colored lines represents each component and colored shaded areas are the error envelopes of 95% confidence intervals associated to each curve).

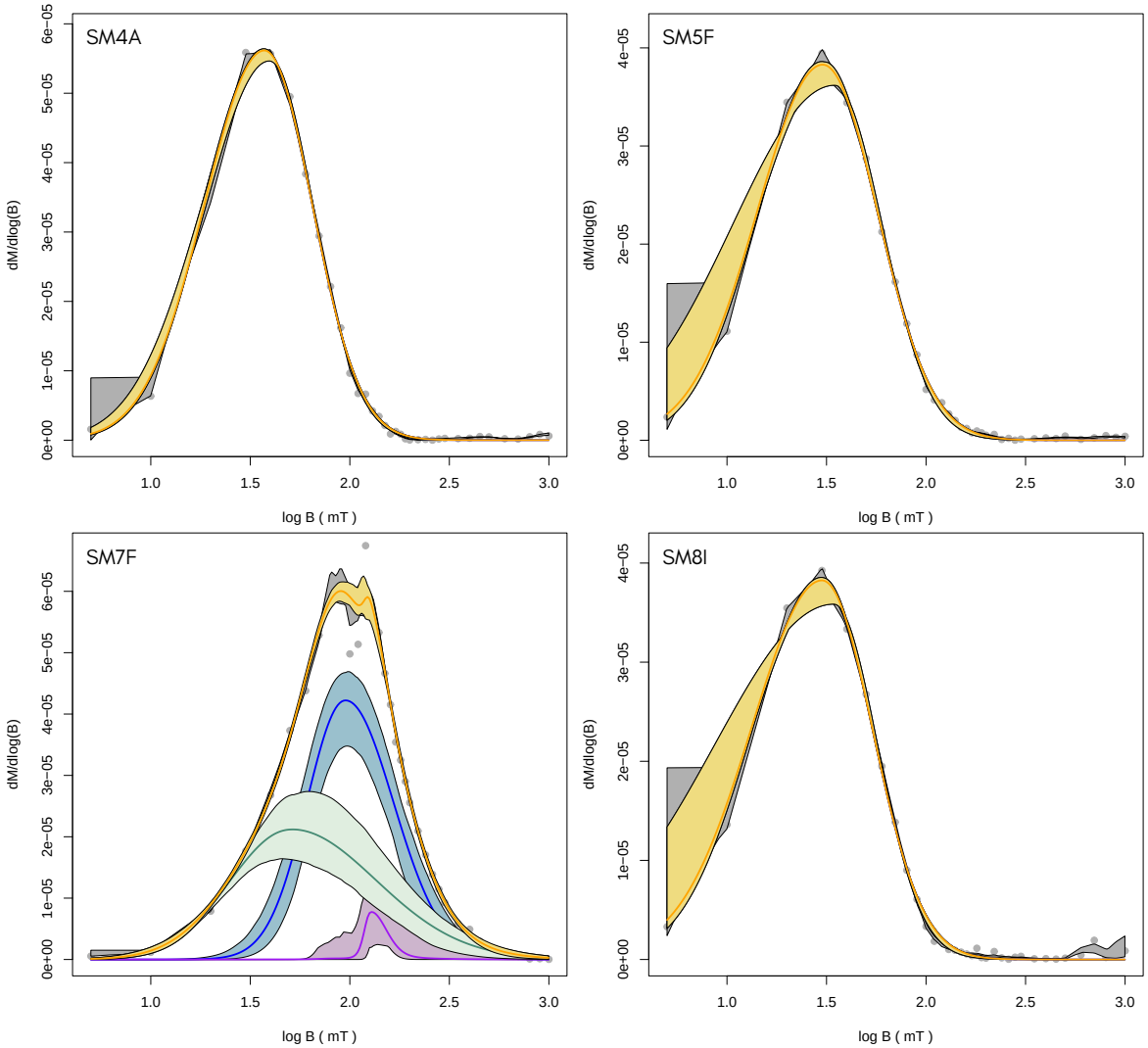

Figure C.3: Mafic dyke IRM samples results obtained from MAXUnMix Software (Maxbauer et al., 2016) (gray circles are the original data, yellow line is the adjusted curve, colored lines represents each component and colored shaded areas are the error envelopes of 95% confidence intervals associated to each curve).

Appendix D

Paleomagnetic Directions

Table D.1 - Thermal + AF demagnetization directional data of each sample

Sample	Demag. Teq.	Dec	Inc	Sample	Demag. Teq.	Dec	Inc
CR1N1	AF (V)	41.40	23.00	CR3H1	T (GC) *	346.0	64.5
CR1A2	AF (GC)	284.90	-20.10	CR4A1	T (V)	42.8	-20.7
CR1N1	AF (GC)	75.70	-63.40	CR4A2	T (V)	62.1	-42.04
CR1B1	T (V)	21.70	6.10	CR4A3	T (V)	59.2	-12.8
CR1D1	T (V)	50.30	-34.00	CR4B3	T (V)	68.9	-22.8
CR1E1	T (V)	31.20	39.80	CR4A1	T (GC)	91.8	62.5
CR1E2	T (V)	35.10	30.00	CR4A2	T (GC)	69.2	52.7
CR1B1	T (GC)	118.50	71.20	CR4B3	T (GC)	108.6	58.5
CR1C1	T (GC)	319.80	17.40	CR4B2	T (V)	74.9	-2.6
CR1C2	T (GC)	321.50	19.80	CR5C1	AF (V) *	53.2	-13.9
CR1E3	T (V)	34.30	22.60	CR5C1	AF (GC)	285.5	-66.5
CR2B2	T (V)	17.4	10.9	CR5E1	AF (GC)	33.2	46.0
CR2C1	T (V)	39.0	-0.1	CR5D1	T (V)	13.2	-15.2
CR2D2	T (V)	24.9	3.6	CR5E2	T (GC)	55.3	40.5
CR2I1	T (V)	17.4	3.2	CR6H2	AF (V) *	28.4	20.3
CR2D2	T (GC)	293.0	21.0	CR6B1	T (V)	20.4	46.6
CR2F1	T (GC)	146.9	16.4	CR6C1	T (V)	21.5	66.1
CR3A1	AF (V)	46.9	-17.0	CR6A1	T (GC)	163.5	28.6
CR3C1	AF (V)	57.6	-3.2	CR6D2	T (GC)	279.0	60.4
CR3A1	AF (GC)	325.3	13.7	CR7B1	AF (V)	31.7	38.4
CR3B1	T (V)	59.7	8.4	CR7B1	AF (GC)	69.3	-46.4
CR3C2	T (V)	97.7	-11.6	CR7A1	T (V)	20.8	24.4
CR3E1	T (V) *	65.6	-3.1	CR7A1	T (GC)	285.3	49.3
CR3E1	T (GC) *	157.2	7.4	CR7D1	T (GC)	303.3	-42.0

(Demag. Teq. = Demagnetization technique used, Alternating Magnetic Field (AF) or Thermal (T), and analyses procedure, Vetorial (V) or Great Circles (GC); * = Indicates if the antipode was taken in consideration; Dec = Declination; Inc = Inclination.)